Ultra-Wide Trans-Neptunian Binaries: Tracers of the Outer Solar System's History

by

Alex Harrison Parker
B.Sc., University of Washington, 2007

A Dissertation Submitted in Partial Fulfillment of the
Requirements for the Degree of

DOCTOR OF PHILOSOPHY

in the Department of Astronomy

Ultra-Wide Trans-Neptunian Binaries: Tracers of the Outer Solar System's History

by

Alex Harrison Parker
B.Sc., University of Washington, 2007

Supervisory Committee

Dr. JJ. Kavelaars, Co-supervisor
(Astronomy)

Dr. J. Willis, Co-supervisor
(Astronomy)

Dr. J. Di Francesco, Departmental Member
(Astronomy)

Dr. A. Weaver, Outside Member
(Earth and Ocean Sciences)

Supervisory Committee

Dr. JJ. Kavelaars, Co-supervisor
(Astronomy)

Dr. J. Willis, Co-supervisor
(Astronomy)

Dr. J. Di Francesco, Departmental Member
(Astronomy)

Dr. A. Weaver, Outside Member
(Earth and Ocean Sciences)

ABSTRACT

Ultra-wide Trans-Neptunian Binaries (TNBs) are extremely sensitive to perturbation, and therefore make excellent probes of the past and present dynamical environment of the outer Solar System. Using data gathered from a host of facilities we have determined the mutual orbits for a sample of seven wide TNBs whose periods exceed one year. This characterized sample provides us with new information about the probable formation scenarios of TNBs, and has significant implications for the early dynamical and collisional history of the Kuiper Belt. We show that these wide binaries have short collisional lifetimes, and use them to produce a new estimate of the number of small (∼1 km) objects in the Kuiper Belt. Additionally, these systems are susceptible to tidal disruption, and we show that it is unlikely that they were ever subjected to a period of close encounters with the giant planets. We find that the current properties of these ultra-wide Trans-Neptunian Binaries suggest that planetesimal growth in the Cold Classical Kuiper Belt did not occur through slow hierarchical accretion, but rather through rapid gravitational collapse.

Contents

List of Tables

List of Figures

ACKNOWLEDGEMENTS

I would like to thank the following mentors, colleagues, and administrators:

My supervisor, Dr. JJ Kavelaars, and collaborators who made this research possible, Lynne Jones, Jean-Mark Petit, Brett Gladman, and Joel Parker.

CADC staff, especially Stephen Gwyn and John Ouellette for their assistance with the technical and computational challenges of this work.

My academic supervisory committee, Jon Willis, James Di Francesco, and Andrew Weaver, for bearing with me during an atypical thesis schedule, and my external examiner Jean-Luc Margot for his careful reading of this work.

My professors from the undergraduate program at the University of Washington, especially Željko Ivezić and Ana Larson, who supported my early research and pointed me to the University of Victoria for graduate studies.

Former senior graduate students at the University of Victoria Melissa Graham and Wesley Fraser, who provided support and insight throughout.

Queue staff at the Gemini observatory, especially Chad Trujillo, Andrew Stephens, and Tim Davidge, who played a crucial role in making my observational program a success.

Technical resources

This research used the facilities of the Canadian Astronomy Data Centre operated by the National Research Council of Canada with the support of the Canadian Space Agency.

This work is based in part on observations obtained with MegaPrime/MegaCam, a joint project of CFHT and CEA/DAPNIA, at the CFHT which is operated by the National Research Council (NRC) of Canada, the Institut National des Science de lUnivers of the Centre National de la Recherche Scientifique (CNRS) of France, and the University of Hawaii.

This work is also based in part on observations obtained at the Gemini Observatory, which is operated by the Association of Universities for Research in Astronomy, Inc., under a cooperative agreement with the NSF on behalf of the Gemini partnership: the National Science Foundation (United States), the Science and Technology Facilities Council (United Kingdom), the National Research Council (Canada), CONICYT (Chile), the Australian Research Council (Australia), Ministério da Cieñcia e

Tecnolo- gia (Brazil) and Ministerio de Ciencia, Tecnología e Innovación Productiva (Argentina).

This work is also based in part on observations made with the European Southern Observatory Very Large Telescope at in Paranal, Chile; with the 200-inch Palomar observatory located in San Diego County, California, USA; with the 6.5 meter Magellan Telescopes located at Las Campanas Observatory, Chile; and with the WIYN observatory located at Kitt Peak, Arizona, USA.

Funding

This work has been supported by the United States' National Science Foundation Graduate Research Fellowship award DGE-0836694, and by the University of Victoria. I gratefully acknowledge the was support provided by the Criswick fund and the Faculty of Graduate Studies for travel.

Chapter 1

Introduction

The Kuiper Belt is a fossil remnant of the primordial disk of material from which the planets formed and which drove much of the dynamical and collisional evolution of the Solar System. Understanding the Kuiper Belt's present properties allows us to constrain its history and understand the mechanisms at play during the formation and evolution of the Solar System.

This document outlines a study of the properties of this population of minor planets in the outer Solar System, and explores how these properties can inform us about the present and past conditions at the edge of our planetary system. In particular, this study characterizes a sample of binary systems found in the Kuiper Belt, and examines the implications of their existence.

In this introductory section, the history of the search for minor planets is outlined and a brief summary of the implications of their discovery is presented, followed by a discussion of the discovery of the Kuiper Belt, the theories of its origin, and which of its properties we can measure with current facilities. The approach that this document takes in exploring the properties of binary systems in the Kuiper Belt is then presented, the chapters of the remainder of the thesis are outlined, and finally its most significant results are summarized.

1.1 History of the Search for Minor Planets

Until the invention of the telescope, the field of planetary science had been limited the study of the Earth, its Moon, and the five planets visible to the unaided eye — Mercury, Venus, Mars, Jupiter, and Saturn. The application of the telescope to astronomical observations led to the relatively rapid discovery of two more planets which had lurked unseen in the outer Solar System. The first planet to be discovered since antiquity was Uranus, recognized in 1781 by William Herschel (Herschel 1781). 65 years later, two researchers independently recognized that the orbit of Uranus was being perturbed by another more distant body, and a search turned up the planet Neptune in 1846 (eg., Adams 1846, Le Verrier 1846, Airy 1846).

Prior to the identification of Neptune, however, other searches had turned up smaller bodies in the space between Mars and Jupiter. In 1801, Giuseppe Piazzi identified the dwarf planet Ceres, the largest asteroid in the Main Belt. Other asteroids were soon identified, with Pallas, Juno, and Vesta discovered before the decade was out.

Before the advent of photographic techniques, the rate of discoveries was relatively slow. Only 322 objects were discovered in the 90 years between the discovery of Ceres and the first use of photographic plates to identify asteroids, but in the following 90 years over 10,000 new minor planets were found — averaging nearly one discovery every three days (see Figure 1).

Searching photographic data for asteroids was still primarily a manual process until the 1990s, when more sensitive Charge-Coupled Devices (CCDs) were widely deployed and automated detection pipelines were developed to more efficiently search for moving objects. At the peak rate of discovery around the year 2000, the average discovery rate was roughly *116 new minor planets every night.* As of October 2010, more than 200,000 minor planets have been assigned permanent numbers in the MPC, the vast majority of which are main belt asteroids.

1.2 Discovery of the Kuiper Belt and Other Reservoirs

The first stable reservoir of material discovered outside of the main asteroid belt was identified soon after the first application of photographic techniques to moving object detection. Jupiter was discovered to have a retinue of Trojan Asteroids, which reside in two clouds near the planet's L4 and L5 Lagrange points, leading and trailing the planet by roughly 60° while sharing its orbital period and semi-major axis. As of October 2010, there are 1,949 numbered Jupiter Trojans[1], but by factoring in the

---

[1] See http://www.minorplanetcenter.org/iau/lists/JupiterTrojans.html

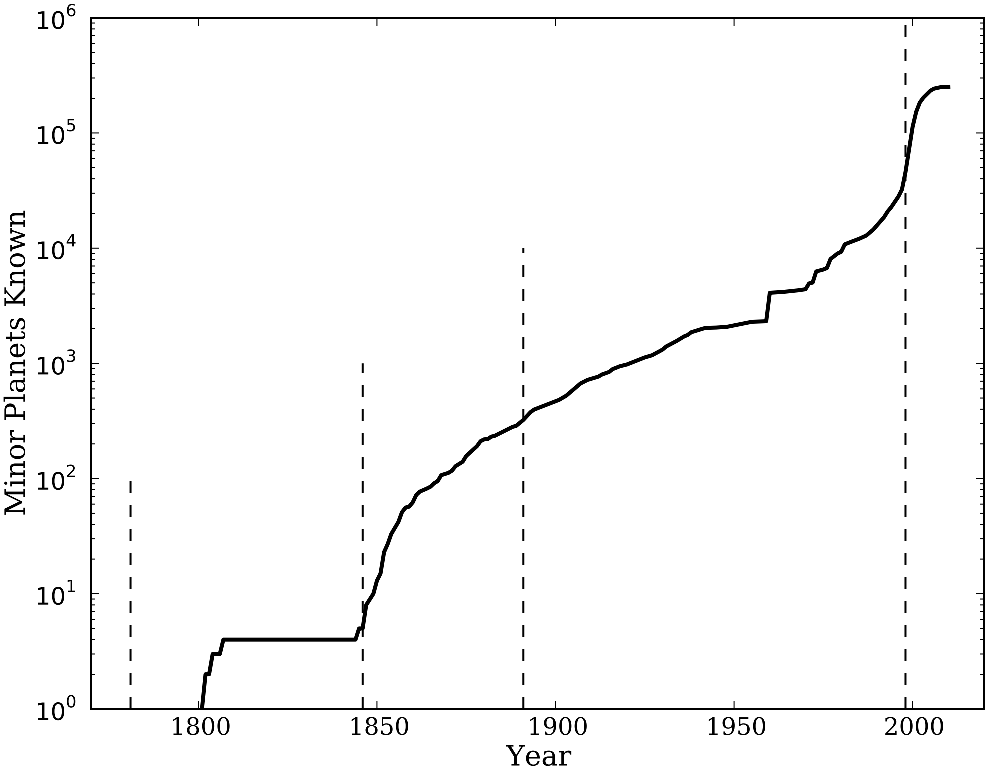

Figure 1.1: History of minor planet discoveries, illustrating the cumulative number of numbered minor planets known over time. Vertical dashed lines mark (from left to right) the discovery of Uranus, discovery of Neptune, the first use of photography for the detection of minor planets, and the start of extensive automated CCD surveys for minor planets. Discovery data from http://www.minorplanetcenter.org/iau/lists/NumberedPerYear.html.

effects of observational completeness on this more distant population, the Jupiter Trojan clouds are estimated to be at least as populous as the main asteroid belt (Yoshida & Nakamura 2005, 2008, Szabó 2007).

In 1930, Pluto became the first object to be discovered outside the orbit of Neptune (Tombaugh, 1946). Based on the assumption that perceived discrepancies in the motions of Neptune and Uranus were due to the gravitational influence of Pluto, its mass and size were estimated at the time to be comparable to Earth (eg. Nicholson & Mayall 1930), earning it the title of a planet. The discovery of this new planet led Frederick Leonard (1930) to suggest that it may be the first in a series of a new "family" of Trans-Neptunian planets. Later work by Kenneth Edgeworth (1949) showed, however, that the growth of planetesimals in the outer regions of the Solar System was slow, and numerous smaller objects analogous to comets might be expected to have formed. However, the early high mass estimates for Pluto led Gerard Kuiper (1951) to suggest that while a disk of icy condensates must have extended out past Neptune in the distant past, the putative mass of the planet Pluto would have been sufficient to long ago scatter any disk of material away, generating the Oort cloud of comets. When Pluto's mass was more accurately measured in the late 1970s and found to be nearly 500 times smaller than this initial estimate (Christy & Harrington 1978), it was evident that Pluto would have had no significant effect on the presence of a disk of Trans-Neptunian material.

In the early 1970s the first cis-Neptunian object was discovered (Kowal, Liller & Marsden 1979). Named Chiron, this object would become the first of a class of objects called Centaurs. These objects have orbits with semi-major axis less than Neptune's and which are unstable on timescales of 1—100 Myr (Tiscareno & Malhotra, 2003), and it was recognized that a much larger exterior reservoir of material must be resupplying them.

In 1980, it was shown by Fernandez that the orbital distribution of comets was inconsistent with an isotropic cloud of material like the postulated Oort cloud (Fernandez 1980). He suggested that the presence of a disk of material beyond the orbit of Neptune might be providing a component of the comet population, and soon Duncan, Quinn, and Tremaine (1988) showed that such a disk in addition to the Oort cloud could explain the observed comet distribution.

This evidence for a disk of material beyond the orbit of Neptune led to new searches for faint objects in the outer Solar System, and in 1993 Jewitt & Luu announced the discovery an object with such an orbit. 1992 QB_1 became the first known

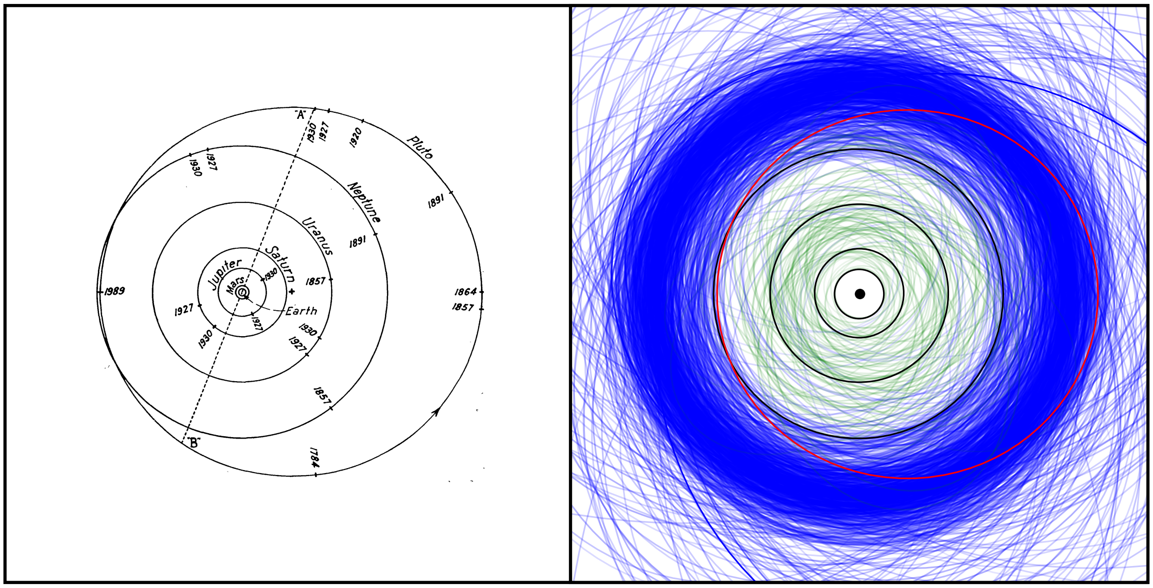

Figure 1.2: Then and now: The outer Solar System as it was known in 1930 on the left, with the new addition of Pluto (Figure from Leonard, 1930). On the right is the outer Solar System as it is known today, with each orbit with $a < 30$ AU represented in green (Centaurs), $a > 30$ AU represented in blue (TNOs), Pluto highlighted in red and the orbits of the giant planets shown for reference in black. Data from the Minor Planet Center's collection of Centaurs, TNOs and Scattered Disk Objects, found here: http://www.minorplanetcenter.org/iau/MPCORB/Distant.txt

object populating the region now frequently referred to as the Classical Kuiper Belt — and “Cubewanos” has since became a common alternate name for such objects.

1.3 Where did it come from?

In the classical picture of hierarchical planet formation, the growth of planetesimals in the Solar System proceeded in three stages. These stages, outlined below, are the initial coagulation of kilometer-scale bodies, followed by a rapid phase of runaway accretion, then finally slowed during the phase of oligarchic growth where only the largest objects continue to grow. For review of this process, see Kenyon et al. (2008).

1.3.1 Aggregation of small planetesimals

All planets and their smaller relatives emerged from the primordial disk of gas and dust grains circling the forming protostar that would become the Sun. In the classical planet-formation framework, the first step in going from micron-scale grains to planet-scale objects is creating meter- to kilometer-scale objects. Initially, the grains have a large surface area with respect to their mass and are coupled to the gas, and thus have low relative velocities, allowing them to stick after collisions and create larger aggregates. As their surface-area to mass ratios decrease, these aggregates become decoupled from the gas but still feel an aerodynamic drag (as the gas is partially supported by thermal pressure and orbits at sub-Keplerian velocities), which damps their vertical velocity component and causes them to settle into a thin plane. Here their mutual gravitational interactions are enhanced, and groups of aggregates can collapse into small (~ 1 m $-$ 1 km) planetesimals.

1.3.2 Runaway growth

These small planetesimals merge and grow through collisions. In addition to their physical cross-section for collision, they are assisted by their mutual gravity, which will enhance their effective cross section. The cross-section enhancement term from gravitational focusing is proportional to the square of the ratio of an object’s escape velocity to the relative velocity of colliding particles:

$$f_G \propto \left(\frac{v_{\text{esc}}}{v_{\text{rel}}}\right)^2 \tag{1.1}$$

At first, these small planetesimals continue to grow slowly, since relative velocities between planetesimals are relatively high and gravitational enhancement of their collisional cross-sections is not yet significant. As they continue to grow, mutual collisions and dynamical friction serve to reduce the relative velocities between planetesimals — which increases the gravitational enhancement of their collisional cross-sections and speeds their growth. Since this growth is enhanced with increasing object size ($v_{\text{esc}} \propto M$), the most massive planetesimals enter a phase of runaway growth, rapidly accreting large numbers of smaller objects.

1.3.3 Oligarchic growth and collisional grinding

Runaway growth continues until the mass contained in the few largest objects — the "oligarchs" — reaches a critical point. At this point, the oligarchs' gravitational perturbations are sufficient to stir the (much more numerous) smaller objects until the relative velocities between planetesimals is roughly the oligarch's escape speed. This reduces the efficiency of gravitational focusing and decreases the growth rate of the oligarchs.

While the oligarchs continue to grow slowly in this environment, collisions at these high velocities are no longer accretive for smaller objects but are instead disruptive. A collisional cascade begins which grinds the planetesimals that escape accretion onto the oligarchs to smaller and smaller sizes, eventually reducing them to dust. This dust is either later accreted onto the oligarchs or removed from the system through radiation pressure.

This phase of growth continues until each oligarch has consumed the mass residing in an annular region of space surrounding it, a "feeding zone" limited by the presence of other oligarchs on nearby orbits.

1.3.4 The Kuiper Belt's Missing Mass problem

In order to create a population of Kuiper Belt Objects at 40-50 AU from the Sun in the typical disk-clearing timescale (∼100 Myr), classical accretion scenarios require that it have been born with significantly more mass than we see today, and indeed the Trans-Neptunian region of the Solar System could be expected to have contained significantly more mass during formation than it presently does. The mass currently contained in the Trans-Neptunian region is estimated to lie near $0.1 M_{\oplus}$ (eg., Gladman et al. 2001), which implies a surface density of material of order 10^2 times lower than the extrapolation of the Minimum Mass Solar Nebula (MMSN, a disk containing the mass of all of the planets' refractory elements, distributed as $r^{-\frac{3}{2}}$), approximately 0.001 g/cm^2 and 0.1 g/cm^2 (Weidenschilling 1977) respectively. This "missing mass problem" suggests that some mechanism must have reduced the mass in the Trans-Neptunian region to present values.

A number of mechanisms have been proposed to reduce the mass in the Kuiper Belt. One subset of these processes suggest that some material was ejected through dynamical scattering from interactions with Neptune or a passing star, while another subset propose that the post-formation collisional cascade was enhanced by similar external perturbations. Another recently popular theory suggests that the Kuiper Belt formed interior to its present location, and was transported outward by interactions with a young Neptune (Levison & Morbidelli 2003, Levison et al. 2008). The present low mass of the Kuiper Belt would therefore not be indicative of mass being removed from this region, but instead would reflect poor efficiency in the transplantation mechanism. This second mechanism is part of a framework called the Nice model (eg., Morbidelli et al. 2005, Tsiganis et al. 2005), developed to explain the early evolution of the Giant planets' orbits and through this evolution explain a number of features of minor planet populations.

1.3.5 Gravitational Instability

A recent alternate approach to rapidly forming large planetesimals at large heliocentric distances has been to posit that the objects in the Kuiper Belt did not form through the classical accretion scenario. Rather, they formed through direct gravitational collapse from a solids-rich disk, driven by local density enhancements caused by a variety of aerodynamic effects. Recent simulations (eg., Johansen et al. 2007) have shown that particle aggregation can be significantly enhanced by aerodynamic effects due to instabilities in a turbulent gas disk, and dwarf-planet sized ($R \sim 100$ km) planetesimals may form very rapidly through this mechanism. Such models are relatively new and driven by recent advancements in numerical techniques, but current results show significant promise.

This scenario could resolve the missing mass problem. Cuzzi et al. (2010) report that the efficiencies of this mechanism in the range of 30—44 AU are such that forming the cold Classical population *in situ* is possible, even if adopting a sudden drop (by a factor of 1000) in density of solids outside of 30 AU in order to stop the migration of Neptune at this distance. Most of the mass of the resulting population of planetesimals would be in relatively large objects, with little extra mass in smaller planetesimals to remove through either collisional grinding or later dynamical processes.

1.4 Observables: What can we measure?

1.4.1 Orbital Distributions

The orbital distribution is perhaps the most fundamental observable that can be obtained for populations of minor planets. It encodes the present dynamics of the population, their interactions with other minor planet populations, and interactions with the giant planets. The Trans-Neptunian population can be broken broadly into three groups: the Classical Kuiper Belt, the resonant populations, and the scattered populations (for review of Trans-Neptunian nomenclature, see Gladman et al. 2008). These broad categories are further subdivided: for example, there are objects known in 1:1, 3:2, 2:1, and a number of other MMRs with Neptune. The Classical Kuiper Belt has been traditionally decomposed into the "Cold"- and "Hot"-Classical Kuiper Belt populations, defined by each component's inclination distribution (generally divided at $i = 5°$). As statistics have improved with larger and better-characterized samples of Trans-Neptunian Objects, further detail has started to emerge — for example, a possible collisional family has been identified through both dynamical clustering and spectroscopic properties (discussed later), associated with the dwarf planet Haumea (eg., Brown et al. 2007).

1.4.2 Size Distributions

Another fundamental observable is the size-frequency distribution, which is reflective of both the formation process of these objects and of their subsequent collisional evolution. In the case of the Kuiper Belt and most other minor planet populations, this is generally viewed from the perspective of a luminosity function, as sizes of objects are rarely directly measured, and instead generally inferred from their luminosity by assuming some estimate for their albedo. Over limited ranges of size (or luminosity), the behavior of minor planet size distributions are generally well described by power laws, though more complex behavior is observed over larger size ranges. This more complex behavior is frequently treated by adding extra components to the power law (as either a broken or rolling power law index).

In radius, the differential version of this power-law takes the following form:

$$dN = \left(\frac{R}{R_0}\right)^{-q} dR \tag{1.2}$$

When converted using absolute magnitude (H) as a measure of luminosity, the differential power-law takes the following form:

$$dN = 10^{\alpha(H-H_0)} dH, \tag{1.3}$$

where $q = 5\alpha + 1$. When considering the *cumulative* luminosity or size distributions ($N(>R)$ or $N(<H)$), the power-law index for the cumulative size distribution $q_c = q-1$, while the luminosity function index remains unchanged ($\alpha_c = \alpha$).

The luminosity function of the Kuiper Belt as a whole appears to have a relatively steep slope ($\alpha \sim 0.78$, eg., Fraser & Kavelaars 2009) for large ($R > 30$ km) objects, and a break to a shallower slope ($\alpha_2 \sim 0.18$) at approximately $m_R \sim 24.9$. When breaking the Kuiper Belt along dynamical lines, it appears that higher-inclination ("Hot") objects have a lower luminosity function slope than lower-inclination ("Cold") objects, which suggests that the two populations underwent different accretion histories (Fraser et al. 2010).

1.4.3 Surface Properties

Without physically visiting a Kuiper Belt Object, structure and compositional measurements must be made through remote sensing. Studies of the surface properties of KBOs have measured color properties, spectroscopic composition, albedo, phase function, and polarization properties.

Kuiper Belt Objects have relatively featureless optical spectra, with colors ranging widely from nearly solar to very red (eg., Barucci et al. 2005). The colors of these objects may be primordial in origin, or may be the result of some weathering process. Infrared spectra of Kuiper Belt Objects have similar variation. Large objects (Pluto, Eris, Makemake, Orcus, and others) show NIR absorption bands suggesting surfaces covered in volatile ices such as Methane (CH_4). Water ice absorption is also present on a number of objects (Barkume et al. 2008), and a class of objects have been discovered that are extremely rich in water ice. These objects all appear to be dynamically associated with the dwarf planet Haumea, and are thought to represent a collisional family from the aftermath of a shattering event which removed much of proto-Haumea's water-ice mantle (eg., Brown et al. 2007).

Albedos have been estimated from radiometric measurements made by the Spitzer and Herschel Space Telescopes (eg., Müller et al. 2010, Brucker et al. 2009). The largest objects, covered in bright ice deposits, frequently have very high albedo (eg., 0.86 for Eris, Brown et al. 2006). Low to moderate albedos (0.02—0.12) are frequent for smaller objects in most dynamical classes, but the Cold Classical Kuiper Belt appears to have higher typical albedos (Brucker et al. 2009). Albedo trends for the smallest objects have not been studied extensively, due to their extremely low thermal fluxes making detection impossible with today's instruments.

1.4.4 Multiplicity

Most, if not all, minor planet populations are host to multiple systems, including binaries and trinaries. These multiples have a vast array of properties, from extremely short-period, contact binaries, to systems which are exceedingly widely separated and mutual periods of many years. Some have tiny satellites, thought to be collisional fragments blown off of their parent, and others have components of near-equal size and mass.

The characteristics of these binaries represent a treasure trove of information about the properties of the objects that compose them, the environment they are embedded in, and the dynamical history of their parent population. Through their orbital separations and periods, binaries offer the only way to measure the mass of these distant objects, which when combined with radius measurements determine these objects' bulk densities — which in turn provide information about composition and physical structure (such as porosity).

This document focuses on what the characteristics of a particular class of binary can tell us about the present conditions in the outer Solar System, as well as what they can tell us about the objects that populate this region and their dynamical histories. The following section will outline the motivation of this study in more detail, and introduce the specifics of the observational and theoretical components of this study.

1.5 Binaries in the Kuiper Belt

The first object in the Trans-Neptunian region found to be binary was Pluto: its satellite Charon was discovered as a periodically-appearing "bulge" seen in photographic plates in 1978. The discovery of the satellite and measurements of its orbital properties allowed the mass of the Pluto system's mass to be measured accurately for the first time, and $\sim$1.421$\times$10^{22} kg, less than half of one percent the mass of the Earth — substantially revising its gravitational significance in the outer Solar System (Christy & Harrington, 1978).

The discovery in the mid-1990s of the first objects (since Pluto) in the Kuiper Belt has in the last 10 years been followed by the surprising discovery that a high fraction of these objects are in binary systems. The binary fraction varies in sub-populations from $\sim$ 29% in the "Cold" Classical Kuiper Belt to $\sim$5.5% in other dynamical classes (Noll et al. 2008a). Given the low interaction rates of the Kuiper Belt populations today, forming such a large number of binary systems has proven a theoretical challenge, especially with the limited information available for the components of these systems.

In a similar manner to binaries in any other astrophysical setting, Trans-Neptunian Binaries (TNBs) offer a unique window into understanding the physical structure and composition of Trans-Neptunian Objects (TNOs). Accurate mutual orbits allow determination of component masses (as with Pluto and its moon) and, if coupled with size measurements derived from thermal observations or direct detection, densities. The ice-to-rock fraction of objects in the Kuiper Belt is not constrained other than in the Pluto-Charon system and a handful of other very large objects which may have suffered mantle-loss events such as Haumea (Rabinowitz et al. 2006, Brown et al. 2007) and Quaoar (Fraser & Brown 2009), but is a strong indicator of the chemical environment at the time of formation (Lunine 1993). Density measurements are therefore essential in establishing the composition in the early solar nebula.

TNBs are distinguished from binary systems elsewhere in the solar system by the high frequency of near-equal sized binaries, and by the presence of binaries with extremely wide separations and long mutual-orbit periods. Widely-separated, long-period TNBs are difficult to create and very sensitive to perturbation (Nesvorný et al. 2011, Parker & Kavelaars 2010, Petit & Mousis 2004), and make valuable tracers of the dynamical and collisional conditions over the history of the outer solar system. The orbital, compositional and statistical properties of these binaries constrain the total mass and dynamical history of the various populations, with important implications for theories of Solar System formation and evolution.

There are several dozen known TNBs, but only a small subset have measured orbital parameters (Noll et al. 2008b, Naoz et al. 2010, Grundy et al. 2011). Most of these, in turn, are relatively tightly-bound binaries that have been characterized by observations from space (eg., Grundy et al. 2009 & 2011). Two TNB systems with moderately widely-separated components have published mutual orbits (1998 WW_{31} and Teharonhiawako/Sawiskera), but the widest TNBs have not been well-characterized to date, with a preliminary orbit estimate available only for the system 2001 QW_{322} (Petit et al. 2008). Such wide-separation, near-equal mass binaries all have low heliocentric inclinations, indicating that they belong to the cold component of the Classical Kuiper Belt. These wide binaries make up at least 1.5% of the known Cold Classical belt objects (Lin et al. 2010). This thesis presents the first-ever precise orbital measurements for a complete sample of the widest Trans-Neptunian Binaries.

1.5.1 Formation Mechanisms

Beyond the physical characteristics of the individual bodies, understanding the formation mechanisms for these systems provides constraints on the dynamical history of the outer Solar System. Proposed mechanisms for formation of Kuiper Belt binaries each imprint observable characteristics on the resultant systems. For example, collision of two bodies in the Hill sphere of a third object (Weidenschilling, 2002) tends to create widely separated binaries, while a two-step formation with first a collision creating an asteroid-like binary followed by an exchange reaction with an interloper (Funato et al., 2004) preferentially creates eccentric orbits. The Chaos Assisted Capture scenario (where two bodies are temporarily captured as a transient binary which increases the probability for an interloper to finally stabilize the system, Astakhov et al. 2005, Lee et al. 2007) preferentially creates systems with mass ratios of order unity and can create systems with eccentricities from zero to nearly one, but produces tightly bound systems with semi-major axes < 0.1 Hill radii.

The creation of large-separation, near-equal mass binaries is most likely during the formation phase of TNOs, as most proposed formation scenarios require a much higher space density of objects than is observed today. Additionally, most TNBs have identically-colored components, with differences between primary and secondary color being much smaller than the color variation seen between different binary systems and solitary TNOs. This suggests that each component formed from similar material in a similar region of a locally homogenous protoplanetary disk with global variations in composition (Benecchi et al. 2009). Different proposed mechanisms for binary formation dominate under different dynamical conditions (eg., Schlichting & Sari 2008a). If the dynamical properties of the systems today can be taken to be representative of their primordial distribution, they can probe the dynamical conditions of the primordial Kuiper Belt during the formation phase. However, any intervening violent dynamical events, like collisions (Petit & Mousis 2004, Nesvorný et al. 2011) or close encounters with giant planets (Parker & Kavelaars 2010) can leave today's mutual orbit distribution substantially altered from its original state. It is critical to measure the orbital properties of a large sample TNBs, as well as perform dynamical studies of possible sources of orbital modification, in order to understand the full extent of information about the formation and history of the outer Solar System encoded in these systems.

1.5.2 Observational Campaign

Wide-separation, near-equal mass binaries make up at least 1.5% of the known Cold Classical belt objects (Lin et al. 2010), and represent ∼7% of all binaries in this population. We have performed a targeted astrometric monitoring campaign, which has measured the on-sky separations and position angles of a sample of wide-separation, long-period TNBs at multiple epochs.

Since we seek to characterize the widest binaries, which have correspondingly long periods, we opted to pursue a ground-based observation campaign. We chose our sample based on the following criteria: (1) the system had no well-characterized orbit in literature, (2) the separation at discovery exceeded $0''.5$, and (3) the magnitude difference between the system's primary and secondary was less than 1.7, indicating a near-equal mass system (mass ratio < 10). At the time of our sample selection, there were 7 systems that met these criteria: 2000 CF_{105}, 2003 UN_{284}, and 2005 EO_{304}, 2001 QW_{322}, and three objects discovered over the course of the Canada-France Ecliptic Plane Survey, with internal designations b7Qa4, L5c02, and hEaV.

For all non-CFEPS objects, some astrometric measurements exist in literature. For 2000 CF_{105}, Hubble Space Telescope observations have been made during several separate epochs. We incorporate these and other literature data points into our mutual orbit fits where possible. We have also used a number of observations extracted from public archives, identified using the Solar System Object Search[2], allowing us to sample temporal baselines of up to a decade for some objects.

These binary systems are extremely faint — several thousand times fainter than Pluto was when its binary nature was discovered. As such, in order to obtain high signal-to-noise measurements, observations from 8-meter class instruments were essential. From 2008—2011, observations were obtained from an observing campaign at Gemini North with the GMOS instrument, requesting short visits at very high image quality. These observations, conducted in seeing as good as $\Gamma \sim 0''.35$, provide extremely strong constraints on the orbital properties of these targets. A supplemental program was conducted at the VLT with the FORS-2 instrument during 2009—2010 with similar results.

Mutual orbit parameters for our sample have been estimated based on this data set using a newly-developed mutual-orbit fitting algorithm. These mutual orbits show that our sample is unique, as no object in literature (other than 2001 QW_{322} which has a published preliminary mutual orbit) has a mutual period exceeding 2.3 years, while objects in our sample have periods ranging from 3.9—17 years.

1.5.3 Dynamical Studies

Given the low gravitational binding energies of these widely-separated binaries, they make excellent tracers of past dynamics in the outer Solar System. We have pursued two studies which utilize these binaries to constrain the extent of violent events in the history of the Kuiper Belt.

The first is simple consideration of the collisional lifetimes of these systems. Since they are immersed in an environment filled with numerous projectiles traveling at relative velocities of ~1 km/s, they will eventually be collisionally unbound. The timescale for collisional unbinding of these systems is approximately an order of magnitude shorter than the timescale for the collisional disruption of one or both of their components (Petit and Mousis, 2004). We have developed a collisional code which subjects these binary systems to a series of impulsive encounters and tracks their orbital evolution through this process. With this code we determined each system's mean collisional lifetime τ under various simulated Kuiper Belts. By positing that wide binaries were initially much more numerous (comprising up to 100% of the Cold Classical Kuiper Belt objects), we estimated an upper limit on the $R \sim 1$ km impactor

---

[2] SSOS is a service provided by the CADC: http://www1.cadc-ccda.hia-iha.nrc-cnrc.gc.ca/ssos/

population that could reduce this initial population of binaries to the present number without completely destroying the wide binary component. The R∼1 km population is currently undetectable through direct imaging (with *R* magnitudes of order 30), and the only existing limits on their numbers come from searches for stellar occultations.

The second study is a test of the hypothesis that the Kuiper Belt was transported outward by interactions with Neptune. The specific scenario tested is that suggested by Levison et al. (2008), in which the Cold Classical Kuiper Belt is generated by the capture of scattered planetesimals in broad MMRs with an initially eccentric Neptune. These captured planetesimals can chaotically diffuse to low eccentricity and be trapped when the MMRs narrow as Neptune's eccentricity damps to present values. We simulated this implantation mechanism and track the Neptune close encounter history of each object that eventually resides in the Cold Classical Kuiper Belt, and subjected synthetic binary systems to these close encounters. We show that these encounters are destructive to wide binaries, and that the present wide binary population would be unlikely to survive this violent transportation to their current location.

1.6 Thesis Agenda

1.6.1 Chapter 2: Mutual Orbits

This section presents the binary observational campaign, archival image search, data reduction process, and application of a new mutual orbit fitting code to the complete astrometric data set compiled to date for all seven wide binaries in our sample. Individual systems' peculiarities will be discussed, and comparisons to previous estimates of system properties are made. It also presents the distribution of mutual orbit parameters and their implications for the binary formation mechanism(s), and compares the properties of the wide binaries with other binary populations in literature. Estimates of each system's albedos are presented, and a preliminary functional albedo distribution is found. Additionally, this section introduces possible evolution processes, and discusses each system's likely Kozai cycle amplitudes and whether these are likely to affect each system's long-term stability or formation mechanism interpretation. Finally, future prospects for discovering and characterizing wide binary systems with large-scale optical surveys are presented.

1.6.2 Chapter 3: Collisional Evolution of Mutual Orbits

Further discussion of a possible evolution process: simulations of orbital evolution due to collisions over the age of the Solar System. These first-order simulations estimate the mean survival lifetime of each binary system given the present collisional environment of the Kuiper Belt. From these lifetimes, an estimate of the upper limit on small (R ∼1 km) objects in the Kuiper Belt is made. Evolution of the mutual orbit properties over the age of the solar system is tracked, and implications for the primordial orbit distribution and binary formation mechanism are explored. Finally, the probability of detecting collisions in real-time with future surveys through transient brightening caused by expanding debris clouds is explored.

1.6.3 Chapter 4: Binary Disruption by Neptune Scattering

This section discusses a suite of simulations to determine the effects of transport of the Kuiper Belt by Neptune scattering on binary systems (for more details see Parker et al. 2010), finding that the wide binaries would have been easily destroyed by such encounters.

1.6.4 Chapter 5: Summary and Conclusions

A final synthesis of all the findings of the thesis, with an emphasis on future prospects.

1.7 Summary of Significant Results

1. Most precise estimates of seven wide TNB mutual orbits are determined. Several of these systems set new records for separation, mass, and mutual eccentricity.

2. The outer orbit distribution of all known TNBs with semi-major axes exceeding 0.02 Hill radii is consistent with being drawn from the CFEPS L7 debiased model of the Cold Classical Kuiper Belt (the "stirred" and "kernel" components). They are inconsistent with being drawn from any other model population, indicating that the wide binaries are hosted exclusively by the dynamically-cold component of the Classical Kuiper Belt.

3. Mutual orbits of wide TNB systems are inconsistent with the predictions of several binary formation models (L_2s process, chaos-assisted capture, and exchange

reactions).

4. Mutual orbits of wide TNB systems are most consistent with the outcomes of simulations of forming binaries through direct gravitational collapse. Current simulations of this process make no predictions about the mutual inclination distribution, however.

5. Four systems have securely prograde orbital solutions, and another three are securely retrograde, and thus it appears that wide binaries have no strong preference for prograde or retrograde orbits. The mutual inclination distribution of wide TNBs is inconsistent with having been drawn from either a uniform distribution or the same inclination distribution as the tighter binaries in literature. Wide TNBs prefer low mutual inclinations, suggesting formation in a dynamically-cold disk.

6. Albedos of these wide binaries are found to range from 0.08-0.3, consistent with the known albedos of solitary Cold Classical TNOs. We find that the albedos and radii of the wide binaries are consistent with being drawn from a gaussian distribution centered at $p = 0.05$ with width $0.058 \leq \sigma \leq 0.1$, clipped such that $p > 0.05$.

7. Wide TNBs are susceptible to disruption by collisions with much smaller objects. Assuming they are the remnant of a collisionally-decayed primordial population of wide binaries, we limit the number of objects larger than 1 km in the current Classical Kuiper Belt to less than 10^{10} for size distribution slopes $q \lesssim 3.5$.

8. Collisional erosion over the age of the solar system can produce similar trends in binary fraction with radius as are predicted for a short epoch of intense collisional grinding by the simulations of Nesvorný et al. (2011), and therefore the product of both processes must be considered if such trends are detected in the future.

9. Wide TNBs are unlikely to be collisionally-evolved tight TNBs, and their inclination distribution must have preferred low inclinations more strongly in the past, further bolstering the evidence for a dynamically-cold primordial disk.

10. Wide TNBs are susceptible to tidal disruption by close encounters with giant planets. As such, we show that the transportation mechanism presented by

Levison et al. (2008) would have decimated the wide binary population in the Cold Classical Kuiper Belt, suggesting that the Cold Classical Kuiper Belt formed in situ or was transported by an as-yet unknown gentler mechanism.

11. A confluence of results — *(a)* gravitational collapse producing similar binary properties as are observed, *(b)* the evidence that the cold Classical Kuiper Belt was not subjected to a period of close encounters with Neptune, and *(c)* the mutual orbits of the wide binaries suggesting formation in a very dynamically-cold environment, yet the L_2s mechanism not dominating the binary formation process — all suggest that the cold Classical Kuiper Belt formed in situ through rapid accretion of small particles directly into large ($10-100$ km) planetesimals, driven by turbulent concentration of solids and gravitational collapse.

Chapter 2

Mutual Orbits

We have collected astrometric measurements of a sample of seven of the widest-known TNBs for an extended period, covering four to nine years of orbital motion for each system. These observations have allowed us to compute accurate mutual orbits for our sample of ultra-wide TNBs, and from these orbits we derive system mass and a host of other characteristics. In the first half of this chapter, we outline the nomenclature we adopt to describe these systems and their host populations (§2.1), our sample selection criteria (§2.2), details of our observational campaign and data reduction techniques (§2.3), and mutual orbit fitting algorithm (§2.4). In the latter half, we describe the mutual orbit fits (§2.5) and compare them to the properties of other binary populations, and derive geometric albedos for each system given reasonable assumptions of bulk density (§2.6). Finally, we conclude with a discussion of possible formation mechanisms and implications for the early history of the outer solar system, and present future surveys' abilities to discover and characterize a large sample of these ultra-wide TNBs.

2.1 Nomenclature

In this manuscript, we compare several sub-populations of Trans-Neptunian Objects and their various orbital properties. In order to facilitate a clear understanding of the nomenclature we use to describe these populations and their properties, we provide an outline here.

A binary's mutual orbit properties will be described either as a "mutual" property or denoted with the subscript "m." By contrast, the properties of the orbit of the binary's barycenter around the Sun will be described as an "outer" property or denoted with the subscript "out."

In order to compare the properties of our sample with those in literature, some dynamical classification is required. We adhere roughly to the Gladman et al. (2008) nomenclature when discussing outer orbit properties. In this manuscript, we frequently deal with binaries which belong to the following dynamical classes:

- "Classical:" Non-resonant objects in the range 34 AU$\leq q_{\text{out}} \leq$ 47 AU, 37 AU $\leq a_{\text{out}} \lesssim$ 70 AU.
- "Cold Classical:" Subset of "Classical" objects with low orbital excitations and confined in semi-major axis. When dividing samples, we assign "Classical" binaries with $i_{\text{out}} < 10°$, $q_{\text{out}} > 38$ AU, and $42.4 \leq a_{\text{out}} \leq 47$ AU to this population. Referred to as CC population in text.
- "Hot Classical:" Subset of "Classical" objects with higher mean orbital excitations, and an extension to lower pericenter than CC population. When dividing samples, we assign "Classical" binaries with $i_{\text{out}} > 10°$, $q_{\text{out}} < 38$ AU, $a_{\text{out}} < 42.4$ or $a_{\text{out}} > 47$ AU to this population. Referred to as HC population in text.

This dynamical classification is somewhat different than that adopted by Grundy et al. (2011), and several binaries in that work which were classified as "extended scattered" fall into our HC classification.

In addition, we compare the outer orbital distributions of binary sub-samples with the CFEPS L7 synthetic model of the Kuiper Belt[1]. We compare the CC binary sub-sample with the composite of the "stirred" and "kernel" sub-components of the synthetic Kuiper Belt model, and refer to the composite of these sub-components as CC-L7. We compare the HC binary sub-sample with the "hot" sub-component of the synthetic Kuiper Belt model, and refer to this sub-component as HC-L7.

In reality, any simple inclination cut is insufficient to determine which population a given object truly belongs to, as both the CC and HC populations overlap significantly. According to the CFEPS L7 model, most relatively bright objects below 10° of inclination actually belong to the HC-L7 population. We stress that while we will refer to a given object as a "CC" binary or a "HC" binary, there is no way to

---

[1] Available at `http://www.cfeps.net/L7Release.html`

absolutely verify the parent population for a given single object. However, we show later that the sub-samples of binaries which fall into our CC and HC classifications have dynamically distinct mutual orbit distributions, and the outer orbit distributions of CC binaries suggest that they are in fact members of the CC-L7 population, and likewise the HC binaries' outer orbit distribution is consistent with the HC-L7 distribution.

2.2 Sample Selection

Since we seek to characterize the widest binaries (which have correspondingly long mutual periods), we opted to pursue a ground-based observation campaign. We chose our sample based on the following criteria:

1. The system had no well-characterized orbit in literature.
2. The separation at discovery was $\gtrsim 0''.5$.
3. The magnitude difference between the system's primary and secondary was less than 1.7, indicating a near-equal mass system ($M_p/M_s \lesssim 10$).

At the time of our sample selection, there were 7 systems that met these criteria: 2000 CF_{105}, 2001 QW_{322}, 2003 UN_{284}, 2005 EO_{304}, and three objects discovered over the course of the Canada-France Ecliptic Plane Survey (CFEPS), with internal designations b7Qa4, L5c02, and hEaV. The binary nature of 2000 CF_{105} was presented in Noll et al. (2002), while the binary natures of 2003 UN_{284} and 2005 EO_{304} were presented in Kern (2006). Provisional orbital characterization for 2001 QW_{322} was presented in Petit et al. (2008). The CFEPS target L5c02 was identified as binary by Lin et al. (2010), and the binary nature of b7Qa4 and hEaV are presented here for the first time. All of the outer orbits of this sample of objects fall into our CC classification, and have very low outer inclinations and eccentricities.

Two other CFEPS targets, L4q10 and L4k12, were initially included in our sample, due to data from CFHT suggesting they were elongated in a manner consistent with a near-equal mass binary with a separation of order $0''.5$. However, follow-up observations in very good seeing did not bear out their putative binary nature, and they were removed from our target list.

Table 2.1: Observations and System Properties

Name	Date Range	N_{visits}	N_{obs}	m_{sys}	Δm	${H_p}^e$	Outer Orbit		
				(r')	(r')	(r')	a_{out} (AU)	e_{out}	i_{out} (°)
2000 CF_{105}	2002-2011	12	50	23.85^a	0.72(5)	7.70	43.84	0.0362	0.528
2001 QW_{322}	2001-2010	35	88	23.16^b	0.03(5)	7.51	43.98	0.0242	4.808
2003 UN_{284}	2003-2010	14	60	22.7^c	0.88(6)	7.5	42.62	0.0035	3.069
2005 EO_{304}	2005-2011	12	52	22.45^d	1.45(3)	6.59	45.62	0.0679	3.415
b7Qa4	2006-2011	20	66	23.0^a	0.50(4)	7.3	43.80	0.0393	1.157
hEaV	2006-2011	15	56	22.7^a	0.98(2)	6.9	44.70	0.0804	3.550
L5c02	2004-2010	15	47	23.0^a	0.44(5)	7.0	45.74	0.0362	1.791

2.3 Observations and Data Reduction

A targeted observational campaign from 2008—2011 was executed from *Gemini North* using the *Gemini Multi-Object Spectrograph* in imaging mode, taken with the r_{G0303} filter. Observations were queue scheduled, with stringent requirements on image quality (frequently at the expense of photometric conditions). By requiring modest visit times ($\sim$ 30 minutes), excellent seeing could be obtained without the use of AO, in some cases with full-width half-max of $\Gamma \simeq 0''.35$ or better. Additional observations during this period were made from *VLT* with the *FORS2* instrument, though image quality requirements were not held to the same stringent limits. Single-epoch observations were also made in April 2010 from *Magellan* with the *Megacam* imager.

Significant archival data also exists for all systems. We used the *Solar System Object Search* (Gwyn 2011, in prep) service provided by the *Canadian Astronomy Data Centre* to locate and download images from the *CFHT* and *HST* public archives that contained our targets, and we also located images of our targets from the *Mayall*, *Hale*, and *WIYN* telescopes.

Literature astrometric measurements are available for some systems as well. The relative astrometry for 2001 QW_{322} published in Petit et al. (2008) is also included in our fit for that system. Astrometric measurements of 2003 UN_{284} and 2005 EO_{304} were presented in Kern (2006), and we include those measurements in our fits for these systems.

Combining all these data sources, the smallest number of observed epochs for any binary in our sample is 12 visits for 2005 EO_{304}, while the largest number is 35 visits for 2001 QW_{322}. During most visits, more than one usable image was acquired. The number of visits and total number of images from which astrometric measurements were made are listed in Table 2.1.

Astrometric solutions were generated for each individual image, matched to the J2000 coordinate system using reference stars in the *USNO b* astrometric catalog. Whenever possible, the catalog stellar positions were corrected for proper motion since their last observed epoch, and uncertainties in the final reference positions reflected the original astrometric precision and the integrated uncertainty due to the stated uncertainty in proper motion over the intervening time.

The brightest 100 non-saturated stars were identified in the CCD on which the binary was located (in the case of multi-chip imagers, other chips in the array were not used to constrain the astrometric solution), and their (x, y) positions (and uncertainties) extracted using *SExtractor* (Bertin & Arnouts, 1996). In the case of an image with a good initial World Coordinate System (WCS) estimate (eg., *Gemini GMOS* images), this WCS was used to estimate each stars' RA and DEC position in the J2000 system and the nearest neighbor in the *USNO b* catalog was identified as its matching counterpart.

If an image did not have a good initial WCS, a robust pattern-recognition algorithm identified probable rough corrections to the WCS, applied these corrections, and then identified nearest-neighbor stars in the *USNO b* catalog.

Once *USNO b* (RA, DEC) positions were matched to (x, y) positions in the image, the *IRAF* package *ccmap* was used to generate a WCS solution. Because this package does not handle positional uncertainties in either the image or reference positions, the positions of each matched star is cloned 1,000 times, adding Gaussian noise to each position consistent with the (RA, DEC) and (x, y) uncertainties. Iterative fitting followed by automatic clipping of outliers in these thousands of cloned sources allowed *ccmap* to generate a robust astrometric solution automatically which reflected the uncertainties in the absolute and measured positions of the reference stars. This allowed a more robust automatic solution to be derived with little input from the operator for each image processed.

After the first pass of *ccmap*, more matches are searched for in the image with the *USNO b* catalog reference stars, and upon flagging any new matches the *ccmap* routine is called again. This matching and WCS-fitting process is iterated ten times for every frame.

The lowest-order astrometric solution merited by the distortions of the optics of each imager was used in each case. In the case of *Gemini GMOS* images, this was a simple rotation and fixed pixel scale. In the case of most other imagers, the distortion across the area of a single CCD was low enough such that the addition of independent x and y pixel scales, as well as a skew term, was sufficient. In the case of HST observations, the internal HST astrometric solutions and distortion corrections were used.

Once an astrometric solution had been found for an image, the relative astrometry of the binary pair in that image was then extracted using a custom Point-Spread Function (PSF) fitting routine. The PSF model we adopted was a sum of two elliptical Gaussian components, with arbitrary long-axis orientation for each component. The wider of the two Gaussians (the PSF wings) is arbitrarily limited to contain less than 2/3 the flux of the narrower "core" Gaussian to prevent runaway solutions with extremely wide wings. Adopting a non-circular PSF was required due to the fact that most images were obtained with sidereal tracking rates, and over the period of integration the PSF of the binary's components became somewhat stretched along their direction of motion.

A variant of the same algorithm used for fitting the mutual binary orbits (described in the following section) was used to minimize the residuals in a sky-subtracted 40×40 pixel region centered on the binary. An initial interactive step is used to identify all the point sources in this region and flag the two associated with the binary. Initial estimates for the amplitude and Γ of the PSF are made automatically, and these values are fed into a Markov-Chain Monte Carlo algorithm which finds the PSF model and array of point source positions and amplitudes that produces the smallest residuals. Because the image model varies with the number of point sources in the 40×40 pixel region, the minimum number of free parameters the algorithm must search over is 9 (two point sources, and a two-component PSF model forced to be circular) while the maximum number of free parameters ever treated was 22 (five point sources and a two-component PSF model with arbitrary rotation and ellipticity for each component). Example of data from the *Gemini* observatory is illustrated in Figures 2.1 and 2.2, along with the image residuals after PSF fitting and subtraction, and the model of the binary system. Each fit is visually inspected, and in general we found that our adopted PSF model produced extremely low residuals.

In some cases where the two binary components were blended, we performed a check to verify that the extra degrees of freedom added by allowing the PSF to be elongated was not skewing the measured astrometry. In these cases, we performed a second, independent fit using a circular PSF and compared the measured astrometry for the binary components. In general, we found excellent agreement between the two. In cases of very strong blending, fits with the elongated PSF would occasionally have trouble converging to a stable solution, and in these cases we adopted the values from the circular PSF fits. We did not attempt to determine any upper limits on separation based on completely unresolved images, and therefore at present such images do not contribute to our mutual orbit fits.

Relative astrometry was recorded as separation (in arcseconds) and position angle (in degrees East of North), and the observation date was taken at the central Julian Date of each observation. Uncertainty in the relative astrometry was estimated as $\sigma_{xy} \simeq \Gamma\sqrt{\mathrm{SN}_p^{-2} + \mathrm{SN}_s^{-2}}$, where SN indicates signal-to-noise ratio of primary or sec-

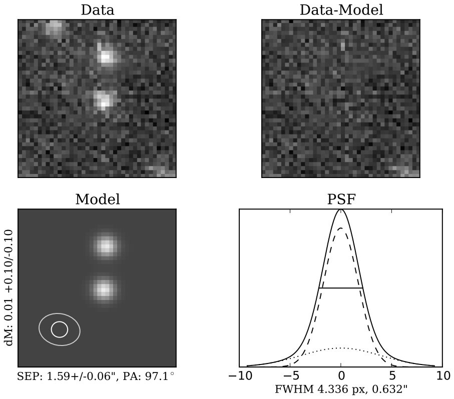

Figure 2.1: Example of Gemini data and PSF fit. Top left: Original image from GMOS camera of 2001 QW_{322}. Bottom left: Synthetic PSF model of binary components. Top right: Image residuals after subtracting binary and other point-sources in the image. Bottom right: Relative contributions of both PSF components. Same stretch is applied to all images, and flux scaling is linear.

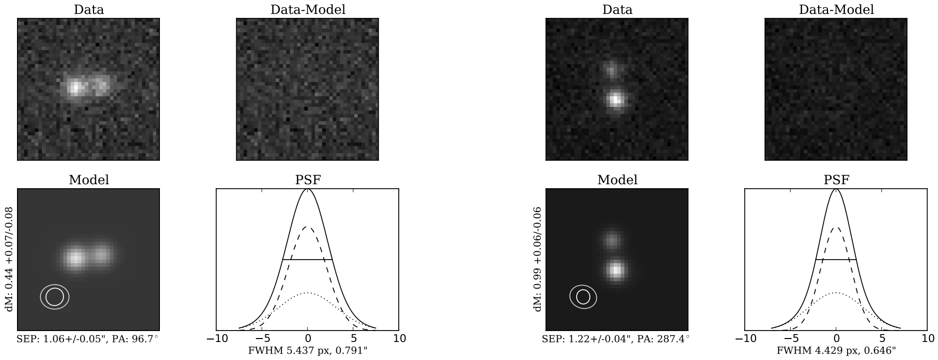

Figure 2.2: Same as Figure 2.1, but for CFEPS binaries b7Qa4 (left) and hEaV (right).

ondary. A noise floor is set by the uncertainty in the astrometric solution for each frame.

These PSF fits also returned relative photometry for each system, and the mean Δ-mag measured in the *Gemini GMOS* r_{G0303} filter during well-resolved visits is also included in Table 2.1. Relatively few observations were made in photometric conditions, as image quality was our primary concern. All MPC targets in our sample have published absolute system photometry in various bands, but only 2001 QW_{322} and 2005 EO_{304} have r'-band magnitudes in literature. 2000 CF_{105}, b7Qa4, hEaV, and L5c02 were all imaged on photometric nights from CFHT, and *Elixir* processed images were used to determine r'-band system magnitudes for these systems. The r'-band magnitude of 2003 UN_{284} was determined from observations on a single night from Gemini North, though the absolute calibration of these particular images is poor and the resulting photometric uncertainty is relatively large.

2.4 Mutual Orbit Determination

The basic operations performed by our mutual-orbit fitting routine are, given an initial guess of mutual orbit properties, to solve Kepler's equation in order to determine the relative system geometry at the time of observation (accounting for the light-time delay between the system and observer), then rotate the system in space to account for its orientation with respect to the Ecliptic. Finally, the code "observes" the system by applying a second rotation to account for the variation in viewing geometry induced by the relative motion between the Earth and the binary, and projects the result onto the sky plane given the separation between the observer and the system.

To fit our observations, we chose to adopt the Metropolis algorithm χ^2 minimization routine (Metropolis et al. 1953), using a similar implementation to that described in Simard et al. (2002), who utilized the Metropolis algorithm to fit a 12 dimensional bulge + disk model to images of galaxies. This algorithm is robust to complicated topology in parameter space, and can be easily adjusted to thoroughly explore parameter space at the expense of speed. The Metropolis algorithm is a Markov-Chain Monte Carlo technique which, after an initial burn-in period, occasionally makes "bad" decisions, allowing it to diffuse out of local minima. After a number of iterations, the choice of new parameter values can be informed by previous values, improving the speed of convergence in complicated parameter-space topology. A binary mutual orbit has seven free parameters, and in our implementation

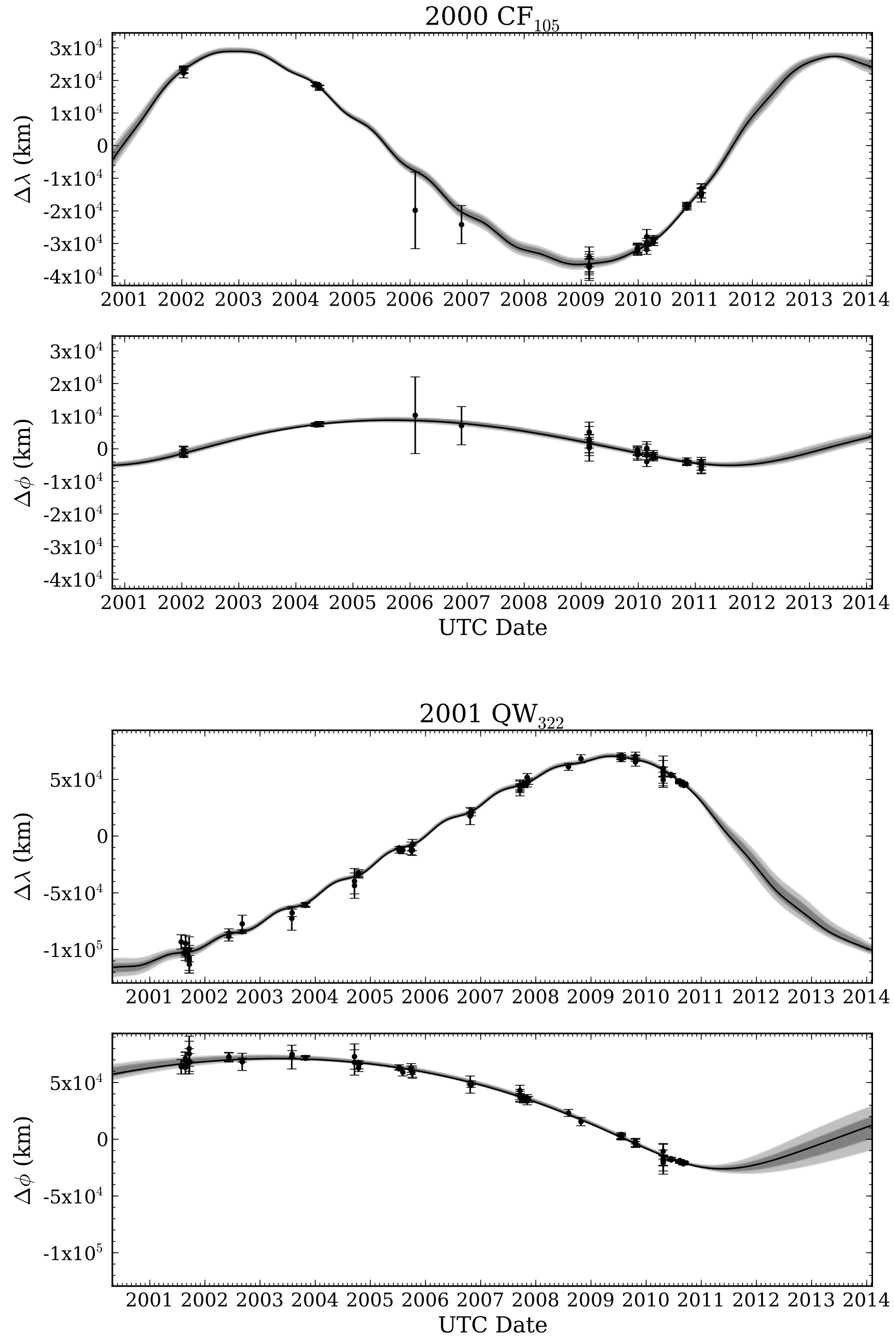

Figure 2.3: Astrometry and fitted mutual orbits for MPC binaries 2000 CF$_{105}$ and 2001 QW$_{322}$. Latitude separation ($\Delta\phi$) and longitude separation ($\Delta\lambda$) are given in projected physical units (km) to remove variation due to changing separation between binary system and the observer and illustrate physical scale of each system. Black line indicates best-fit mutual orbit, while dark and light gray regions illustrate orbits consistent at the 68% and 95% confidence level, respectively.

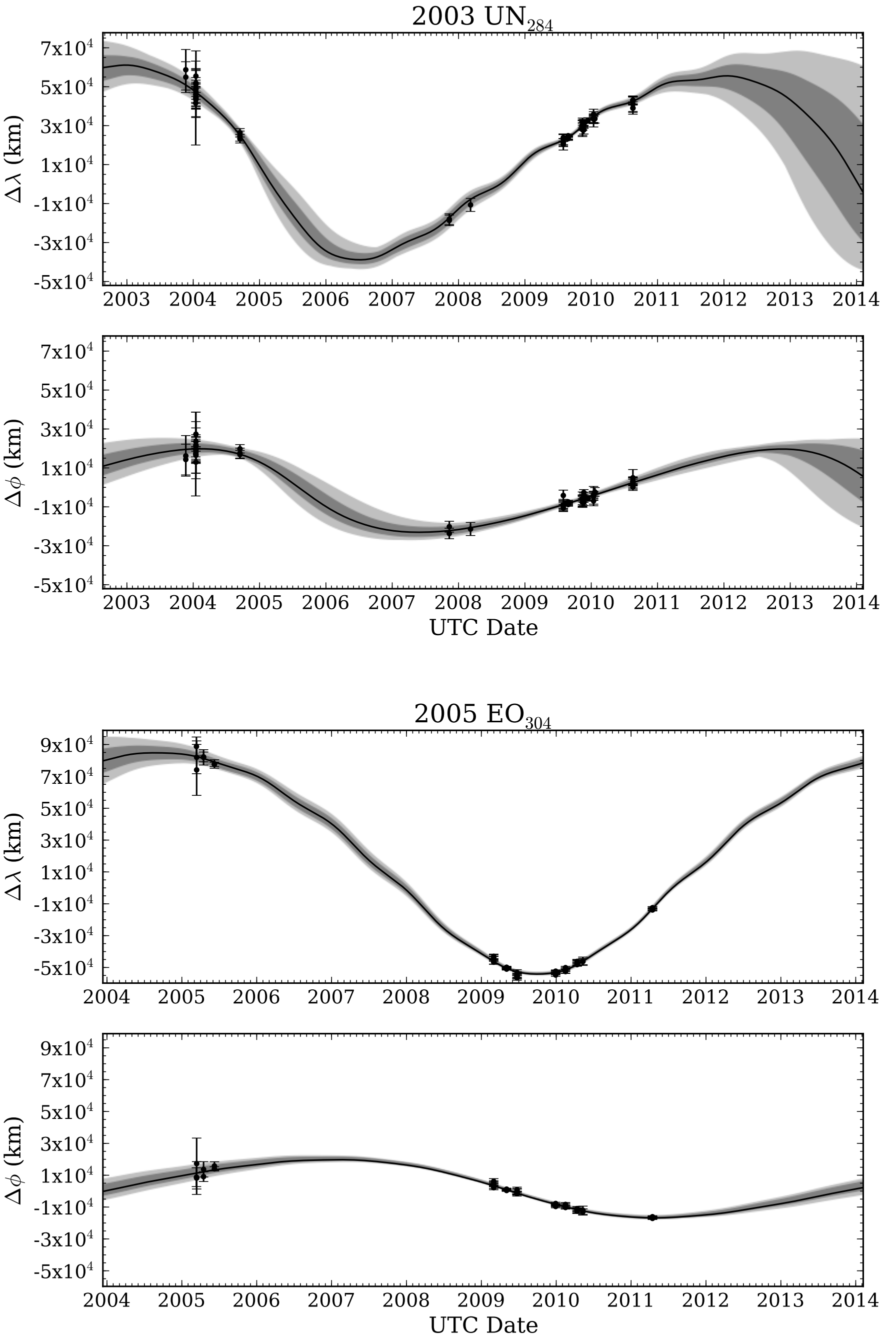

Figure 2.4: Same as Figure 2.3, but for MPC binaries 2003 UN$_{284}$ and 2005 EO$_{304}$.

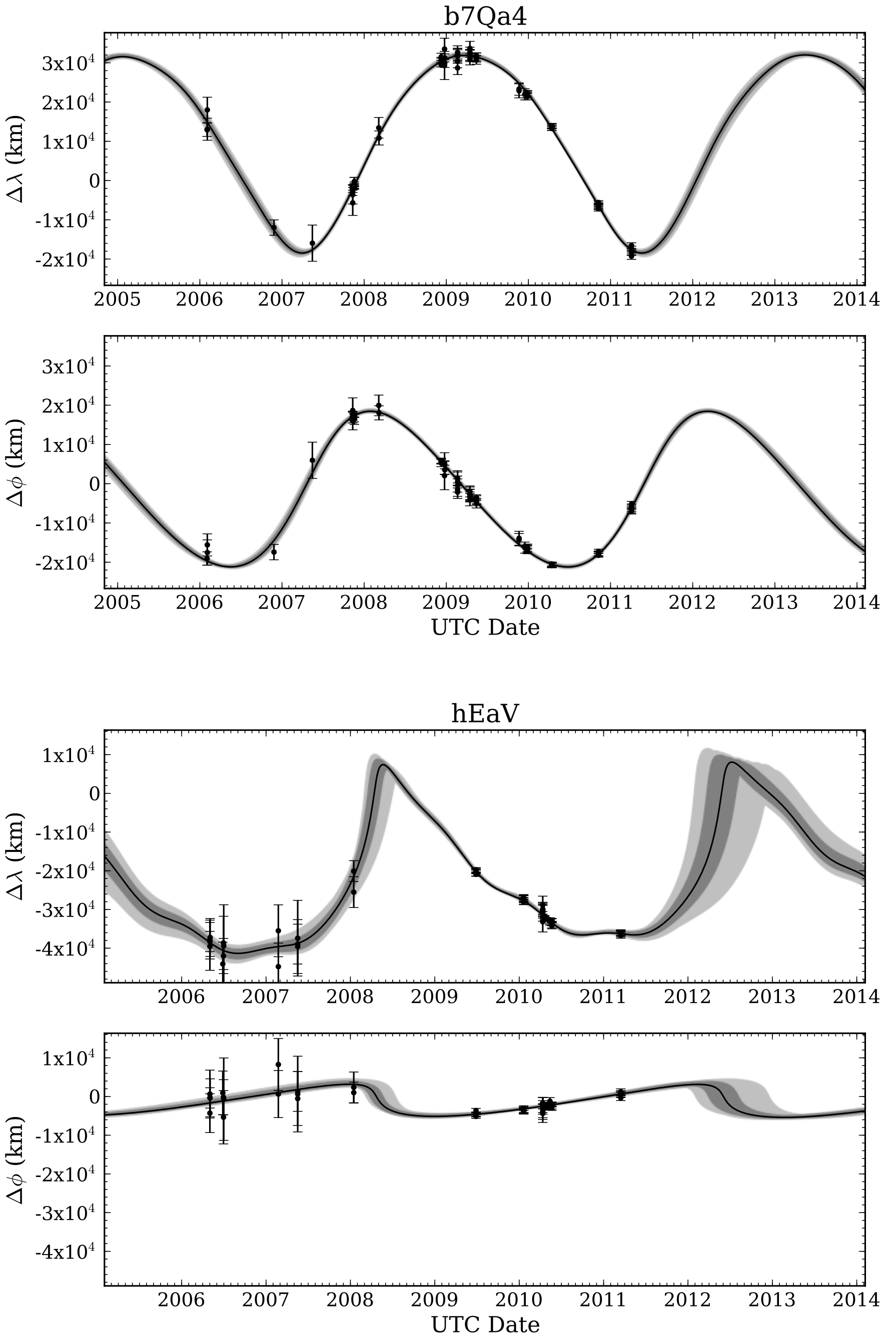

Figure 2.5: Same as Figure 2.3, but for the three CFEPS binaries b7Qa4 and hEaV.

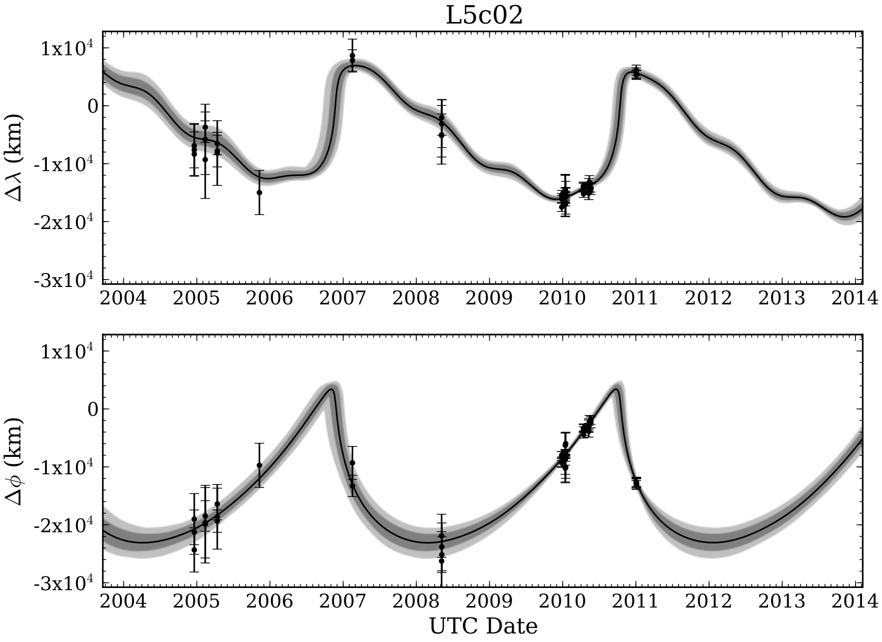

Figure 2.6: Same as Figure 2.3, but for the CFEPS binary L5c02.

we chose these to be the following: mutual semi-major axis (a_m), eccentricity (e_m), period (T_m), Mean Anomaly (M, valid at a defined JD), inclination (i_E), longitude of the ascending node (Ω_E), and argument of pericenter (ω_E). The last three angular parameters are defined with respect to the J2000 Ecliptic. For nearly circular orbits, M and ω become degenerate and alternate choice of basis is preferred; however, we were not presented with a circumstance where altering the basis used in our code was merited, as the binaries we observed all have significant eccentricity. For all orbit fits, 15 Metropolis algorithm threads are run simultaneously, and each compare their final best-fit value and sampled orbit space to identify the global best-fit and statistically acceptable range of parameters after an additional test of the error distribution.

Since our estimates of the astrometric uncertainty of each observation may not reflect their true distribution, (i.e., we don't know the properties of the distribution of errors on the individual measurements *a priori*), we perform a test to bootstrap the 68% and 95% confidence intervals for the χ^2 distribution. This test simply assumes that the best-fit orbit is the "truth," and estimates the observed error distribution around the best-fit by bootstrap-resampling (with replacement) the observations 10,000 times. After each resampling, a new "observed" χ^2 is calculated based off of the resampled observations and the best-fit orbit. After this process, we are left with a distribution of possible best-fit χ^2 values which "might have been." We find the 68% and 95% upper confidence intervals on this distribution, and set those to be our χ^2 thresholds for statistically acceptable mutual orbit fits. Orbits that fall below these χ^2 thresholds are saved, and their distribution is used to generate the uncertainties for each orbital parameter. This analysis has led to extremely well-behaved fitting behavior, with consistently nested uncertainty contours after every addition of new data to a given fit.

The mutual orbit fitting code was tested by reproducing the orbital parameters for the Pluto-Charon system based on synthetic data generated by the *JPL Horizons* system, and reproducing the orbital parameters of 2001 XR_{254} and 2004 PB_{204} as published in Grundy et al. (2009).

2.5 Present Best-Fit Orbits and Implications

The best-fit and uncertainty (given as the extrema of each parameter from the distribution of orbits allowed at the 68% level of confidence) of all fitted parameters are listed in Table 2.2. Additionally, Table 2.3 contains derived parameters; specifically,

Table 2.2: Fit Mutual Orbit Elements

Name	a_m (10^4 km)	T_m (years)	e_m	i_E ($^\circ$)	Ω_E ($^\circ$)	ω_E ($^\circ$)	M ($^\circ$)	Epoch
2000 CF$_{105}$	$3.33^{+0.05}_{-0.06}$	$10.92^{+0.12}_{-0.10}$	$0.29^{+0.02}_{-0.02}$	$167.4^{+0.6}_{-0.7}$	$223.^{+4}_{-3}$	$296.^{+3}_{-3}$	$262.^{+3}_{-3}$	2454880.96
2001 QW$_{322}$	$10.15^{+0.38}_{-0.14}$	$17.01^{+1.55}_{-0.69}$	$0.46^{+0.02}_{-0.01}$	$150.7^{+0.6}_{-0.6}$	$243.^{+3}_{-4}$	$257.^{+5}_{-10}$	$158.^{+19}_{-10}$	2452117.92
2003 UN$_{284}$	$5.55^{+0.38}_{-0.53}$	$8.73^{+0.65}_{-0.54}$	$0.40^{+0.04}_{-0.07}$	$24.3^{+2.2}_{-1.5}$	$92.^{+6}_{-3}$	$172.^{+10}_{-8}$	$294.^{+5}_{-14}$	2452963.77
2005 EO$_{304}$	$6.98^{+0.20}_{-0.21}$	$9.80^{+0.45}_{-0.45}$	$0.22^{+0.02}_{-0.02}$	$12.4^{+0.8}_{-0.5}$	$259.^{+2}_{-3}$	$206.^{+9}_{-5}$	$193.^{+8}_{-13}$	2453440.94
b7Qa4	$2.53^{+0.03}_{-0.03}$	$4.11^{+0.04}_{-0.03}$	$0.28^{+0.01}_{-0.01}$	$55.6^{+1.3}_{-1.4}$	$41.^{+2}_{-2}$	$14.^{+1}_{-1}$	$219.^{+1}_{-1}$	2455153.08
hEaV	$3.23^{+0.53}_{-0.28}$	$4.11^{+0.15}_{-0.12}$	$0.84^{+0.03}_{-0.02}$	$13.3^{+2.5}_{-1.9}$	$82.^{+5}_{-7}$	$171.^{+2}_{-2}$	$104.^{+9}_{-8}$	2455007.86
L5c02	$2.76^{+0.33}_{-0.28}$	$3.89^{+0.05}_{-0.07}$	$0.90^{+0.02}_{-0.02}$	$134.1^{+4.9}_{-6.1}$	$105.^{+6}_{-8}$	$149.^{+5}_{-6}$	$286.^{+4}_{-3}$	2455190.06

Table 2.3: Derived Values

Name	M_{sys} (10^{17} kg)	a_m/R_H	i_m (°)	ω_m (°)	$q_m/R_P{}^*$
2000 CF_{105}	$1.85^{+0.1}_{-0.14}$	$0.1679^{+0.0012}_{-0.0011}$	$167.9^{+0.6}_{-0.7}$	$295.^{+3}_{-3}$	741^{+29}_{-30}
2001 QW_{322}	$21.50^{+1.44}_{-2.23}$	$0.2222^{+0.0133}_{-0.0061}$	$152.7^{+0.6}_{-0.8}$	$248.^{+6}_{-10}$	855^{+64}_{-40}
2003 UN_{284}	$13.12^{+2.26}_{-2.97}$	$0.1449^{+0.0070}_{-0.0060}$	$22.7^{+2.2}_{-1.4}$	$165.^{+21}_{-8}$	534^{+59}_{-42}
2005 EO_{304}	$21.03^{+0.87}_{-0.74}$	$0.1553^{+0.0048}_{-0.0047}$	$15.7^{+0.8}_{-0.5}$	$203.^{+9}_{-5}$	714^{+7}_{-6}
b7Qa4	$5.70^{+0.17}_{-0.20}$	$0.0879^{+0.0005}_{-0.0005}$	$54.6^{+1.3}_{-1.4}$	$13.^{+1}_{-2}$	408^{+8}_{-7}
hEaV	$11.83^{+7.09}_{-3.18}$	$0.0900^{+0.0021}_{-0.0018}$	$11.1^{+2.5}_{-2.0}$	$158.^{+4}_{-4}$	84^{+10}_{-18}
L5c02	$8.30^{+3.35}_{-2.15}$	$0.0809^{+0.0007}_{-0.0009}$	$133.3^{+4.9}_{-4.8}$	$147.^{+5}_{-6}$	56^{+10}_{-10}

*: Primary radius R_P assumes $\rho = 1$ gram cm^{-3}.

the system mass M_{sys}, mutual semi-major axis to Hill-radius fraction a/R_H, mutual inclination i_m, mutual argument of pericenter ω_m, and mutual pericenter separation in multiples of primary radii q_m/R_p. Figure 2.7 illustrates the a/R_H, e_m, and i_m fits and the 68% and 95% uncertainties in these parameters for each system.

The astrometric measurements for each system and comparison to fit orbits are illustrated in Figures 2.3—2.6. These figures project each system onto the sky plane in physical separation units, removing the variation in the observed scale of the systems due to the change in the observer-system separation over the course of a year.

2.5.1 Derived Parameters

In the following section, we describe the derived mutual orbital parameters listed in Table 2.3 and illustrated in Figure 2.7. System mass is simply calculated from Kepler's laws,

$$M_{sys} = 4\pi^2 \frac{a_m^3}{G T_m^2}. \tag{2.1}$$

while the classical Hill radius for a binary in orbit around the Sun is defined as

$$R_H = a_{\text{out}}(1 - e_{\text{out}}) \left(\frac{M_{sys}}{3 M_\odot} \right)^{\frac{1}{3}}, \tag{2.2}$$

where a_{out} and e_{out} is are the heliocentric semi-major axis and eccentricity of the binary system's barycenter. Primary radius is found from the system mass by assuming that both components have the same albedo and density, and is given by

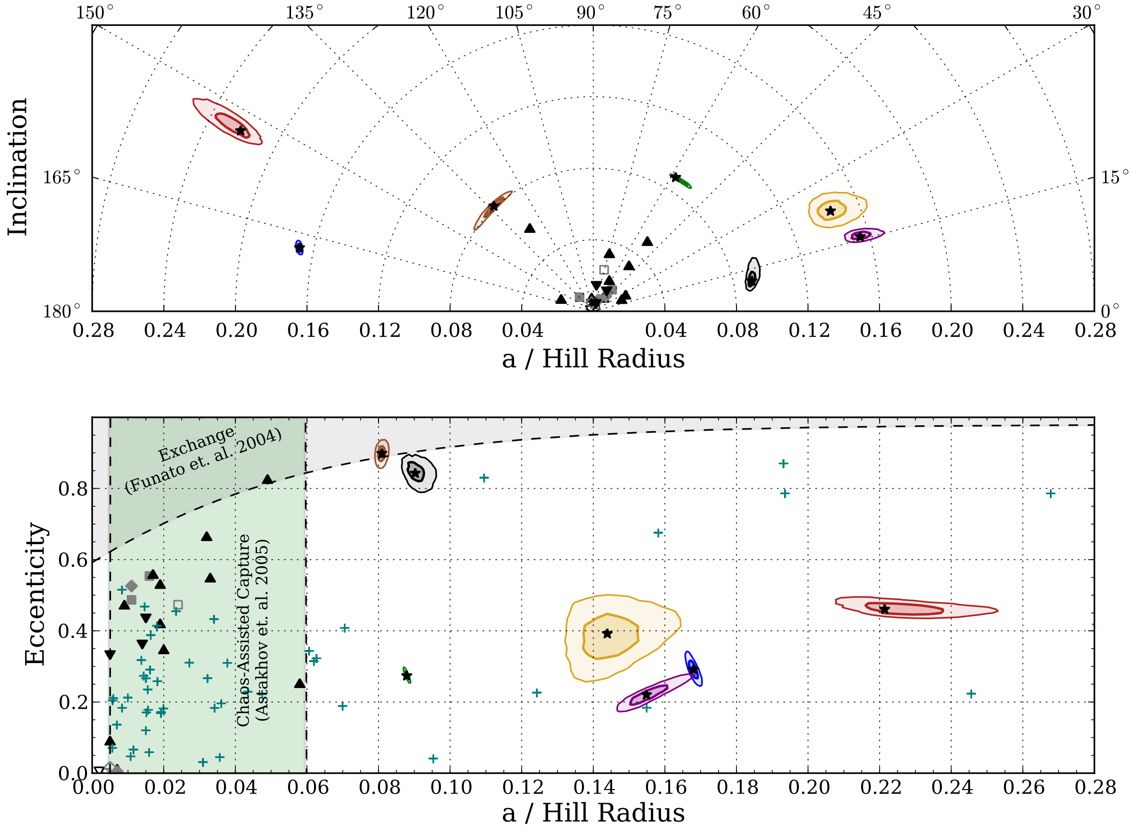

Figure 2.7: Best-fit mutual orbit properties. Blue: 2000 CF$_{105}$, Red: 2001 QW$_{322}$, Yellow: 2003 UN$_{284}$, Purple: 2005 EO$_{304}$, Green: b7Qa4, Gray: hEaV, Brown: L5c02. Heavy and light contours represent 68% and 95% confidence intervals, respectively, while black stars mark the best-fit parameters. Teal "+" symbols mark sample of synthetic systems created by gravitational collapse in Nesvorný et al. (2010), selecting simulations with $\Omega = 0.5 - 1.0\Omega_{circ}$ (initial clump rotation), and $f^* = 10 - 30$ (cross-section modifier). Gray shaded region represents properties of binary systems created by three-body exchange reactions in Funato et al. (2004). Green shaded region represents properties of binary systems created by Chaos-Assisted Capture in Astakhov et al. (2005). Other points represent TNBs with known orbits (Grundy et al. 2011). Black points are members of the Classical belt, gray points are members of other dynamical populations. Filled points indicate $\Delta m < 1.7$, and open points indicate $\Delta m > 1.7$. Upward triangles indicate CC objects, while downward triangles indicate HC objects. Square points indicate resonant objects, and diamond points indicate Centaurs or scattered disk objects. Non-preferred degenerate pole solutions are not illustrated for literature binaries.

$$R_p = \left(\frac{3}{4\pi\rho(1+10^{\frac{-3\Delta m}{5}})} M_{sys} \right)^{\frac{1}{3}}, \tag{2.3}$$

where ρ is the adopted bulk density and Δm is the magnitude difference between the primary and secondary components of the binary.

Mutual inclination is the angle between the pole vector of the binary mutual orbit $\vec{P_m}$ and that of the outer Heliocentric orbit $\vec{P}_{\text{out}}$, and can be found by $i_m = \cos^{-1}(\vec{P}_{\text{out}} \cdot \vec{P_m})$. The pole vectors for either orbit can be found by (eg., Naoz et al. 2010):

$$\vec{P} = \begin{pmatrix} \sin(\Omega)\sin(i) \\ -\ \cos(\Omega)\sin(i) \\ \cos(i) \end{pmatrix}.$$

The mutual argument of pericenter ω_m (critical for estimating the extent of Kozai oscillations) is the angle between the ascending node (with respect to the outer Heliocentric orbit) and pericenter in the plane of the mutual orbit. It can be found by:

$$\omega_m = \cos^{-1}\left(\frac{\vec{e}_m \cdot \vec{n}}{|\vec{e}_m||\vec{n}|} \right) \frac{\vec{e}_m[z]}{|\vec{e}_m[z]|},$$

where

$$\frac{\vec{e}_m}{|\vec{e}_m|} = \begin{pmatrix} \cos(\omega_E)\cos(\Omega_E) - \sin(\omega_E)\cos(i_E)\sin(\Omega_E) \\ \cos(\omega_E)\sin(\Omega_E) + \sin(\omega_E)\cos(i_E)\cos(\Omega_E) \\ \sin(\omega_E)\sin(i_E) \end{pmatrix},$$

and $\vec{n} = \vec{P}_{\text{out}} \times \vec{P_m}$.

2.5.2 Kozai Cycles

Systems within a broad range of i_m centered on 90° may be subject to large oscillations in i_m and e_m due to the Kozai effect. This effect is caused by a torque on the quadrupole moment of the binary system, and over the oscillation cycles two values are conserved; one depending on the initial mutual eccentricity and inclination, and the other depending on both these and the mutual argument of pericenter. Following Perets & Naoz (2008), we adopt the following form for these two conserved values:

Table 2.4: Kozai Oscillations

Name	$e_{\max}$	$e_{\min}$	$q_{\min}/R_p{}^*$
2001 QW_{322}	$0.477^{+0.012}_{-0.006}$	$0.342^{+0.017}_{-0.009}$	830^{+36}_{-29}
2003 UN_{284}	$0.45^{+0.04}_{-0.07}$	$0.39^{+0.04}_{-0.08}$	486^{+57}_{-42}
b7Qa4	$0.72^{+0.02}_{-0.02}$	$0.263^{+0.009}_{-0.010}$	155^{+15}_{-13}
L5c02	$0.94^{+0.01}_{-0.02}$	$0.70^{+0.06}_{-0.08}$	31^{+9}_{-7}
2000 CF_{105}	$0.29^{+0.02}_{-0.02}$	$0.28^{+0.02}_{-0.02}$	739^{+29}_{-29}
2005 EO_{304}	$0.24^{+0.02}_{-0.03}$	$0.22^{+0.02}_{-0.03}$	698^{+7}_{-6}
hEaV	$0.85^{+0.03}_{-0.02}$	$0.84^{0.03}_{-0.02}$	82^{+10}_{-18}

*: Primary radius R_P assumes $\rho = 1$ gram cm^{-3}.

$$A = \left(5e_m^2 \sin^2 \omega_m + 2(1 - e_m^2)\right) \sin^2 i_m \tag{2.4}$$

and

$$B = \sqrt{1 - e_m^2} \cos i_m. \tag{2.5}$$

With some algebraic manipulation and the constraint that eccentricity and inclination minima and maxima occur when $\omega_m = 0°$ or $90°$, these two constants determine the maximum and minimum eccentricity and inclination reached by a given binary system during its Kozai cycle. We calculate these values, and the amplitudes of the eccentricity excursions experienced by each binary system is listed in Table 2.4. Also listed are the predicted minimum pericenter separations (occurring during the highest eccentricity phase of the Kozai cycle) in multiples of primary radii, as close encounters during Kozai cycles may lead to modification of the mutual orbit due to tidal friction (Fabrycky & Tremaine 2007, Perets & Naoz 2009, Brown et al. 2010). Details of systems with large-amplitude Kozai oscillations will be discussed on an object-by-object basis in the following sections.

The Kozai effect can be easily suppressed by other effects, including permanent asymmetries in the mass distribution of the component bodies (Ragozzine 2009). However, this suppression only occurs for relatively small semi-major axes, and therefore the Kozai oscillations of these wide systems are unlikely to be suppressed.

2.5.3 Individual Objects

2000 CF$_{105}$

With several epochs of HST data, and nearly nine years of observational baseline (covering most of a single 11 year mutual orbit period), 2000 CF$_{105}$ has one of the best-measured orbits in our sample with mutual semi-major axis and period uncertainties at the 1% level. It is also the lowest-mass system in our sample, and the second-most weakly bound (behind only 2001 QW$_{322}$). Because of its low mass (currently the lowest mass of any known TNB), this system has the smallest estimated primary radius of any system in our sample (assuming all objects share a common density), estimated to be $31.8^{+0.6}_{-0.8}$ km given a bulk density of 1 gram cm^{-3}.

2000 CF$_{105}$ is not subject to strong Kozai oscillations, and its pericenter separation is always greater than ~ 710 primary radii, so there is little chance of mutual tides having modified its mutual orbit.

The pole solution for 2000 CF$_{105}$ is non-degenerate at greater than 95% confidence, and the system is retrograde. Its mutual pole vector is only $\sim 12.1^{\circ}$ degrees from being anti-aligned with its outer orbit's pole vector, making one of the most pole-parallel systems known.

2001 QW$_{322}$

At the outset, our current results for the mutual orbit of 2001 QW$_{322}$ appear inconsistent with the orbit published in Petit et al. (2008). By fitting only the astrometric data used in that publication with our new code, we find a much larger range of allowable mutual orbit solutions than was presented in the previous study. This is especially notable for allowing much higher values of mutual eccentricity. This larger range of allowed orbital parameters completely overlaps with our current orbit fit, as illustrated in Figure 2.8. We suspect that the difference is due to two factors: our more thorough fitting algorithm and our different statistical analysis of the allowed χ^2 range. The allowed χ^2 range in Petit et al. (2008) was much smaller than that determined by the methods used here.

The components of this system remain photometrically indistinguishable, with Δm consistent with 0. When making astrometric measurements, we have arbitrarily assigned the Northernmost object in the discovery epoch as the system primary. Observations have been frequent enough that there is no possibility for confusion between system components, based on continuity of the orbital motion.

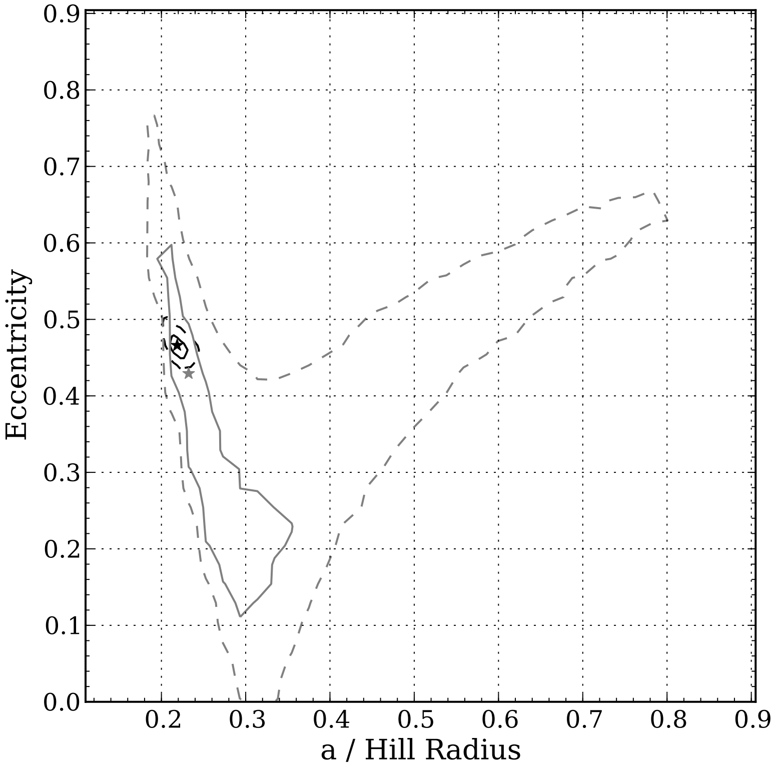

Figure 2.8: Comparison of the allowed orbits for 2001 QW_{322}, given the data presented in Petit et al. 2008 (gray contours) and the complete set of data used in this work (black contours) using the fitting algorithm described in the text. Stars mark best-fit orbits. 68% and 95% confidence intervals are marked by the solid and dashed contours, respectively.

The observations in our dataset cover approximately nine years, sampling slightly over 50% of the best-fit mutual orbital period of 17.0 years. Because the observations have been frequent and of high quality, this limited sample of the orbital motion of the system is very constraining. Mutual semi-major axis, period, and eccentricity are all known to better than 10% accuracy. Angular and derived parameters are similarly well known.

2001 QW_{322} is subject to strong Kozai oscillations, with the nominal best-fit orbit implying eccentricity variations between $0.342 \lesssim e_m \lesssim 0.477$. Its current orbit is therefore near its highest eccentricity phase.

In physical units, this system remains the most widely separated binary minor planet known, with a mutual semi-major axis of $1.015^{+0.038}_{-0.014} \times 10^5$ km. It is also likely the most weakly bound binary minor planet known, with its measured a/R_H of $0.2222^{+0.0133}_{-0.0061}$ exceeding the current estimate for the outer satellite of the Main-Belt asteroid (3749) Balam of $a/R_H \sim 0.2$ (Marchis et al. 2008). Several other known main-belt asteroid binaries have estimates of a/R_H shown in Richardson & Walsh (2006) which are similar to or slightly higher than that measured for 2001 QW_{322}, but these estimates are based on single-epoch observations and may not reflect the true orbits and masses of these systems.

The pole solution for 2001 QW_{322} is non-degenerate at greater than 95% confidence, and the system is retrograde with a mutual inclination of $\sim 152.7°$.

2003 UN_{284}

The orbit of 2003 UN_{284} is the least-well constrained in our sample. The fit relies heavily on astrometry published in Kern (2006) for pinning the 2003—2004 astrometry, and only three data points constrain the 2005—2008 astrometry. Recent data have proved relatively discriminatory, and the mutual semi-major axis and period are both known to better than 10% accuracy, but the derived system mass is only constrained to $\sim 20\%$ accuracy. The Δm we adopt for 2003 UN_{284} is determined from two well-resolved visits from Gemini North. Kern (2006) finds a highly variable Δm for this system, suggesting one or both components may have a significant lightcurve, and our adopted Δm may not reflect this variability.

This system is likely subject to minor Kozai oscillations, but the amplitude of these oscillations is comparable to the uncertainty in the currently measured mutual eccentricity. The pole solution for 2003 UN_{284} is non-degenerate at greater than 95%

confidence, and the system is prograde with a mutual inclination of $\sim 22.7^\circ$.

2005 EO$_{304}$

The orbit of 2005 EO$_{304}$ also relies heavily on astrometry published in Kern (2006), and it has the fewest observed epochs (12) of any of our systems. Nevertheless, the recent measurements from *VLT* and *Gemini* have provided reasonably tight constraints on it's orbital properties.

This system has the largest Δm in our sample at 1.45 in r'. It also has the largest primary radius (assuming all objects share a common density), which we estimate to be $76.2^{+1.0}_{-0.9}$ km given a bulk density of 1 gram cm^{-3}.

2005 EO$_{304}$ is not subject to significant Kozai oscillations, and its minimum pericenter separation is at least 692 primary radii. The pole solution for 2005 EO$_{304}$ is non-degenerate at greater than 95% confidence, and the system is prograde with a mutual inclination of $\sim 15.7^\circ$, making it one of the lowest mutual inclination systems known.

b7Qa4

Nearly all observations of b7Qa4 used in our astrometric fit come from *Gemini*, and the orbit has been sampled for just over a single orbital period. Its orbit is very well constrained, with mutual semi-major axis and period known to 1% accuracy and mutual eccentricity to better than 4% accuracy. The pole solution for b7Qa4 is non-degenerate at greater than 95% confidence, and the system is prograde with a mutual inclination of $\sim 54.6^\circ$, making it the most inclined system in our sample.

b7Qa4 is subject to strong Kozai oscillations, with the nominal best-fit orbit implying eccentricity variations between $0.72 \leq e_m \leq 0.26$. Its current orbit is therefore near the lowest point of its eccentricity cycle. Its pericenter passages are still widely separated (never lower than 143 primary radii) and mutual tides are not a concern for this system.

L5c02

The observations of L5c02 cover well over a single orbital period, though as Figure 2.5 illustrates its on-sky behavior is quite complex and well time-sampled observations were necessary to accurately constrain this system's mutual orbital properties.

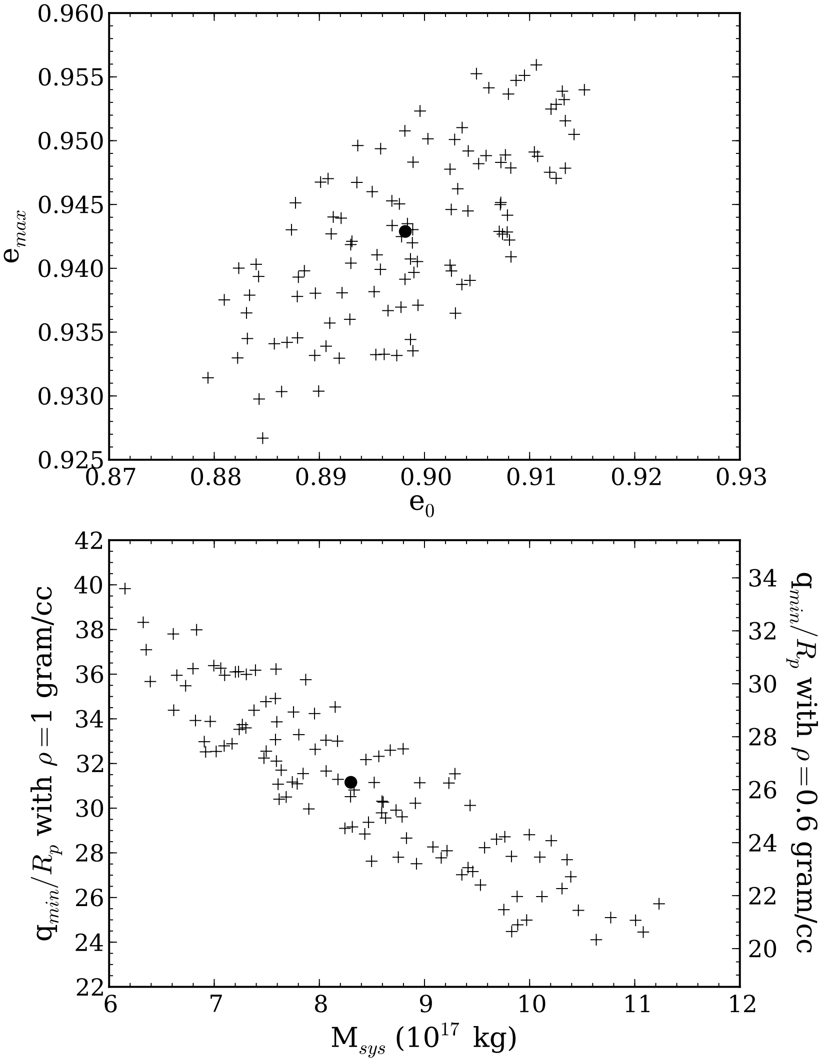

Figure 2.9: Features of L5c02's Kozai oscillations. Top panel: representative sample of 107 orbits consistent with L5c02 astrometry at 1σ level, showing their current eccentricity (e_0) and the maximum eccentricity (e_{max}) they reach over the course of a Kozai cycle, with the best-fit orbit marked by the large point. Bottom panel: Same sample of orbits, but now illustrating their best-fit system mass (M_{sys}) and the minimum pericenter separation in multiples of primary radii (q_{min}/R_p, assuming $\rho = 1$ gram cm^{-3}).

This system has the highest well-measured mutual eccentricity of any binary minor planet, at $e_m = 0.90^{+0.02}_{-0.02}$. The orbit of the outermost satellite of the trinary asteroid (3749) Balam has been estimated to rival this at $e_m \sim 0.9$ (Marchis et al. 2008), but its value is poorly constrained. A fascinating consequence of this extreme mutual eccentricity is that over the course of its mutual orbit, the secondary of L5c02 will subtend an angle ranging from to $\sim 0.1^\circ$ (at mutual apocenter) to $\sim 1.7^\circ$ (at mutual pericenter) as viewed from the surface of the primary — from one-fifth to over three times the angular size of the Moon on the sky.

L5c02 may be subject to strong Kozai oscillations, with the nominal best-fit orbit implying eccentricity variations between $0.70 \lesssim e_m \lesssim 0.94$. Its current orbit is therefore near its highest eccentricity phase. The pole solution for L5c02 is non-degenerate at greater than 95% confidence, and the system is retrograde with a mutual inclination of $\sim 134^\circ$. This system is also the most tightly bound in our sample, with $a/R_H \simeq 0.0809$. Because of the orbits' high eccentricity, the error distributions in a_m and T_m conspire to produce a large uncertainty in the derived system mass, and M_{sys} remains uncertain at the 40% level.

The high mutual eccentricity phases of L5c02's Kozai cycles lead to very close passages between the primary and secondary. At its current mutual eccentricity, pericenter passages occur at 56^{+10}_{-10} primary radii (again given a bulk density of 1 gram cm^{-3}), which may be wide enough that mutual tides do not cause orbital modification. However, during the high eccentricity phase of its Kozai cycle, the pericenter separation of L5c02 drops much lower to 31^{+9}_{-7}. Figure 2.9 illustrates the distribution of mutual pericenter separation versus system mass. If we argue that L5c02 must have survived roughly in its current orbital configuration for the age of the solar system, then we would prefer higher minimum pericenter separations to keep the system from experiencing tidal evolution. From Figure 2.9 we see that orbit fits which have higher pericenter separations are lower-mass solutions. However, the tidal evolution of highly eccentric, highly inclined binary systems is poorly understood, and future work is merited to determine if limiting the tidal evolution of L5c02 would provide useful priors for further constraining its mutual orbit.

hEaV

The observations of hEaV span slightly more than a single period, and Figure 2.5 illustrates that like L5c02 the on-sky behavior of this system is also complex. This system is also very highly eccentric, at $e_m = 0.84^{+0.03}_{-0.02}$, making it the second-highest eccentricity TNB known behind L5c02. Its mutual semi-major axis remains somewhat poorly constrained at 16% uncertainty, while the mutual period is known to better than 5% uncertainty. The derived system mass remains highly uncertain for the same reason as L5c02, and uncertainties in M_{sys} remain at the 40% level.

The pole solution of hEaV is non-degenerate at the 95% level, and the system is prograde with the lowest mutual inclination of any known TNB at just $\sim 11°$. Due to this low inclination, hEaV is not subject to notable Kozai oscillations. Despite its high eccentricity and relatively large primary (61^{+10}_{-6} km), mutual pericenter passages are always at least 64 primary radii, making this system much less susceptible to possible mutual tidal effects than L5c02.

2.5.4 Ensemble Results

Comparison to Other Populations

Comparing the TNBs studied here to previously characterized TNBs, we see that they are much more widely separated in terms of their Hill sphere occupation. Figure 2.7 illustrates the mutual semi-major axis to Hill radius fraction for the ultra-wide TNBs characterized in this work and the systems listed in Grundy et al. (2011); the widest known TNB with a well-characterized orbit not in our sample is Teharonhiawako/Sawiskera at $a/R_H \sim 0.06$.

Grundy et al. (2011) showed that the previously known widely-separated, loosely-bound TNBs are only found on dynamically cold heliocentric orbits. Here we seek to confirm this relationship, and identify which dynamical population hosts the wide binaries; is it the cold Classical Kuiper Belt, or can a low-inclination extension of the hot Classical Kuiper Belt plausibly host the widely-separated binary systems? Figure 2.10 illustrates the outer orbital excitation (given by $\sqrt{\sin(i_{\mathrm{out}})^2 + e^2_{\mathrm{out}}}$) versus a/R_H. As in Grundy et al. (2011), we confirm that only dynamically cold populations host wide binaries. Further, systems with pericenters which suggest current or past encounters with Neptune have relatively low a/R_H, supporting the destructive nature of such encounters presented by Parker & Kavelaars (2010). To quantify the difference between the binaries found in dynamically cold and hot populations, we compare the a/R_H distributions of binaries falling into our CC classification with all other binaries. We find that these two samples are inconsistent with being drawn from the same a/R_H distribution, with the KS test rejecting this hypothesis at greater

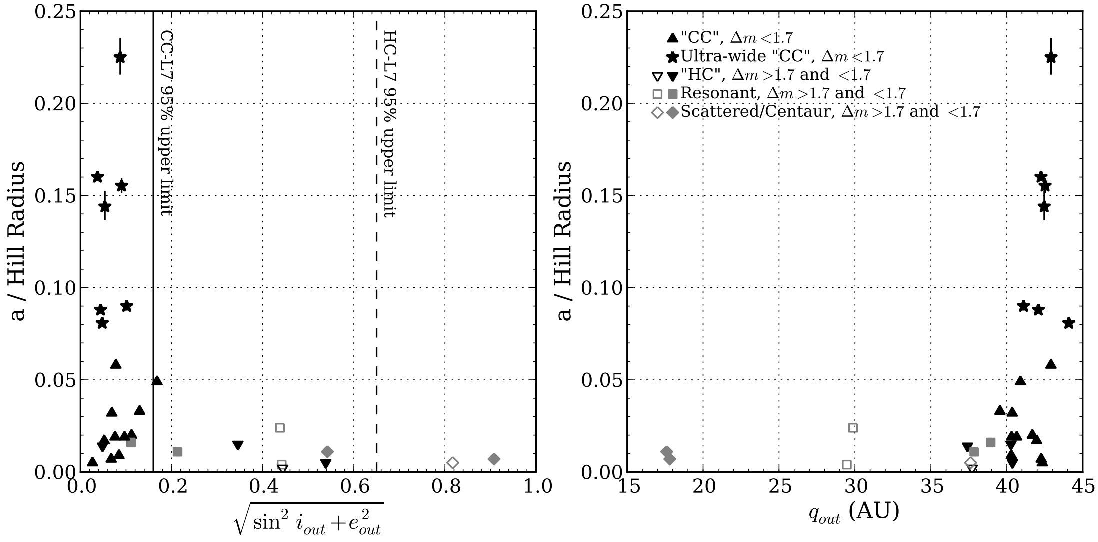

Figure 2.10: Left panel: Heliocentric orbital excitation vs. a/R_H (similar to Fig. 5 from Grundy et al. 2011). Triangle, square, and diamond points have same meaning as in Figure 2.7, representing orbits published in Grundy et al. (2011). Stars mark best-fit orbits for the ultra-wide TNBs characterized in this work, with errorbars representing 68% confidence interval. Vertical lines mark upper 95th-percentile of the orbital excitation of the cold Classical Kuiper Belt (solid) and hot Classical Kuiper Belt (dashed), as found by the CFEPS L7 survey. Right panel: heliocentric pericenter q_{out} vs. a/R_H.

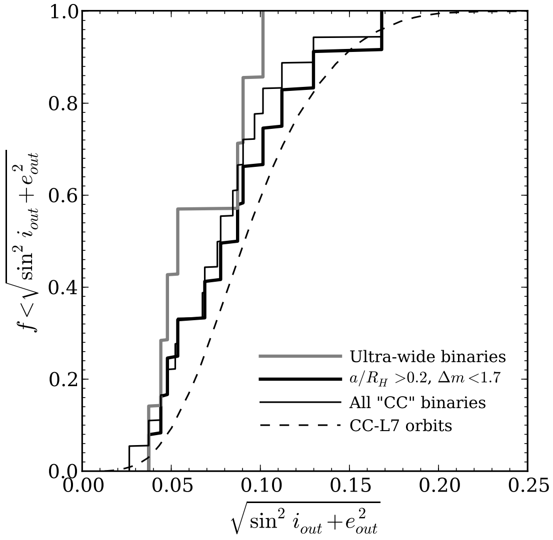

Figure 2.11: Cumulative histograms of heliocentric orbital excitation for different binary sub-samples, compared to model distributions. Left panel: All CC binaries (heavy solid histogram), just the ultra-wide binaries (gray histogram), and all binaries with $a/R_H > 0.02$ and $\Delta m < 1.7$ (light black histogram), compared to the CC-L7 model distribution (dashed line). Right panel: All HC binaries (solid histogram) compared to the HC-L7 distribution (dashed histogram). We stress that this plot is comparing a heavily biased sample (binaries) with a de-biased model, and is only used for consistency checks.

than 99.9% confidence. Therefore, the binaries which fall into our crude dynamical classification of the cold Classical Kuiper Belt have distinctly different characteristics than binaries hosted in other populations.

To further clarify the host population of the wide binaries, we compare the outer orbital excitation distribution of the binaries with the distribution of the CC-L7 and HC-L7 orbital excitations. The distribution of orbital excitations for these binary samples and the L7 model populations are illustrated in Figure 2.11. Since most binaries considered here have been discovered in near-ecliptic surveys, there is significant bias against the detection of high inclination binaries. The bias is less significant when considering low inclination populations, so comparisons between the biased CC binary sample with the de-biased CC-L7 model population are reasonably fair. Comparing the CC binary sample to just the low inclination objects in the de-biased HC-L7 model population is also meaningful, as observational biases are not significant for the low-inclination extension of the HC-L7 population. We use the KS test to determine if we can reject the following two hypotheses: that the CC binaries are drawn from the CC-L7 orbital excitation distribution, or that the CC binaries are drawn from the excitation distribution of low-inclination ($i_{\text{out}} \leq 5°$) HC-L7 orbits. Additionally, we determine whether just the seven ultra-wide binaries characterized in this work (with no outer orbit constraints placed on them) could be drawn from the CC-L7 or $i_{\text{out}} \leq 5°$ HC-L7 excitation distributions, and whether *all* binaries with $a/R_H > 0.02$ and $\Delta m < 1.7$ could be drawn from the same excitation distributions.

We rule out ($P < 0.001$) that the CC binaries are drawn from any subset of the HC-L7 excitation distribution, while it is plausible (KS test cannot reject at high confidence) that they are drawn from the CC-L7 excitation distribution. We also find that, without any prior cuts on heliocentric orbits, neither the seven ultra-wide binaries characterized in this work nor all binaries with $a/R_H > 0.02$ and $\Delta m < 1.7$ can be drawn from the low-inclination HC-L7 excitation distribution ($P < 0.001$ in both cases), while both can be plausibly drawn from the CC-L7 excitation distribution. This further confirms that wide binaries are intimately linked to the dynamically cold population of the Classical Kuiper Belt — it cannot be that they are predominantly hosted by a low-inclination extension of the hot Classical Kuiper Belt.

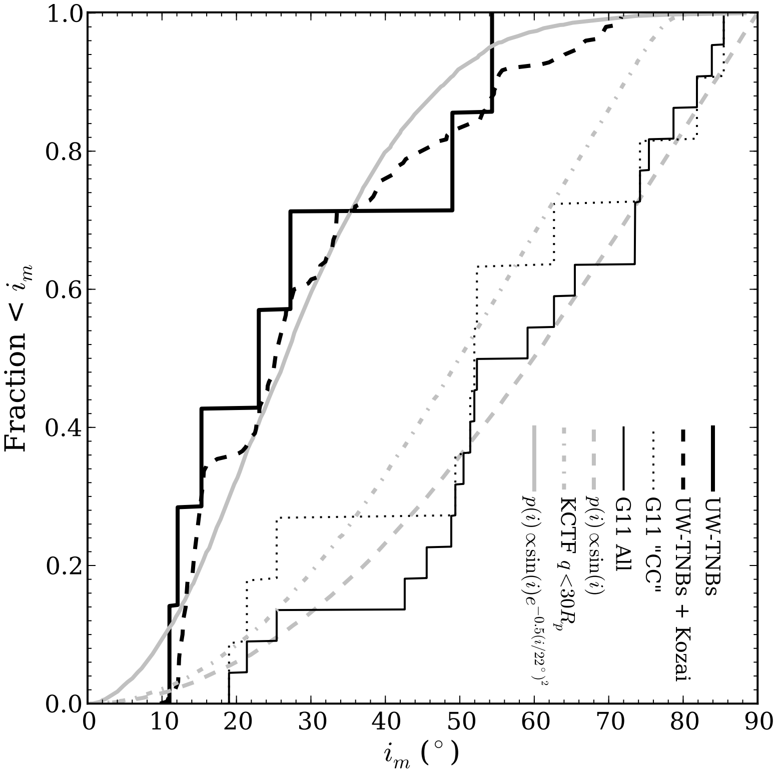

Figure 2.12: Cumulative mutual inclination distribution of ultra-wide binaries characterized in this work (heavy black histogram), tight binaries from literature (light black histogram), and tight CC binaries from literature (dotted black histogram). Retrograde inclinations are folded over onto the range of 0°—90°. Dashed black line shows ultra-wide binaries' inclinations when smoothed over entire Kozai cycle of each object. Gray dashed line: uniform distribution — $P(i) \propto sin(i)$. Grey dash-dotted line: uniform distribution modified by removing any orbits with Kozai cycles which drive $q_{\rm min} \leq 30R_p$ as described in the text. Gray solid line: inclination distribution of form $P(i) \propto \sin(i) e^{-0.5(i/22^\circ)^2}$.

Mutual inclination distribution

The mutual inclination of a TNB system is one of the most challenging parameters to measure, as there is a mirror degeneracy in the pole solution which can only be broken after sufficient time has elapsed for the observer's viewing geometry of the binary system has changed enough to discern the system's true orientation. However, the distribution of mutual inclinations and the ratio of prograde to retrograde orbits holds significant implications for formation scenarios (Schlichting & Sari 2008b, Noll et al. 2008b) and for the ongoing evolution of the binary orbit (Fabrycky & Tremaine 2007, Perets & Naoz 2009). As illustrated in Figure 2.7, all seven systems characterized here now have non-degenerate pole solutions: four prograde and three retrograde. The prograde-to-retrograde ratio and its 95% Poisson counting uncertainty for the ultra-wide TNBs is therefore $\sim 1.33^{+4.55}_{-1.02}$. If we fold in the systems with non-degenerate pole solutions presented in this work and those in Grundy et al. (2011) which fall into our CC sub-sample and meet our near-equal mass criteria, we find that the ensemble prograde-to-retrograde ratio for dynamically cold, near-equal mass TNBs is $1.60^{+2.96}_{-0.99}$.

The distribution of the mutual orbit inclinations of the ultra-wide binaries is illustrated in Figure 2.12, along with the inclination distribution of tightly-bound TNBs in literature, taken from the orbits compiled by Grundy et al. (2011). Due to the relative lack of high-inclination and excess of low-inclination of wide binaries, we find it highly unlikely that the wide binaries' inclinations are drawn from the same inclination distribution as the tighter TNBs, with the Kolmogorov-Smirnov (KS) test rejecting this hypothesis at $> 95\%$ confidence. Additionally, we find that the tight binaries in literature are consistent with having their inclinations drawn from a uniform distribution ($P(i) \propto sin(i)$, with the KS test rejecting this hypothesis at only $\sim 6\%$ confidence), while the ultra-wide TNBs' inclinations are inconsistent with being drawn from the same uniform distribution (KS test rejecting this hypothesis at $\sim 99\%$ confidence). A simple way to understand the strength of this rejection is to note that in a uniform inclination distribution, 50% of the inclinations are $> 60°$, while there are no systems in our sample with inclinations so high. Since the probability of randomly drawing an inclination $< 60°$ is 0.5 each time, after sampling seven systems the probability of every system having inclination $< 60°$ is the same as landing seven coin flips head-up in a row, $0.5^7 \simeq 0.008$.

When restricting the tightly-bound literature binaries to only those in the CC sample, the significance of the rejection of the wide binaries being drawn from the same distribution drops to only $> 89\%$ — however, the dynamically cold binaries from literature remain consistent with a uniform distribution (KS test rejecting this hypothesis at only 40% confidence).

It should be noted that observational bias works against the detection of low inclination systems (with respect to the Ecliptic), as they present edge-on geometry and their average projected separations are lower than high inclination systems. Thus, our relative lack of high inclination objects is not due to observational bias.

When considering all the inclinations the wide binaries reach during their Kozai cycle, we find that a $\sin(i)$ times a Gaussian distribution (frequently used to describe the inclination distribution of heliocentric Kuiper Belt orbits, eg., Brown 2001) centered at $i = 0°$ with width $\sigma \simeq 22°$ is compellingly similar to the Kozai-modified distribution. We find that widths between $10° \leq \sigma \leq 50°$ are consistent with the observed (non-Kozai) distribution within the 95% confidence interval.

The difference in inclination distributions between both populations could either be due to cosmogonic variations inherent in different formation mechanisms, or due to evolutionary processes. Fabrycky & Tremaine (2007) showed that tidal friction coupled with Kozai oscillations can cause wide, high-inclination systems to shrink and become circularized, creating a paucity of widely-separated, high-inclination binaries, and an excess of tight binaries near the critical inclinations for Kozai cycles (40° and 140°). This is referred to as the Kozai Cycles with Tidal Friction (KCTF) mechanism, and its plausibility as a significant evolutionary mechanism for binary minor planets was confirmed by Ragozzine (2009) and Perets & Naoz (2009). While small numbers of objects and other complicating effects may prohibit the detection of an increase of tight binaries near the critical inclinations, the observed paucity of high-inclination, ultra-wide TNBs is suggestive of the KCTF effect in action.

We have performed a cursory test to compare the observed inclination distribution to the outcomes of KCTF. We determine the maximum eccentricity e_{max} each binary system can reach for a grid of initial inclinations i_0 and arguments of pericenter ω_0, assuming they begin with initial e_m and a_m equal to their present values. We then determine the fraction of phase space as a function of i_0 (assuming i_0 was initially uniformly distributed on a sphere) which do not lead to an e_{max} that causes each system's pericenter to drop below a critical number of primary radii — in other words, we require that $q_{min} \geq n \times R_p$. Ragozzine (2009) showed in full numerical simulations with reasonable assumptions that tidal dissipation became significant at $q \sim 20R_p$ for the binary system Orcus/Vanth, which is more massive than the binaries studied here. However, the binary system L5c02 has Kozai cycles which take it to $31^{+9}_{-7}R_p$, and presumably its existence suggests that such pericenter separations are stable for a significant fraction of the age of the solar system. As such, we chose the limit $q_{min} \geq 30 \times R_p$ for our cursory KCTF test, and compare the resulting "KCTF-modified" inclination distributions to the observed ultra-wide TNB inclination distribution (illustrated in Figure 2.12). We find that the resulting distribution (and any with smaller q_{min} cutoff) is ruled out at 97% confidence.

We conclude that while the KCTF mechanism may have modified the orbits of some very high-inclination ultra-wide TNBs, it alone is not enough to explain the current mutual inclination distribution of these systems. To verify this, more comprehensive studies of the effects of KCTF on systems like those presented here are needed. If KCTF is not sufficient to explain the mutual inclination distribution of the ultra-wide TNBs, then we must consider cosmogonic effects. The primordial poles of the wide binaries may have preferred orientations orthogonal to the Ecliptic plane, suggesting formation in a very cold disk (Noll et al. 2008b). It should be noted that if the inclination distribution of the ultra-wide TNBs is non-uniform, and the binaries are subjected to small perturbations over their lifetimes (e.g., collisions), then the mutual inclination distribution will always tend to become *more* uniform over time. As such, the primordial inclination distribution would have to have favored low inclinations even more strongly than the current distribution does. We explore the effects of collisions on the mutual inclination distribution in the following chapter.

2.6 Albedos and Densities

Given the dynamically-derived masses and visible photometry for each system, we can explore the albedos and densities for the component bodies in these binaries. Without radiometric measurements to ascertain the albedo independently, the density and albedo remain degenerate. However, by assuming physically plausible values for the component densities, we can estimate the implied albedos for each object; the results of this exercise are illustrated in Figure 2.13 and listed in Table 2.5. Generally, albedos for our sample of ultra-wide TNBs are found to be consistent with those measured radiometrically for larger solitary cold Classical Kuiper Belt objects (eg., Brucker et al. 2009), and range from 9%—30%, assuming $\rho = 1$ gram cm^{-3} (6.4%—21% assuming $\rho = 0.6$ gram cm^{-3}). Figure 2.13 also includes estimates of the albedos and radii of four other binaries from literature, and these systems were selected as

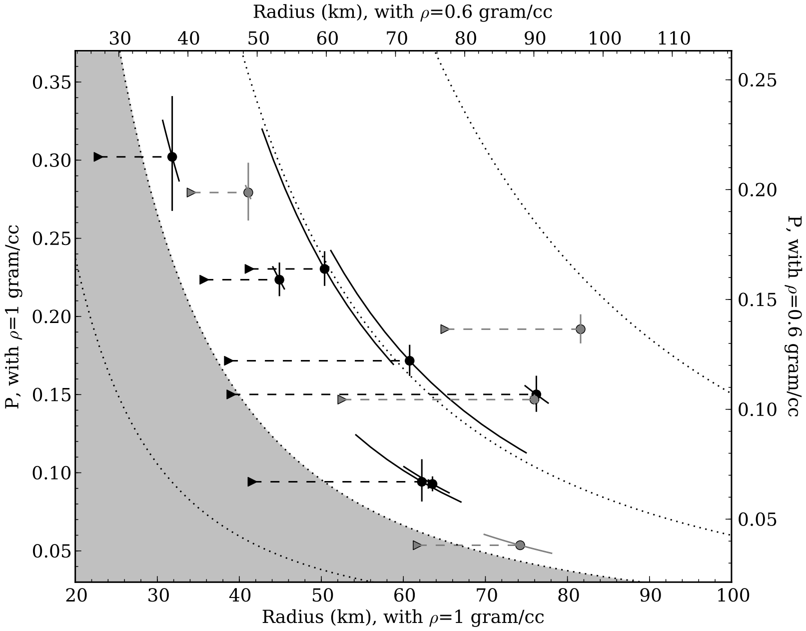

Figure 2.13: Albedos and radii for CC binary systems. Left/bottom axes show values assuming $\rho = 1$ gram cm^{-3}, while top/right axes show the values assuming $\rho = 0.6$ gram cm^{-3}. Circles mark primary radii, triangles connected with dashed line mark secondary radii. Black points represent binaries characterized here, gray points represent values derived from literature for the low-inclination classical TNBs 1998 WW$_{31}$, Borasisi/Pabu, Logos/Zoe and Teharonhiawako/Sawiskera. Dotted lines represent contours of constant H magnitude. Gray region marks $H_r > 8$, likely unpopulated due to flux limits of current binary searches.

Table 2.5: Albedos and Primary Radii (with $\rho = 1$ gram cm^{-3})

Name	P (r')	R_p (km)	Note
2000 CF$_{105}$	$0.30^{+0.04}_{-0.03}$	$31.8^{+0.6}_{-0.8}$	1
2001 QW$_{322}$	$0.093^{+0.010}_{-0.006}$	64^{+1}_{-2}	1
2003 UN$_{284}$	$0.09^{+0.03}_{-0.01}$	62^{+3}_{-5}	1
2005 EO$_{304}$	$0.15^{+0.01}_{-0.01}$	$76.2^{+1.0}_{-0.9}$	1
b7Qa4	$0.22^{+0.01}_{-0.01}$	$44.9^{+0.4}_{-0.5}$	1
hEaV	$0.17^{+0.07}_{-0.06}$	61^{+10}_{-6}	1
L5c02	$0.23^{+0.09}_{-0.06}$	50^{+6}_{-5}	1
1998 WW$_{31}$	$0.054^{+0.004}_{-0.004}$	74^{+3}_{-3}	1,3,7
Teharonhiawako	$0.147^{+0.003}_{-0.003}$	$76.0^{+0.3}_{-0.3}$	1,4,7
Borasisi	$0.192^{+0.009}_{-0.009}$	$81.6^{+0.2}_{-0.2}$	2,5,7
Logos	$0.28^{+0.02}_{-0.02}$	$41.1^{+0.2}_{-0.2}$	2,6,7

[1]: Adopting $m_\odot = -26.93$. [2]: Adopting $m_\odot = -27.12$. [3]: Photometry from Veillet et al. (2002). [4]: Photometry from Benecchi et al. (2009). [5]: Photometry from Delsanti et al. (2001). [6]: Photometry from Jewitt & Luu (2001). [7]: Mass from Grundy et al. (2011).

members of the CC sample which had estimates of their r-band magnitude. The albedos of these four literature systems range from 5.4%—28% (with $\rho = 1$ gram cm^{-3}).

The apparent trend of increasing albedo with decreasing radius visible in Figure 2.13 is due to a selection effect: in a flux-limited survey, any physically small object detected must have a high albedo. The apparent trend here is consistent with a flux limit somewhat less than $H_r \simeq 8$. We note that, in general, the observations which discovered the primary of a given binary system were not the observations which discovered the binary nature of the system. Thus, this flux limit seems to apply to the primary absolute magnitude, and the fact that secondary absolute magnitudes scatter across the $H_r = 8$ line reflects deeper follow-up observations identifying the secondaries.

The lack of a strong group of small, high-albedo binaries along with the lack of large, high-albedo binaries suggest that relatively low albedos may be more common than high albedos in the cold Classical Kuiper Belt. All seven binaries in Figure 2.13 with primary radius greater than 55 km have nominal albedos less than 20%, while all four binaries with primary radius smaller than 55 km have nominal albedos greater than 20%. Given the steepness of the size distribution of low-inclination TNOs in this size range ($q \sim 4.8$, Fraser & Kavelaars 2009), we would expect there to be roughly nine times as many objects in the radius range of 30—55 km than at all radii larger than 55 km. Since the sample contains only roughly 0.57 times as many binaries in the smaller size range, we posit that the rest of the expected small binaries are missing due to having low albedos, making them invisible to the flux limits of the surveys which discovered the binary systems in our sample.

We adopt an ansatz albedo distribution of a Gaussian centered at $p = 0.05$, and clipped such that $p > 0.05$ (comparable to the lowest measured albedo in our sample):

$$P(p) \propto \begin{cases} e^{-0.5(\frac{p-0.05}{\sigma_p})^2} & : p > 0.05 \\ 0 & : p \leq 0.05 \end{cases} \tag{2.6}$$

Additionally, we adopt a size distribution with slope $q = 4.8$, and estimate the flux limit at discovery to be $H_r = 8$. When we draw a radius from this size distribution, we assign it an albedo from our Gaussian albedo distribution and determine if it is bright enough to have been observed by our synthetic survey (brighter than $H_r = 8$). We then compare the properties of these synthetic "observed" systems with the systems which were actually observed by varying the width σ_p of the albedo distribution until the KS test can rule out that either the distribution of real radii or the distribution of real albedos are drawn from the synthetic "observed" distributions. We find that at 95% confidence, the observed range of real albedos implies that the albedo distribution must have a width $\sigma_p \gtrsim 0.058$ or there would be too few high albedo detections. Additionally, given the observed real primary radius distribution, the albedo distribution must have a width $\sigma_p \lesssim 0.1$ or there would be too many small objects discovered. Figure 2.14 illustrates the distribution of albedos and primary radii of the real binaries in comparison to the synthetic "observed" distributions of these parameters.

The lack of a strong group of small, high-albedo binaries may also be explained in the case of a more uniform albedo distribution by positing that the binary fraction decreases drastically for decreasing radii, similar to the prediction of Nesvorný et al. (2011). However, with the addition of a varying binary fraction with size as a new degree of freedom, the current sample size is not sufficient to quantitatively constrain such behavior at this time. We note that given the large range of albedos observed in this population, any sharp features in the trend of binary fraction with radius will be blurred if considering only the absolute magnitude of systems (as done in Nesvorný et al. 2011), and any such features will be much more evident when radii derived from mass measurements or radiometric measurements are used in place of absolute

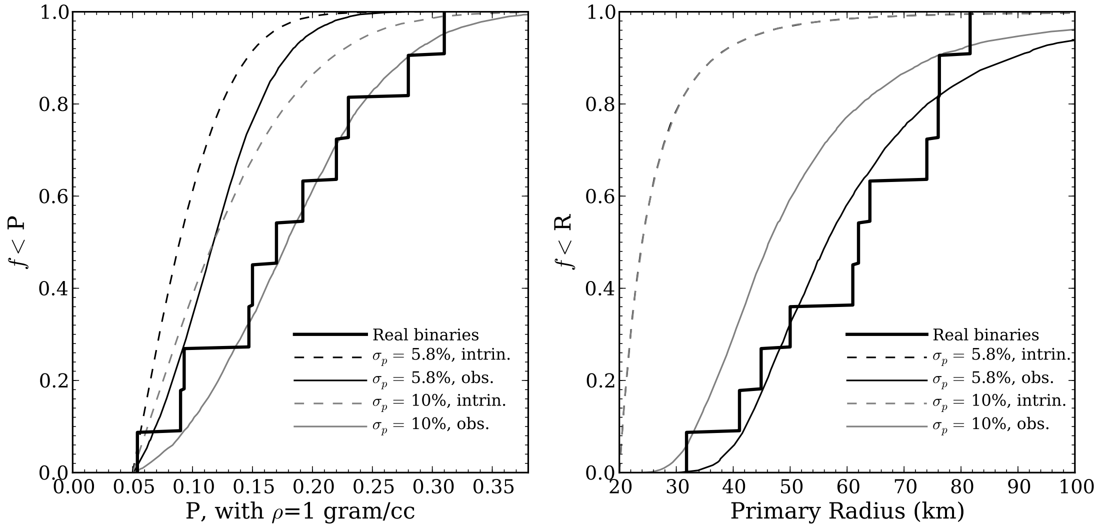

Figure 2.14: Left panel: comparison of binary albedo distribution (heavy histogram) with model distributions, assuming an albedo distribution with form of Eqn. 2.6, a power-law size distribution with slope $q = 4.8$, and binary discovery survey flux limit of $H_r = 8$. Intrinsic albedo distributions shown by dashed lines, while synthetic "observed" distributions shown by solid lines. Right panel: Same binaries and albedo distributions, but showing resulting radius distributions.

magnitudes.

2.7 Discussion

2.7.1 Formation Mechanisms and Implications

Since the discovery of the first TNBs, a number of possible formation pathways have been posited. In the following discussion, we consider those mechanisms most likely to form widely-separated, near-equal mass systems, and compare the predicted outcomes of each of these pathways to our observed sample.

L_2s and L_3 mechanisms

Originally described in Goldreich (2002), these mechanisms were further investigated by Noll et al. (2008b) and Schlichting & Sari (2008 a & b). The L_2s mechanism posits that binaries are captured when two passing solitary objects can disperse some excess kinetic energy into a sea of smaller bodies and become bound, while the L_3 mechanism instead sends the excess kinetic energy away through scattering a third large body.

Schlichting & Sari (2008b) show that models like L_2s, which rely on a smooth dissipation process to capture binaries, will dominate the binary formation rate only in conditions where the relative velocity between planetesimals v is much less than the Hill velocity, $v_H = 2\pi R_H/T_{\text{out}}$, where T_{out} is the heliocentric orbital period. They also show that under these conditions, the binary mutual inclinations will be dominantly retrograde, predicting a prograde-to-retrograde ratio $\lesssim 0.03$. The measured wide binary inclinations exclude such an extreme ratio of prograde to retrograde systems. Therefore, we can rule out this mechanism for forming wide binaries, unless an intervening dynamical process can be invoked to re-orient a large number of binary systems or preferentially destroy retrograde binary systems. We estimate that starting from a primordial prograde-to-retrograde ratio of 0.03, at least 22% of wide binary systems would have to be re-oriented in order to not be ruled out at greater than 95% confidence by the current observed prograde-to-retrograde ratio.

Under more energetic conditions, where the relative velocity between planetesimals exceeds v_H, Schlichting & Sari (2008b) show that three-body interactions (L_3 models) will dominate the binary formation rate. In this regime, they find that roughly equal numbers of prograde and retrograde systems are formed, consistent with the observed distribution of inclinations. However, they also show that only systems with separations of order $s \lesssim R_H(v_H/v)^2$ tend to survive the formation phase, and binary formation rates drop dramatically as v increases. As our observed binary systems have separations of order $0.08 - 0.22R_H$, the velocity dispersion in the primordial disk could not have exceeded 2—4 times v_H if this formation mechanism applied. Additionally, Noll et al. (2008b) suggest that formation in a dynamically cold disk ($v < v_H$) should produce aligned orbit poles. Since the wide binaries seem to prefer low mutual inclinations, this argues for formation in a dynamically cold disk, but not so cold as to allow L_2s to dominate and produce a large fraction of retrograde systems.

Together, the widely-separated components, lack of clear preference for retrograde orbits, but apparent preference for low mutual inclinations all point toward the velocity dispersion being approximately equal to the Hill velocity. This represents a fine-tuning problem (Noll et al. 2008b), for there is no clear *a priori* reason to expect that $v \sim v_H$. Additionally, it is not clear whether the balance between the L_3 and L_2s mechanisms at $v \sim v_H$ would simultaneously produce widely separated binaries, aligned poles, *and* roughly equal numbers of prograde and retrograde orbits.

Exchange Reactions and Chaos-Assisted Capture

Funato et al. (2004) suggest that multiple exchange reactions (where one object in a binary system is swapped for a passerby) can produce very widely separated binary systems. However, systems as widely separated as those in our sample formed through exchange reactions all have very high eccentricities ($e_m \gtrsim 0.9$, see Figure 2.7). The systems L5c02 and hEaV have present eccentricity values consistent with these predictions, but all other systems are presently inconsistent with such high eccentricities. Several systems are subject to large oscillations of their inclination and eccentricity due to Kozai cycles, but these oscillations do not carry them to eccentricities as high as predicted by exchange reactions. Thus, it seems unlikely that this mechanism dominated binary formation.

Astakhov et al. (2005) simulated the effect of chaotic transient binaries on stable binary formation. They found that two objects temporarily caught in their mutual chaotic layer could become stabilized by dynamical friction due to a sea of small objects — effectively adding an enhancement to the L_2s mechanism due to transient, chaotic orbits. This mechanism is referred to as Chaos-Assisted Capture. They find mutual eccentricities spanning the range of those observed in our sample, but the separations they find for binaries formed by Chaos-Assisted Capture do not extend to as high as those found for the ultra-wide TNBs (see Figure 2.7). Additionally, Schlichting & Sari (2008a) argue that the enhancement due to these transient captures is not significant, and that formation should proceed as they found for the L_2s and L_3 mechanisms. We conclude that it is unlikely that this mechanism dominated the ultra-wide TNB formation rate.

Gravitational collapse

Recently, another mechanism has been proposed to form Kuiper Belt binaries. Operating with the framework of planetesimal formation through rapid gravitational collapse in a turbulent disk, Nesvorný et al. (2010) suggest that binaries may form as a cloud of cm-scale particles collapses and fragments. This model produces binaries very efficiently, and their properties can vary widely. Mass ratios of order unity are produced, and semi-major axes from $10^3 - 10^5$ km are produced for systems with primary radii ranging from tens to hundreds of kilometers. Broad ranges of inclination and eccentricity can be produced for all semi-major axes. Additionally, this mechanism has the attractive feature of producing a natural explanation for the correlated colors of binary components (Bennechi et al. 2009), in contrast to the broad range of colors exhibited between different binary systems.

We compare the results of a subset of these simulations to our observed mutual orbits. We select only those simulations which produce binaries with final mass ratio < 10, and with initial particle-swarm rotation $\Omega = 0.5 - 1.0\Omega_{circ}$ (where $\Omega_{circ} = R^{-\frac{3}{2}}\sqrt{GM}$, and M and R are the total initial mass and radius of the swarm) and collisional cross-section enhancements (to account for the lower resolution of the simulation compared to reality) $f^* = 10 - 30$. See Nesvorný et al. (2010) for a more thorough description of these parameters and their importance. Figure 2.7 illustrates the mutual eccentricity and a/R_H for all the synthetic orbits formed by this mechanism which meets these criteria, and in general we find that they appear to mimic the distribution of real orbits surprisingly well. Figure 2.15 illustrates the distribution of a/R_H for the synthetic orbits compared to the CC binaries and all the other binaries. We find that the a/R_H distribution of the CC binaries is statistically indistinguishable from the synthetic orbit distribution generated by gravitational collapse, while we rule out that the other binary populations were drawn from the same distribution

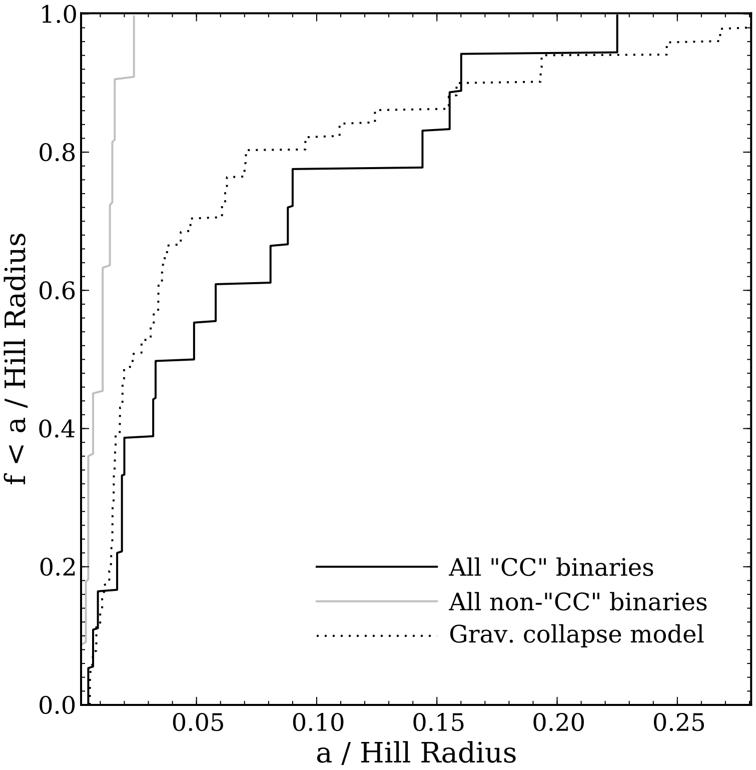

Figure 2.15: Cumulative histogram of a/R_H for CC TNBs (solid histogram) and all other TNBs with known orbits (grey histogram). Also shown are results of gravitational collapse binary formation simulations by Nesvorný et al. (2010), selecting simulations with $\Omega = 0.5 - 1.0\Omega_{circ}$ (initial clump rotation), $f^* = 10 - 30$ (cross-section modifier), and final mass ratio < 10.

as the synthetic orbits at a high level of confidence.

This agreement is encouraging, but it remains preliminary. The initial conditions for binary formation by gravitational collapse are still highly uncertain, and it remains unclear if this mechanism can produce a large number of retrograde binaries or if the binaries it produces will exhibit a preference for low mutual inclinations. Additionally, while the a/R_H distributions appear to agree, there are likely a number of biases in the current observed distribution and any conclusions drawn from it must be taken with caution. The binary fraction is measured to be $\sim 29\%$ in the cold Classical Kuiper Belt (Noll et al. 2008a), while the fraction of ultra-wide systems is approximately 1.5% (Lin et al. 2010); therefore, the ultra-wide binaries make up approximately 7% of the current CC binary population. However, comparing the systems with measured orbits, we see that the ultra-wide systems are over-represented, with our sample alone making up $\sim 39\%$ of all the CC binaries with measured mutual orbits. Taking this into account, it appears that the Nesvorný et al. (2010) model actually over-produces wide binaries compared to the present population.

There is additional concern since the current a/R_H distribution may not represent the primordial distribution; Petit & Mousis (2004) showed that these wide binary systems were likely much more common in the past, and may have been reduced in number due to collisional disruption. We discuss this problem in more detail in the following chapter.

2.7.2 Characterizing wide binaries with next-generation surveys

While the current sample of known ultra-wide TNBs remains fairly small, future wide-area surveys like the Large Synoptic Survey Telescope (LSST) and Pan-STARRS will be quite capable of identifying such systems. The projected LSST g-band single-visit depth is ~ 25, which translates to $H_g \simeq 8.5$ for a geocentric distance of 45 AU. At this depth, there are roughly 17,000 objects in CC-L7 component of the CFEPS synthetic model of the Kuiper Belt. At a minimum, the results of Lin et al. (2010) suggest that at least 1.5% of these objects are ultra-wide TNBs with characteristics like those in our sample, and we therefore expect over 250 such systems will be detectable by the LSST pipeline.

Some fraction of the observations of each of these TNBs will likely be resolved, depending on the binary separation and the seeing at the time of each observation.

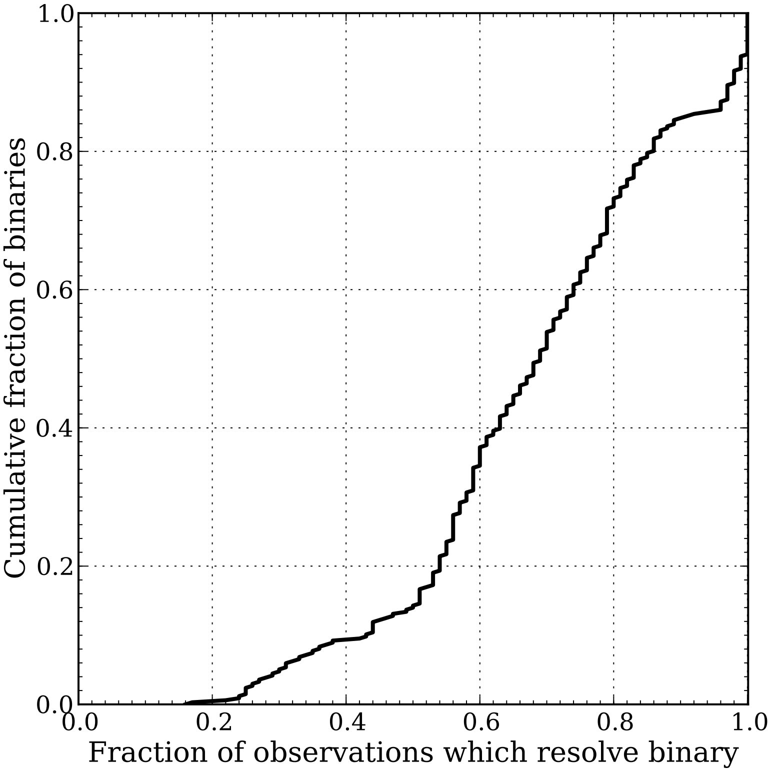

Figure 2.16: Results of observing clones of our sample of ultra-wide TNBs through simulated LSST seeing, assuming observations in the r-band taken over the course of the 10-year LSST survey lifetime. An observation is said to be "resolved" when the full-width at half-max of the seeing during that observations is smaller than the projected binary separation.

In order to estimate this fraction of resolved observations, we have used clones of each binary in our sample to determine the distribution of on-sky separations that can be expected over the ten-year baseline of the LSST survey. We move each clone to a random starting point on both its heliocentric orbit and mutual orbits, then propagated its motion forward for ten years while sampling its on-sky separation at 100 "observation epochs" over than ten-year period. At every "observation epoch" we determined if the system was resolved or not based on its on-sky separation and an image quality drawn from the measured r-band distribution of seeing at the LSST site (LSST Science Book Version 2.0, Section 2.2), with median seeing of $\sim$ 0".6. Figure 2.16 illustrates the cumulative fraction f_B of binary systems versus the minimum fraction of observations which resolve those systems.

The minimum fraction of resolved observations for any system we simulated was $\sim$18%, and the maximum was 100%. If we take the planned baseline number of 230 visits per field in the $r-$band to represent the number of observations likely to be made of each binary, then we would expect $\sim$40—230 resolved observations of each binary system. This indicates that virtually *all* 250 TNB systems with properties similar to those in our sample likely to be observed by the LSST will have more resolved observation epochs than the most-observed binary in our current data set (2001 QW$_{322}$, with 35 observed epochs). As such, not only will LSST *detect* most of these binary systems, but it will measure their mutual orbit properties at least as well as we have managed to do with the sample presented in this paper.

With such a large catalog of well-characterized binary orbits, all drawn from the same well-calibrated survey, unprecedented avenues of investigation will be opened. Identifying trends of binary properties with heliocentric orbit may provide further evidence for different origins and histories of the sub-components of the Kuiper Belt, and will provide new constraints on the dynamical history of the outer Solar System (Parker & Kavelaars 2010, Murray-Clay & Schlichting 2011), trends of binary fraction with component sizes will constrain the extent of collisional grinding in the early Kuiper Belt (Nesvorný et al. 2011), and color—albedo trends may be identified and used to constrain the surface composition of these objects.

2.8 Summary

We have presented the first-ever well-characterized mutual orbits for a sample of seven ultra-wide Trans-Neptunian Binaries. These orbits range over eccentricities from $0.2-0.9$, and have semi-major axis to Hill Radius (a/R_H) fractions ranging from $0.08-0.22$. We find that their properties are distinct from other binary populations, with the following highlights:

1. The outer orbits of all widely-separated binaries ($a/R_H > 0.02$) with near-equal mass components ($\Delta m < 1.7$, or $M_p/M_s < 10$) are distributed consistently with being drawn from the "stirred" and "kernel" components of the CFEPS L7 synthetic model of the Kuiper Belt, and inconsistent with being drawn from the low-inclination subset of the "hot" component. This confirms that only the dynamically cold components of the Classical Kuiper Belt are host to wide binaries.

2. Two ultra-wide TNBs have very high mutual eccentricities ($e_m \simeq 0.84$ and 0.9) consistent with the predictions of binary formation by exchange reactions (Funato et al. 2004), but the rest are inconsistent with the extreme eccentricities predicted by this mechanism.

3. Ultra-wide TNBs have roughly equal numbers of prograde and retrograde orbits, and the observed ratio is inconsistent with the predicted preference for retrograde orbits if the L_2s binary formation mechanism dominated unless over $\sim 22\%$ of wide binary systems have switched orientations over their lifetimes.

4. Ultra-wide TNBs have a statistically significantly different mutual inclination distribution compared to tighter binaries in literature, and their inclinations also cannot have been drawn from a uniform sphere ($P(i) \propto sin(i)$) due to a lack of detections of high-mutual inclination wide binaries. This paucity of wide binaries at high inclinations and preference for low inclinations cannot be explained by the KCTF mechanism alone, and suggests a primordial preference for low-inclination mutual orbits. This suggests formation in a very dynamically cold disk.

5. The wide separations of these systems indicate that if binary formation was dominated by the L_3 mechanism, the velocity dispersion in the primordial disk must have been less than a few times the Hill velocity. A low velocity dispersion supports the observed preference for low mutual inclinations. However, the velocity dispersion could not have been much below the Hill velocity or the L_2s mechanism would have dominated and the ultra-wide binaries should exhibit a

strong preference for retrograde orbits. Thus, under the assumption that these are the only two efficient formation pathways, it appears that $v \sim v_H$. Further modeling of these mechanisms is required to determine whether a balance can be struck between them where widely-separated binaries can be formed with aligned poles and roughly equal numbers of prograde and retrograde orientations.

6. Current simulations of the alternative formation mechanism of gravitational collapse and fragmentation (Nesvorný et al. 2010) create orbital distributions similar to the observed present-day distributions. These simulations tend to over-produce wide systems, which leaves some room for post-formation disruption of ultra-wide binaries. However, it remains unclear if this mechanism can produce a large number of retrograde systems.

7. Assuming realistic densities, the implied albedos for the ultra-wide TNBs range over $\sim 0.09 - 0.30$, consistent with estimates of the albedos of solitary Cold Classical objects (eg., Brucker et al. 2009). The distribution of observed albedos with primary radius for all dynamically-cold TNBs (seven from this work and four others from literature) suggests that albedos at the lower end of this scale are intrinsically more common in this population. A Gaussian albedo distribution, centered at $p = 0.05$ and clipped such that $p > 0.05$, is consistent with observations for widths $0.058 \leq \sigma_p \leq 0.1$. This estimate does not account for the possibility that binary fraction might vary substantially with primary radius as predicted by Nesvorný et al. (2011).

Chapter 3

Collisional Evolution of Mutual Orbits

The dynamically-cold component of the classical Kuiper Belt is host to a very high fraction of binary systems, and some of these systems have very wide separations. These ultra-wide Trans Neptunian Binaries (TNBs) have been shown to be extremely delicate, sensitive to collisional disruption (Petit & Mousis 2004, Nesvorný et al. 2011, Parker et al. 2011) and disruption by close encounters with Neptune (Parker & Kavelaars 2010).

Given the characterized sample of ultra-wide TNBs presented in the previous chapter, we seek to accurately determine the collisional lifetimes of these wide systems and their implications for the current state of the Kuiper Belt. To do this, we expand upon the analytical estimates of Petit & Mousis (2004) in §3.2, then describe numerical simulations we performed to more accurately account for the effects of mutual eccentricity, mass loss, and multiple impactors in §3.3. We find a simple empirical correction to the analytic predictions described in §3.2 which accurately reproduces the collisional lifetimes determined by our simulations.

Armed with these new estimates of collisional lifetimes under a variety of assumed impactor populations, in §3.4 we determine the properties of these impactor populations (representing the population of $\gtrsim 1$ km) that are allowed given conservative assumptions about the primordial fraction of ultra-wide TNBs in the classical Kuiper Belt. This impactor population is extremely difficult to constrain observationally; TNOs with $R \sim 1$ km are unlikely to ever be detected in reflected light (with magnitudes $\gtrsim 33$), and at present the only limits that exist on their numbers are based on searches for stellar occultations (Schlichting et al. 2009, Wang et al. 2009, Bickerton, Kavelaars & Welch 2008). Determining the behavior of the TNO size distribution at small sizes is critical for understanding the accretion and collisional history of the outer solar system.

In §3.5 we discuss the evolution of the properties of the binary mutual orbits over their lifetimes as they are subjected to collisions, and discuss the effects of these collisions on the interpretation of the current orbital distributions. In general we find that it is unlikely for the wide binaries to have evolved from initially tighter orbits, that their primordial mutual inclination distribution must have been even colder than it is currently, and that their current roughly equal numbers of prograde and retrograde orientations likely reflects the primordial distribution.

We conclude with a discussion of the implications of the existence of a single low-mass, widely separated system like 2000 CF_{105} and the importance of identifying the prevalence of systems like it in the current Kuiper Belt, implications of post-formation collisional evolution for our understanding of the binary formation mechanism(s), and also discuss the probability and utility of detecting transient brightening events caused by catastrophic collisions like those simulated in this work in future surveys like LSST.

3.1 Analytical Estimates of Collisional Lifetimes

Following Petit & Mousis (2004), the radius R_i of an impactor onto the secondary which can unbind (i.e., cause total system energy to exceed zero) a binary can be approximated by

$$R_i \simeq R_s \left(\frac{0.62}{V_i}\right)^{\frac{1}{3}} \left(\frac{GM_{sys}}{a_m}\right)^{\frac{1}{6}}, \tag{3.1}$$

where R_s is the radius of the system's secondary, V_i is the velocity of the impactor, M_{sys} is the total mass of both binary components, and a_m is the mutual semi-major axis of the binary. For the ultra-wide TNBs presented here, collisions at typical Kuiper Belt relative velocities of $V_i \sim 1$ km s^{-1}, Eqn. 3.1 estimates that the required impactor radii range from $\sim$1.6 km (for 2000 CF_{105}) to $\sim$5.7 km (for 2001 QW_{322}).

We can estimate the mean time between single impacts large enough to unbind the binary,

$$\bar{t} \simeq \left(P_i\, R_s^2\, N(R > R_i)\right)^{-1}, \tag{3.2}$$

where P_i is the intrinsic collision probability in km^{-2} yr^{-1} for objects in the Classical Kuiper Belt, and we nominally adopt the value of 1.3×10^{-21} (Farinella et al. 2000). This intrinsic collisional probability is determined by the orbital distribution of the population, and several estimates exist in literature which use different approaches (particle-in-a-box vs. analytical estimates) and assume different intrinsic orbital distributions. Later we explore the effects of adopting a different value for P_i. To simplify, we do not include the radius of the impacting objects in the estimate of the collisional cross-section, which results in an estimate of "head on" collisions instead of grazing collisions.

Given a power-law size distribution of the form $N(>R) = N_0(R/R_0)^{1-q}$, we find

$$\bar{t} \simeq \left(P_i\, R_s^2\, N_0 (R_i/R_0)^{1-q}\right)^{-1} = \left(P_i N_0 R_0^{q-1} R_s^{3-q} \left(\frac{0.62}{V_i}\right)^{\frac{1-q}{3}} \left(\frac{GM_{sys}}{a_m}\right)^{\frac{1-q}{6}}\right)^{-1} \tag{3.3}$$

Noting that collisions onto the primary of a binary system can also unbind the system, our analytic estimate of the mean system lifetime is half the harmonic mean of the average time between unbinding collisions for the primary and secondary components,

$$\tau_a \simeq \left(P_i N_0 R_0^{q-1} \left(R_s^{3-q} + R_p^{3-q}\right) \left(\frac{0.62}{V_i}\right)^{\frac{1-q}{3}} \left(\frac{GM_{sys}}{a_m}\right)^{\frac{1-q}{6}}\right)^{-1}. \tag{3.4}$$

For a system with nearly-equal mass components, adding this second decay channel reduces the mean lifetime by up to a factor of two.

3.1.1 Lifetime ratios: Separation and mass effects

In order to determine the relative importance of initial binary separation vs. binary mass with respect to survival time, we consider the lifetime estimate Eqn. 3.4 in the case where the binary has equal-massed components with equal bulk densities — thus, $R_p = R_s$ and $M_s = M_p = M_{sys}/2$. The ratio of lifetimes of two binaries immersed in the same collisional environment is:

$$\tau_1/\tau_2 = \left(\frac{R_{s2}}{R_{s1}}\right)^{3-q} \left(\frac{a_{m1} M_{sys2}}{a_{m2} M_{sys1}}\right)^{\frac{1-q}{6}} = \left(\frac{M_{sys1}}{M_{sys2}}\right)^{\frac{2}{9}(2q-5)} \left(\frac{a_{m1}/R_{H1}}{a_{m2}/R_{H2}}\right)^{\frac{1}{6}(1-q)}, \tag{3.5}$$

where subscripts indicate the properties of the first or second binary system being compared, and R_H is the is the Hill radius of a given system given by $R_H = a_{out}\left(\frac{M_{sys}}{3M_\odot}\right)^{\frac{1}{3}}$ where a_{out} is the Heliocentric semi-major axis of the binary system's barycenter. This ratio of lifetimes allows us to compare the importance of binding (a_m/R_H) to system mass in a given impactor regime. The indices on the two terms sum to zero when $q = 17/5 = 3.4$. At this slope, if system 1 has half the mass of system 2, then it will have to have half the a_m/R_H separation of system 2 in order to have the same lifetime. At steeper slopes, mass becomes the weakly dominant term, while for shallower slopes a_m/R_H has the largest effect on the lifetime.

For $q = 2.5$, τ_1/τ_2 is independent of the ratio of system mass, and for shallower slopes τ_1/τ_2 is actually inversely correlated with the ratio of system mass — an increased system mass leads to a *decreased* lifetime. This is a consequence of the impactor spectrum becoming very flat, resulting in the dominant mass effect in a system's lifetime becoming its cross section for collisions (which increases with system mass).

To illustrate, it is interesting to compare two systems with roughly similar values of a_m/R_H but significantly different masses. 2003 UN$_{284}$ and 2000 CF$_{105}$ are a good comparison; both are very widely separated, and the ratio of their best-fit a_m/R_H values is ~ 0.86. However, the ratio of their system masses is relatively high at ~ 6.8. Both have comparable mass ratios (~ 3). At a collisional equilibrium slope of $q = 3.5$ we would expect a ratio of lifetimes of approximately $\tau_{UN284}/\tau_{CF105} \sim 2.5$. For $q = 2.5$ we would expect them to have roughly equal lifetimes, while for an even shallower slope $q = 2$ (comparable to that currently measured for small objects, eg. Fraser & Kavelaars 2009) we would expect 2003 UN$_{284}$ to actually have a shorter lifetime than the much less massive and slightly more widely separated 2000 CF$_{105}$, with $\tau_{UN284}/\tau_{CF105} \sim 0.68$.

3.2 Numerical Simulations

The analytical estimates presented in the previous section do not account for a number of important effects, including mass loss, orbital evolution through multiple impacts, and the eccentricity of the orbit. To more accurately determine the collisional lifetimes of these binary systems, we performed a series collisional bath simulations for each system. We subject each binary to a series of impulses, corresponding to collisions with impactors drawn from a realistic size distribution, and monitor the stability of the binary after these encounters.

Our simulated impactor population was sampled from a size distribution characterized by a power law normalized at $N(R > 1\ \text{km})$. We chose this radius as it was close to the impactor size required to disrupt these binary systems according to our analytical estimates. This size distribution has a slope extending to larger and smaller sizes q_{small}, and at $R = 31$ km we break to a large-object slope similar to that measured in the Kuiper Belt, with $q_{\text{large}} = 4.8$ (eg., Fraser & Kavelaars 2009). We extrapolate the small-object slope down to a minimum impactor size of $R_{\text{min}} = 200$ m.

Given the total number of impactors considered, $N(R > R_{\text{min}})$, we then estimated the average time between collision events:

$$\bar{t} = \left(P_i\,\sigma\,N(R > R_{\text{min}})\right)^{-1},$$

where P_i is the intrinsic collision probability in km^{-2} yr^{-1} for objects in the Classical Kuiper Belt, and we nominally adopt the value of 1.3×10^{-21} (Farinella et al. 2000), while σ is the collisional cross section (without any π term). This cross section is adjusted to account for the radii of the impacting population in the following way: we inflate the radii of the binary components by a fixed buffer size of four times the primary radius, $\sigma = (5R_p)^2 + (R_s + 4R_p)^2$. At each iteration, we add $\bar{t}$ to the total elapsed time, then sample an impactor radius R_i from the impactor size distribution. We then determine if a near-collision occurs with the primary or the secondary, weighting the relative probability by the relative collision cross section of each component (including the extra buffer radius of four primary radii), and generate an impact parameter b drawn uniformly over the area of the component which was selected. If $b \leq R_0 + 0.9R_i$ (where R_0 is the radius of the binary component potentially suffering the collision without the added buffer radius) a collision is taken to actually occur. In general, radii and mass are related by assuming a bulk density $\rho = 1$ g cm^{-3} unless otherwise stated.

If a collision occurs, we then randomly generate the binary's mean anomaly M to determine the orbital phase of the binary system. The relative position $\vec{x}$ and velocity $\vec{v}$ of the binary components are estimated, and an impact trajectory is generated from a uniform sphere. All collisions are assumed to occur with relative velocity of $V_i = 1$ km s^{-1} unless otherwise stated.

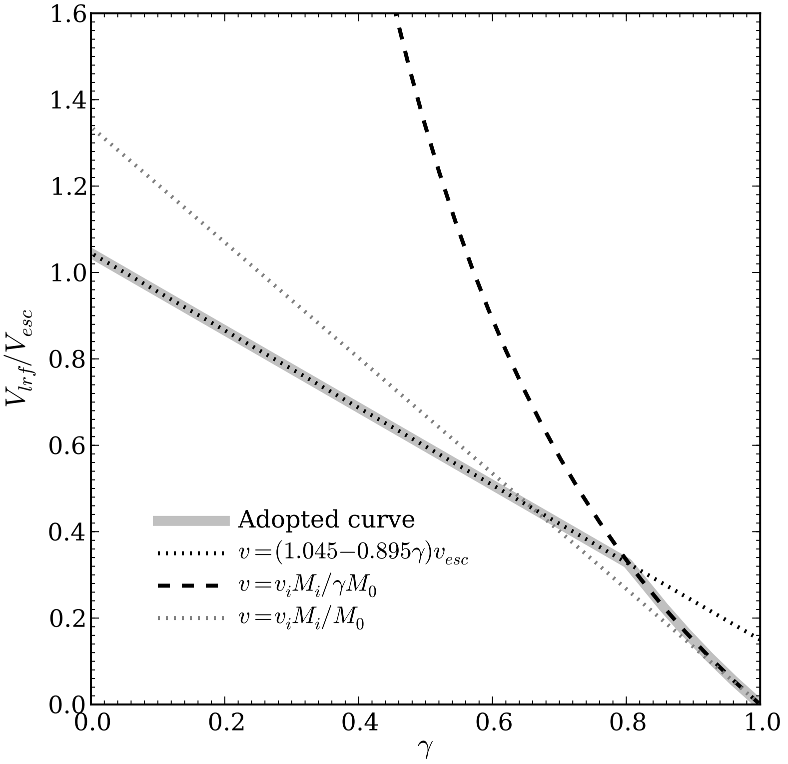

Figure 3.1: Ratio of velocity of largest remaining fragment V_{lrf} to parent body's escape velocity V_{esc} for a collision which results in a mass ratio of the largest remaining fragment to the parent body of $\gamma = M_{lrf}/M_0$. Curves illustrate different schemes for estimating V_{lrf}/V_{esc}; adopted curve should be compared to results of numerical simulations by Benz & Asphaug (1999, see Figures 15 & 16).

To improve the realism of these simulations, we also treat the mass-loss during collisions, using the strength laws found by Benz & Asphaug (1999) for ice in impacts at velocities on the order of 0.5—3 km s^{-1}. Based on the kinetic energy of the impactor KE_i, we estimate the mass of the largest remaining fragment given the relationship

$$\gamma \equiv \frac{M_{\mathrm{lrf}}}{M_0} = 1 - 0.5\left(\frac{KE_i}{M_0 Q_D^*}\right), \tag{3.6}$$

where M_0 is the mass of the parent body, and Q_D^* is the specific energy required to disrupt 50% of the mass of the parent body, given by

$$Q_D^* = 7 \times 10^7 \left(\frac{R_0}{1\ \mathrm{cm}}\right)^{-0.45} + 2.1\rho\left(\frac{R_0}{1\ \mathrm{cm}}\right)^{1.19} \mathrm{erg\ gram}^{-1}, \tag{3.7}$$

where ρ is the density of the parent body in gram cm^{-1}.

For "small" collisions ($\gamma \gtrsim 0.8$), we assume momentum is conserved with perfectly inelastic collisions (with all of the momentum of the impactor translated into the largest remaining fragment), ie. $\vec{v}_{b,1} = \vec{v}_{b,0} + \vec{v}_i \frac{M_i}{M_{lrf}}$, where subscripts b and i indicate binary components and impactor, respectively. We treated all velocity changes as velocity changes of the secondary with respect to the primary - therefore if a collision occurs on the primary,

$$\vec{v}_{\mathrm{secondary},1} = \vec{v}_{\mathrm{secondary},0} - \vec{v}_i \frac{M_i}{\gamma M_{\mathrm{primary}}}, \tag{3.8}$$

whereas if a collision occurs on the secondary,

$$\vec{v}_{\mathrm{secondary},1} = \vec{v}_{\mathrm{secondary},0} + \vec{v}_i \frac{M_i}{\gamma M_{\mathrm{secondary}}}. \tag{3.9}$$

In larger collisions where a significant amount of mass loss occurs, much of impactor's momentum is translated into small fragments, and the largest remaining fragment experiences a much smaller change in velocity. We use a simple piecewise-linear prescription with γ to approximately reproduce the velocity of the largest remaining fragment V_{lrf} found by Benz & Asphaug (1999), given by

$$V_{\mathrm{lrf}} = \min\left(V', (1.045 - 0.895\gamma)V_{\mathrm{esc}}\right), \tag{3.10}$$

where V' is the velocity that would be expected if all of the momentum of the impactor was translated into the largest remaining fragment, and V_{esc} is the escape velocity of the parent body. Figure 3.1 illustrates this velocity distribution and compares it to other schemes for treating momentum conservation for massive collisions.

After each collision, the cross-section of each component is re-computed given their new mass, and the average time between all future collisions $\bar{t}$ is re-calculated to reflect the change in collisional cross section. The total time assumed to have elapsed at this point is the sum of all the $\bar{t}$ values between all impacts preceding the latest impact.

Given a new velocity vector $\vec{v}_1$ post-impact, we transform coordinates to (a, e, i) space. If the system has become unbound, if the mutual apocenter has grown larger than the system's Hill radius R_H, or if the components have merged (mutual pericenter drops to less than the tidal Roche limit), integration is stopped. The radius of the final impactor that disrupted the system, the survival time τ (taken to be the elapsed time), and the total mass lost by each component over its lifetime is recorded.

Figure 3.2 illustrates the result of integrating 2000 realizations of two binary systems (2000 CF_{105} and 2001 QW_{322}), with $N(R > 1\ \mathrm{km})$ held fixed and q_{small} randomly selected at each realization from $2.0 < q_{\mathrm{small}} < 4.5$. For steeper size distribution slopes, smaller objects will often cause the final disruption of a system. These two systems were selected for illustration because the represent the extremes of r_c for all the systems characterized. All other systems are illustrated in Figures 3.3 & 3.4.

For most realizations, the total mass loss suffered by the system is less than 10% of its initial mass, confirming the result found by Petit & Mousis (2004) which found that for reasonable size distributions, shattering collisions are much less important for disrupting these binary systems compared to smaller perturbations. The average mass lost by the systems is illustrated in Figures 3.2—3.4 as well, and generally two trends can be seen; these trends are a result of the way the impactor size distribution is normalized. At low q_{small}, relatively large amounts of mass can be lost to single (large) impactors, but as q_{small} increases the number of large impactors decreases (since we hold $N(R > 1\ \mathrm{km})$ fixed) so the total amount of mass lost decreases with increasing q_{small}. However, for large q_{small}, the cumulative effect of many small impactors begins to matter, and as q_{small} increases the number of these small impactors increases, and more mass is lost at higher q_{small}.

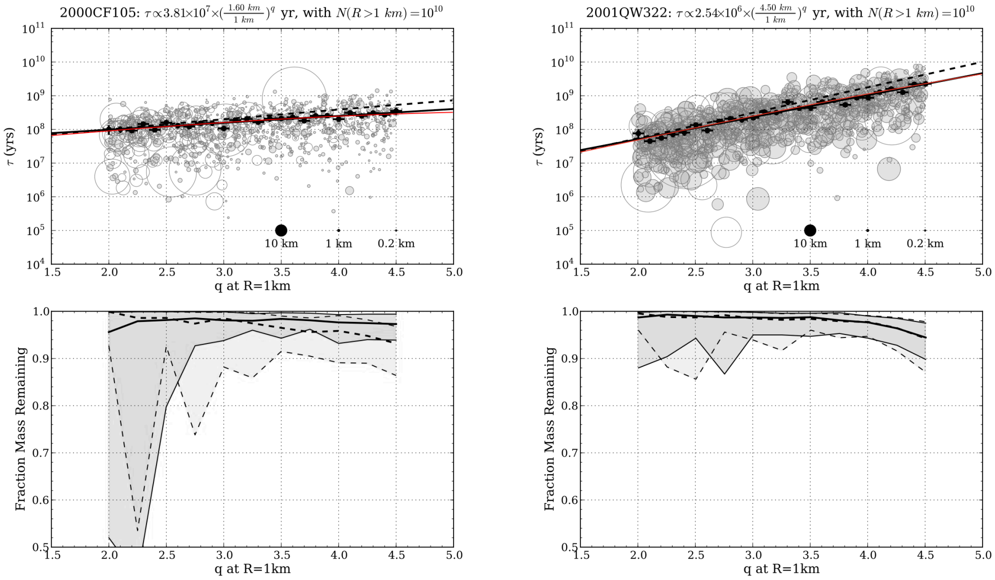

Figure 3.2: Results from 2000 collisional bath simulations for the binary systems 2000 CF_{105} (left panels) and 2001 QW_{322} (right panels), where $N(R > 1$ km) is held fixed at 1×10^{10} and differential size distribution power-law slope q is varied between 2.0 and 4.5. Top panels: Points represent time until system was disrupted in each case (only 1000 points shown for clarity), while radius of each point represents the radius of the impactor that caused disruption, and red line shows fit to mean system lifetime as a function of q. Open points illustrate a system where one or both components lost more than 50% of its mass by the end of the system lifetime. Bottom panels: average fraction of mass remaining in primary (heavy solid line) and secondary (heavy dashed line), and standard deviations for each (shaded regions). These two systems represent the extreme values of the critical impactor radius r_c whose space density determines system lifetime.

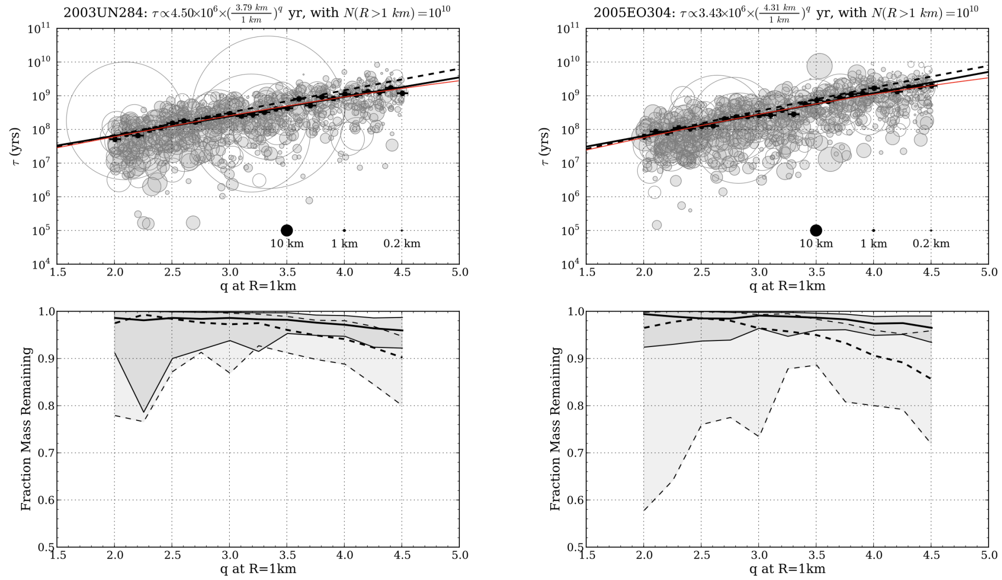

Figure 3.3: Same as Figure 3.2, but for 2003 UN_{284} and 2005 EO_{304}.

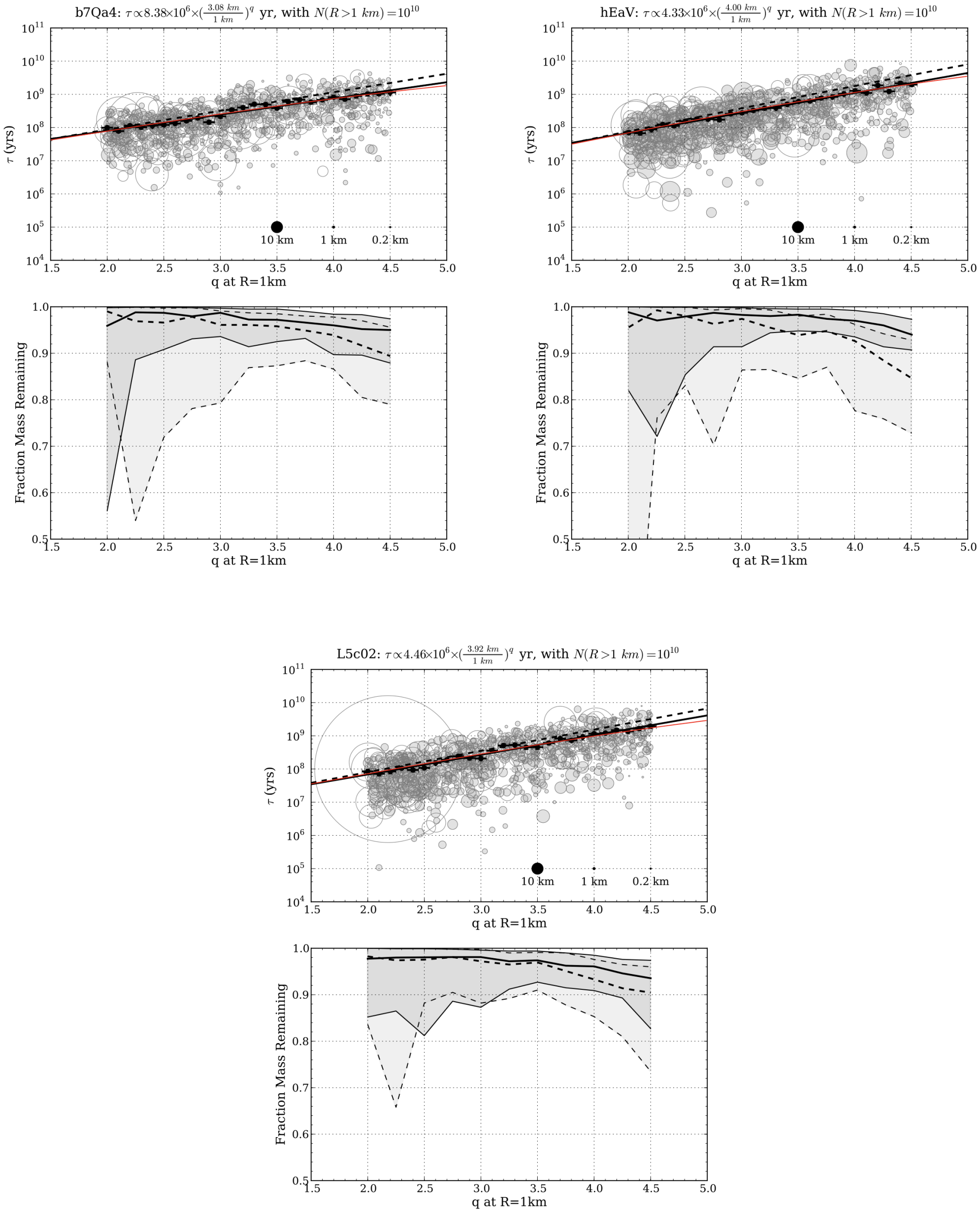

Figure 3.4: Same as Figure 3.2, but for b7Qa4, hEaV, and L5c02.

Table 3.1: Fit parameters for Eqn. 3.11 & adopted parameters for Eqn. 3.13

Name	K (yr)	r_c (km)	${r_i}^a$ (km)	M_{sys} (kg)	R_p^b (km)	R_s^b (km)	a_m (km)
2000 CF_{105}	3.81×10^7	1.60	1.65	1.85×10^{17}	32.0	23.0	3.33×10^4
2001 QW_{322}	2.54×10^6	4.50	5.74	21.1×10^{17}	63.5	63.5	1.015×10^5
2003 UN_{284}	4.50×10^6	3.79	3.83	12.4×10^{17}	62.2	41.6	5.55×10^4
2005 EO_{304}	3.43×10^6	4.31	3.74	20.7×10^{17}	76.2	39.1	6.98×10^4
b7Qa4	8.38×10^6	3.08	3.26	5.7×10^{17}	44.9	35.7	2.53×10^4
hEaV	4.33×10^6	4.00	3.83	12.1×10^{17}	60.8	38.7	3.23×10^4
L5c02	4.46×10^6	3.92	3.95	8.4×10^{17}	50.4	41.2	2.76×10^4

[a]: Required impactor radius for disruption by collision with secondary, from Eqn. 3.1.

[b]: Radii of components are estimated by adopting system mass and delta-magnitudes measured in Parker et al. (2011) and assuming a bulk density of 1 gram cm^{-3}.

3.2.1 Interpretation of simulation results

As a consequence of the way the impactor size distribution is normalized at the number with $R > 1$ km, the trend in system lifetime τ vs. q_{small} indicates the characteristic radius r_c of an impactor whose space density is the critical factor in determining the lifetime of a given binary. For a system with $r_c \sim 1$ km, the trend in the survival time vs. q_{small} should be approximately flat (as seen for 2000 CF$_{105}$, with $r_c = 1.6$ km), whereas if $r_c > 1$ km the mean survival time should increase with q_{small} (as seen for 2001 QW$_{322}$, with $r_c = 4.50$ km) as long as $N(r > 1\text{ km})$ is held fixed.

We fit the the mean lifetime $\bar{\tau}$ as a function of slope q given the collisional circumstances used in the simulation,

$$\bar{\tau}(q) = K \times \left(\frac{r_c \text{ km}}{1 \text{ km}}\right)^q . \tag{3.11}$$

The parameters K and r_c for each system are given in Table 3.1. Comparing the values of r_c to the values of r_i predicted by Eqn. 3.1, we see that they are generally very similar.

The binned mean lifetimes can also be well reproduced by applying a simple correction to the analytical lifetime estimates from the previous section. Given that the analytical lifetime estimate underestimates the effect of multiple small impactors (both in random walk of orbital elements and mass loss through many erosive collisions), we might expect this correction to go as some power-law with index $\sim q$. We find that the ratio between the analytic lifetime estimate τ_a and the numerical simulation estimate τ_{sim} is well reproduced for all binaries by the function

$$f = \tau_a/\tau_{sim} = 0.007 \times 3.12^q + 1 \tag{3.12}$$

Figure 3.5 illustrates τ_a/τ_{sim} for all seven ultra-wide TNBs characterized in this work, and shows Eqn. 3.12 for comparison. We stress that this correction has no rigorously physically-motivated form; other functional forms were explored, but in general did not improve the scatter significantly. No obvious trends in initial system separation, mass, or eccentricity were found when attempting to reduce the scatter in the correction results. We have also compared this correction to simulations with different impact velocity ($V_i = 0.5 - 2$ km s^{-1}), different bulk density ($\rho = 0.4 - 2$ g cm^{-3}), and simulations of much more tightly bound binaries ($a_m/R_H \simeq 0.01$) and

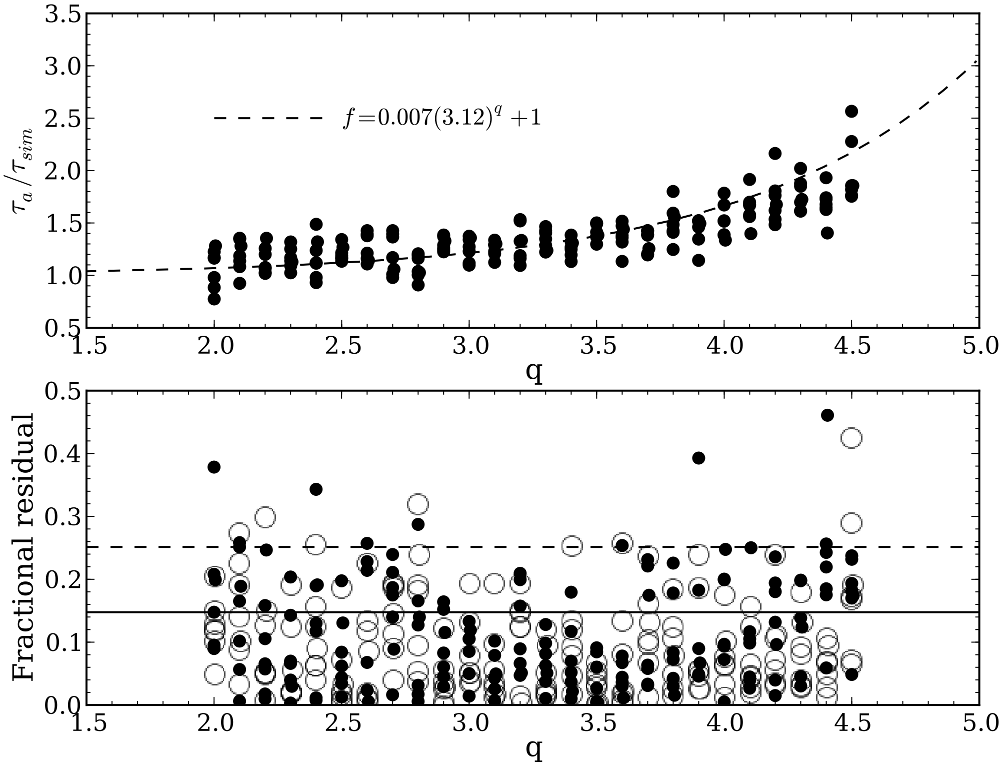

Figure 3.5: Top panel: Ratio of analytical estimate of system lifetime τ_a to binned results of collisional simulations τ_{sim}. Also illustrated is the correcting function f. Bottom panel: Fractional residuals between corrected lifetime and binned simulation results (filled points) and between power-law fit to simulation results and the binned simulation results (open points). Note that, in general, the corrected analytical estimates have a comparable or lower scatter than the power-law fit. 68% and 95% contours of fractional residuals between corrected lifetime and binned simulation results shown by solid and dashed line, respectively.

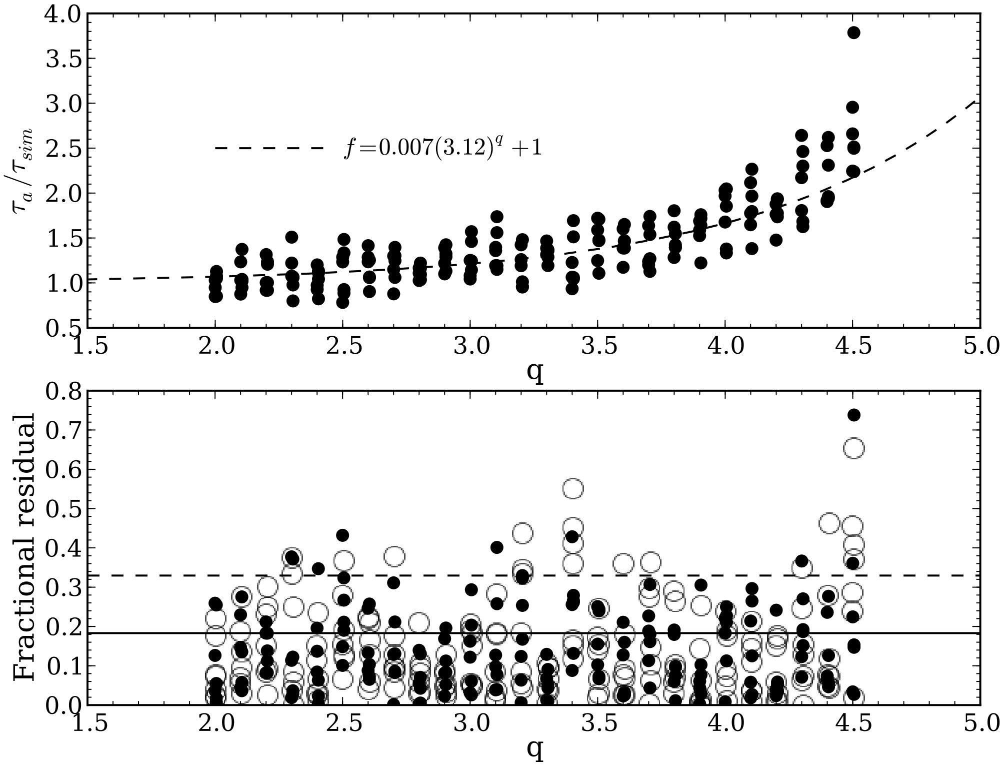

Figure 3.6: Same as Figure 3.5, but for simulations with $V_i = 2$ km s^{-1} and $\rho = 0.4$ g cm^{-3}. Note the somewhat poorer performance of the correction function f at extremely steep slopes due to increased mass loss; however, the single power-law fit to the system lifetime vs. q also performs poorly at these high slopes.

find that it generally holds in these regimes as well. The correction is found to break down at high size-distribution slopes ($q \gtrsim 4$) in cases of simultaneously high impact velocity (2 km s^{-1}), low density (0.4 g cm^{-3}), and tightly bound binaries ($a_m/R_H \simeq 0.01-0.02$) because the amount of mass-loss suffered before these systems become unbound tends to be rather large; as such, the true system lifetimes tend to be somewhat shorter than predicted by the analytical correction in these extreme cases. Figure 3.6 illustrates the same quantities as Figure 3.5 for the wide binaries in a set of simulations with $V_i = 2$ km s^{-1} and $\rho = 0.4$ g cm^{-3}; in general the same correcting function still performs better than the Eqn. 3.11 power-law fit to τ vs. q, though the correction performs less well in this case than in the $V_i = 1$ km s^{-1}, $\rho = 1$ g cm^{-3} case.

Combining Eqns. 3.4 and 3.12 allows for accurate estimate of nearly any TNB,

$$\tau_{corr}^{-1} \simeq (0.007 \times 3.12^q + 1) P_i N_0 R_0^{q-1} \left(R_s^{3-q} + R_p^{3-q}\right) \left(\frac{0.62}{V_i}\right)^{\frac{1-q}{3}} \left(\frac{GM_{sys}}{a_m}\right)^{\frac{1-q}{6}} . \quad (3.13)$$

For all further discussion, system lifetimes are estimated as $\tau = \tau_{corr}$.

3.2.2 Small object population limits

Given the current existence of a population of n objects today with individual mean lifetimes τ_i, the initial population implied by that population is

$$n_0 = \sum_{i=0}^{n} e^{\frac{t}{\tau_i}} \quad (3.14)$$

where t is the time over which the binary population has been decaying, estimated as 4×10^9 years. Given a maximum initial population of binaries, we can then numerically solve Eqn. 3.14 given τ_i determined by Eqn. 3.13 and the parameters in Table 3.1. The parameter we choose to vary in Eqn. 3.13 in order to solve Eqn. 3.14 is N_0 which we take to be $N(R > 1$ km) for a given power-law slope q. This results in an estimate of the maximum population of $R > 1$ km objects in the classical belt allowed by the continued existence of our sample of wide binaries, given size distribution slope q and an assumed initial population of binaries. This estimate also assumes that the impactor size distribution is in equilibrium, and is not evolving in time. Thus, we take these estimates to reflect the current collisional environment of the Kuiper Belt ignoring any early collisional evolution of the size distribution.

Given a current binary fraction f and a primordial binary fraction f_0, the number of primordial binaries n_0 implied by a given number of extant binaries n is

$$n_0 = n\frac{f_0}{f}, \tag{3.15}$$

As our most conservative estimate, we assume that ∼100% of the current Cold Classical objects started their lives as binaries. At present ∼ 30% exist as tight binaries (Noll et al. 2008a), so we set the primordial wide-binary fraction to be at most 70%. The extant fraction of wide binaries is estimated to be much lower, at approximately 1.5% (Lin et al. 2010). To be conservative, we assume that after disruption of a binary system, only one of its members remains as a Cold Classical object. Using this primordial binary fraction, the n_0 implied by our sample of seven wide binaries is

$$n_0 = 7\frac{0.7}{0.015} = 327 \text{ (Case 1).} \tag{3.16}$$

However, such a high fraction of wide-binaries is not physically motivated by any formation model. To set a more realistic upper limit of the impactor population, we consider the results of the binary formation simulations presented by Nesvorný et al. (2010). These simulations modeled the formation of binaries through gravitational collapse, and in the previous chapter we found that while somewhat over-producing wide binaries compared to the extant sample, the orbital distribution produced was favorably similar to the observed distribution. The relative fraction of wide binaries (splitting at $a_m/R_H = 0.07$) produced by these simulations is approximately 20% of all binaries formed. Therefore, even if the total binary fraction of the primordial Cold Classical Kuiper Belt was 100%, the primordial wide binary fraction likely did not exceed 20% given this formation scenario. Using this primordial binary fraction, the n_0 implied by our sample of seven wide binaries is

$$n_0 = 7\frac{0.2}{0.015} = 93 \text{ (Case 2).} \tag{3.17}$$

We set n_0 in Eqn. 3.14 first equal to 327 (case 1), then to 93 (case 2) and solve for $N(R > 1 \text{ km})$ as a function of q given the collisional lifetimes from Eqn. 3.13, assuming two values of P_i; 1.3×10^{-21} km^{-2} yr^{-1} suggested by Farinella et al. (2000) for collisions between Classical Kuiper Belt objects, and 4×10^{-22} km^{-2} yr^{-1} as derived by Dell'Oro et al. (2001) for the same circumstances but assuming a different orbital distribution and using a different derivation technique. The results are illustrated in Figure 3.7; under any of the size distribution slopes we consider, the population of 1 km radius objects in the Classical Kuiper Belt must be less than $\sim 2 \times 10^{10}$ objects (assuming the smaller P_i value) or less than 5×10^9 objects (assuming the larger P_i value), with fewer objects being allowed for lower q.

For comparison, we extrapolate the measured large-object population to $R \simeq 1$ km. The CFEPS L7 synthetic model of the Kuiper Belt[1] contains $\sim 45,500$ objects with $H_g < 8.5$ in the Main Classical Kuiper Belt (hot, stirred, and kernel components). Extrapolating this population to a break magnitude of $H_g = 10$ with a luminosity function slope of $\alpha = 0.76$ (eg., Fraser & Kavelaars 2009) we find $\sim 618,000$ in this population larger than the break magnitude (translated with $p = 0.1$ to a radius of 26 km). We then extrapolate this number to $R = 1$ km using a size distribution with slope q normalized at $R = 26$ km,

$$N(R > 1\ \mathrm{km}) = 618,000 \times \left(\frac{1\ \mathrm{km}}{26\ \mathrm{km}}\right)^{1-q}. \tag{3.18}$$

Current observations suggest that the Cold Classical Kuiper Belt size distribution breaks at radii of 20-30 km to a slope of approximately $q \simeq 2$ (Bernstein et al. 2004, Fraser & Kavelaars 2009, Fuentes et al. 2009). If this slope continues all the way down to radii of 1 km, the implied population of impactors would allow the survival of a relic wide binary population over the age of the Solar System. However, such a slope would be inconsistent with the putative detection of a single stellar occultation event by a ~ 250 m TNO reported by Schlichting et al. (2009). The convergence of the $R > 1$ km population estimates at slopes of $q \sim 3.5$ from extrapolating the large-object population, collisional lifetimes of binaries, and stellar occultations, combined with the fact that a the total mass of a population with size distribution slope steeper than $q = 4$ is infinite, suggests that the small-object size distribution slope lies between $3.2 \leq q < 3.8$, and $N(R > 1$ km$)$ is a few billion. Using the less conservative $P_i = 1.3 \times 10^{-21} km^{-1} s^{-1}$, the maximum viable slope becomes $q \lesssim 3.6$ for case 1 and $q \lesssim 3.5$ for case 2.

At the steep-slope end, the current existence of the binary 2000 CF$_{105}$ sets the strongest upper limit on the impactor population, as its low mass and wide separation make it extremely easy to disrupt by the numerous small impactors in this

---

[1] Available at `http://www.cfeps.net/L7Release.html`

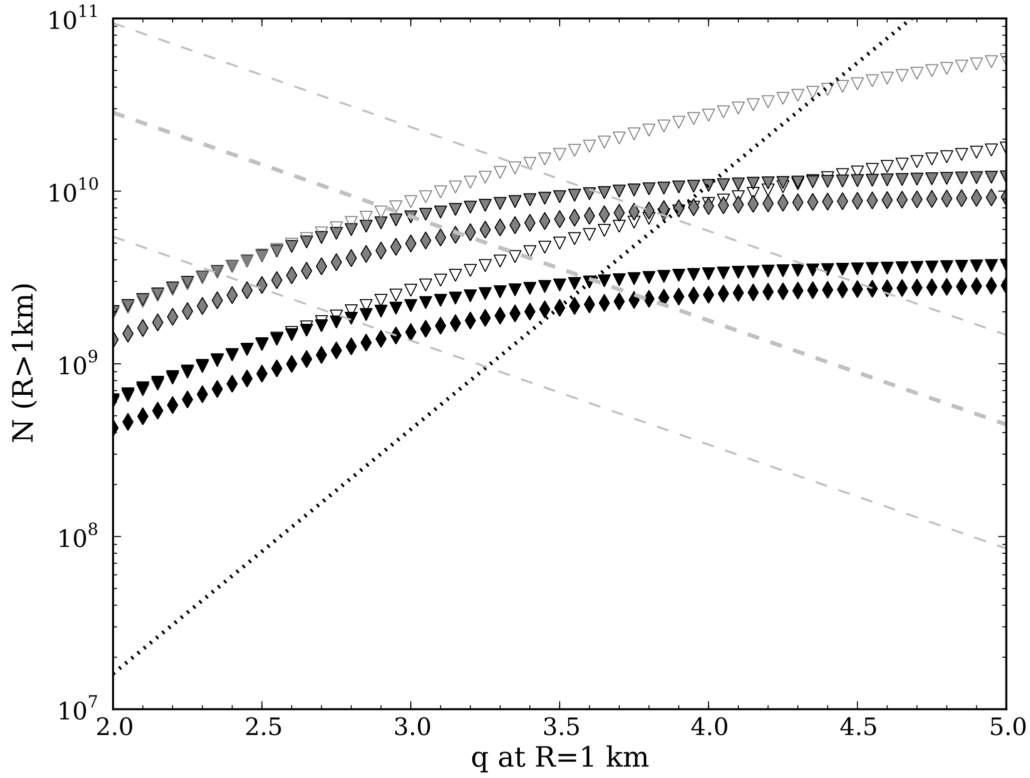

Figure 3.7: Upper limits on number of objects larger than 1 km that pass through the Classical Kuiper Belt, assuming wide binaries today represent an eroded primordial population. Results assuming $P_i = 1.3 \times 10^{-21}$ km^{-2} yr^{-1} (black points) and $P_i = 4 \times 10^{-22}$ km^{-2} yr^{-1} (gray points). Triangles show upper limit for case 1 (70% primordial wide-binary fraction), while diamond points show upper limit for case 2 (20% primordial wide-binary fraction). Open triangles show limit when 2000 CF$_{105}$ is removed for case 2. Dotted line shows extrapolated population assuming albedo of $p = 0.1$, determined as described in the text with Eqn. 3.18. Dashed silver lines shows best-fit (heavy line) and 1-σ limits (light lines) extrapolated from the estimate of the $R \gtrsim 250$ m population by occultations (Schlichting et al. 2009).

regime. Figure 3.7 includes the upper limit on the impactor population with 2000 CF_{105} removed, and while at low q there is no change, at high q the upper limit becomes much less constraining. Small binaries like 2000 CF_{105} are at present the least complete sample, as they suffer the strongest flux bias — only those with very high albedos are detected in current surveys, and 2000 CF_{105} likely represents the first of a large population. Determining the prevalence of small 2000 CF_{105}-like binaries in the current Kuiper Belt should therefore be a critical goal of future large-scale surveys.

Note that these estimates remain fairly conservative; even in case 2 (primordial wide-binary fraction of 20%) we assume that the total primordial binary fraction was 100% and no intense period of collisional grinding occurred. Such an epoch would be extremely destructive to the primordial binary population (Petit & Mousis 2004, Nesvorný et al. 2011). Additionally, we assumed in each case that when a binary was disrupted, only one of its two components survived on as a solitary TNO; in reality, a large fraction of both the disrupted primaries and secondaries would survive as independent TNOs in this population. If we assume both components survive, n_0 derived from Eqn. 3.15 becomes

$$n_0 = n\frac{1+f^{-1}}{1+f_0^{-1}}, \tag{3.19}$$

which produces $n_0 = 195$ for case 1 and $n_0 = 79$ for case 2.

Also clear from Figure 3.7 is that these estimates are quite sensitive to the adopted value of the intrinsic collisional probability. In fact, the upper limit on the small-object population is inversely proportional to the adopted value, as $\tau \propto (P_i N(R > 1\text{ km}))^{-1}$, and therefore for a fixed lifetime, $N(R > 1\text{ km}) \propto P_i^{-1}$. Our uncertainties on the upper limits on the small-object population are driven largely by the uncertainty in P_i for today's Kuiper Belt; the difference between the two values adopted in this work imparts a factor of 3.25 variation between the their respective estimates of the small-object population. Fortunately, when newer and more accurate values are available the population estimates we present can be revised by simply scaling them by the ratio of our adopted values of P_i to the newer value.

3.2.3 Does orientation play a role in survival time?

The asymmetry in the maximum stable tidal radius between prograde and retrograde orbits allows wider orbits to exist stably for retrograde orbits, but we have found that this additional stable phase space does not significantly enhance the lifetime of retrograde binaries subjected to collisions drawn from realistic impactor size distributions.

By determining the change in velocity required to lift an initial orbit to an arbitrary final semi-major axis, and using this Δv to determine the impactor size required to affect this change (under the assumption of a perfectly inelastic collision with the binary's secondary), the ratio of the population of impactors capable of lifting a given binary to beyond its prograde tidal limit to the population capable of lifting the same binary to beyond its retrograde tidal limit is approximately

$$\frac{N(>R_p)}{N(>R_r)} \simeq \left(\frac{1 - a_0/R_H}{1 - 2a_0/R_H}\right)^{(q-1)/6}, \tag{3.20}$$

where a_0 is the initial semi-major axis, and assuming that the stable tidal limit for retrograde orbits is one classical Hill radius R_H, while the stable limit for prograde orbits is one-half of the classical Hill radius. Since the lifetime of the binaries is inversely proportional to the population of impactors that are capable of disrupting them, this ratio represents the ratio of lifetimes of retrograde and prograde binaries. Comparing this relationship to the known wide binaries ($a_0/R_H \sim 0.08$—0.25), we see that even with extremely steep impactor size distributions this ratio is close to unity, and thus would expect very little asymmetry between the expected mean lifetimes of the prograde and retrograde binaries.

To verify that survival time is generally independent of inclination, we performed a test of the effect of the tidal stability asymmetry by re-running our numerical simulations and approximating the tidal stability limits as

$$R'_H = \begin{cases} 0.5R_H & \text{if } i_m \leq 90^\circ; \\ R_H & \text{if } i_m > 90^\circ. \end{cases}$$

We selected the initial inclination for each binary system from a uniform distribution between $0^\circ < i_0 < 180^\circ$, and determined whether each binary's mutual apocenter remains below our approximation of the stable limit for its current inclination after every collision. The resulting mean lifetimes (for values of q ranging from 2—4.5) showed no discernible variation with initial system inclination.

The lack of strong variation indicates that if the primordial populations of prograde and retrograde populations were equal, that equality should persist to the present day. If there was any primordial asymmetry, however, evolution of the mutual inclination may cause some systems' orientations to flip, thereby causing the prograde-to-retrograde ratio to change over time. We explore this possibility in the following section.

3.3 Evolution of orbital parameters

3.3.1 Evolution of the inclination distribution

In our collisional simulations, we track the initial mutual inclination and the final inclination the system reaches before being disrupted. A significant unknown in the current understanding of how to interpret the orbital distribution of TNBs is how inclination evolves over time, as binary systems are subjected to various perturbations; in the case of collisional perturbations, we can determine the effect directly. In the following experiments, we considered impactor populations with a fixed size distribution slope of $q = 3$. We adopt this slope because it is still allowed by the arguments of the previous section when considering extrapolation of the $R \sim 1$ km population from the measured population of large objects, and because steeper slopes allow more chance of stochastic evolution of orbital evolution through multiple small impacts.

Figure 3.8 shows the difference between the initial and final mutual inclinations for 100 realizations of each binary system, where the initial inclinations were drawn from a uniform distribution ($p(i) \propto \sin(i)$) and impactors either struck uniformly from all directions or were drawn from a longitudinally-uniform disk with half-width of 20°. Final inclination was determined to be the last inclination of the system prior to the final impact that disrupted it. Many systems have little to no change in inclination before disruption; however, significant change did occur for some systems, and ∼15%—18% of the systems had their orientation flipped from prograde to retrograde or vice-versa, with the disk-like geometry more efficient at reversing orientations. The final inclination distribution was found to be indistinguishable from the initial, uniform distribution in both cases; in general, random perturbations will tend to make a non-uniform distribution *more* uniform, and not vice-versa.

The inclination distribution of TNBs has been shown to be indicative of formation mechanics (eg., Schlichting & Sari 2008), and it has been measured by recent surveys. As shown in the previous chapter, the wide binary inclination distribution is currently inconsistent with being drawn from a uniform distribution. It lacks any high inclination systems ($55^\circ \lesssim i_m \lesssim 125^\circ$), and has a large number of systems at very low mutual inclination. This preference for pole-aligned mutual orbits is sug-

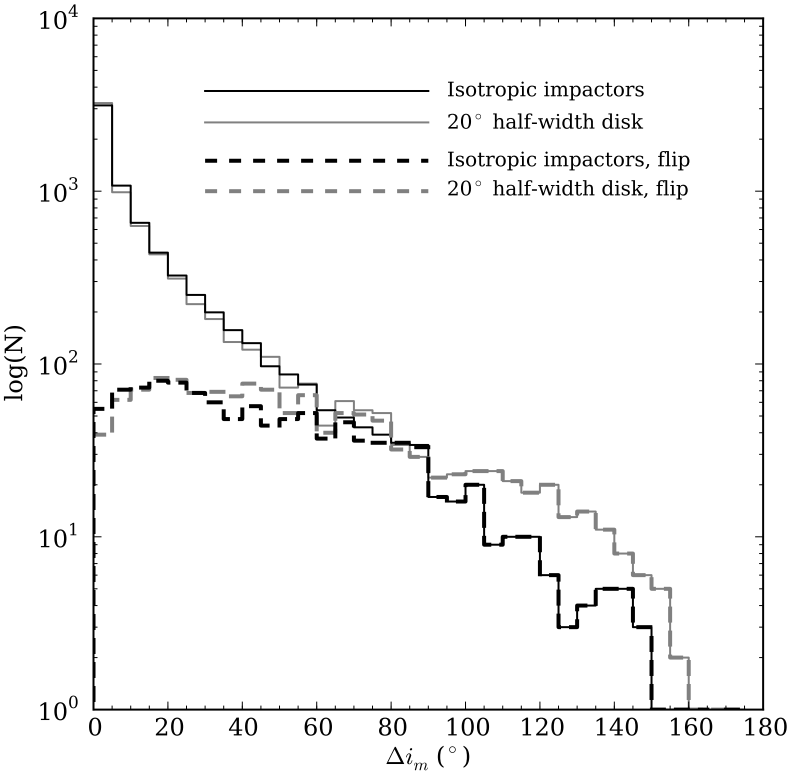

Figure 3.8: Histogram of the change in inclination before disruption of binary systems. Initial inclinations were drawn from a uniform distribution, and impactors either struck from random orientations or within a disk of half-width 20°. Dashed histograms illustrate the just those system's which had their orientation reversed from prograde to retrograde (or vice versa). 15—18% of systems are reoriented, with disk-like impactor geometry more efficient.

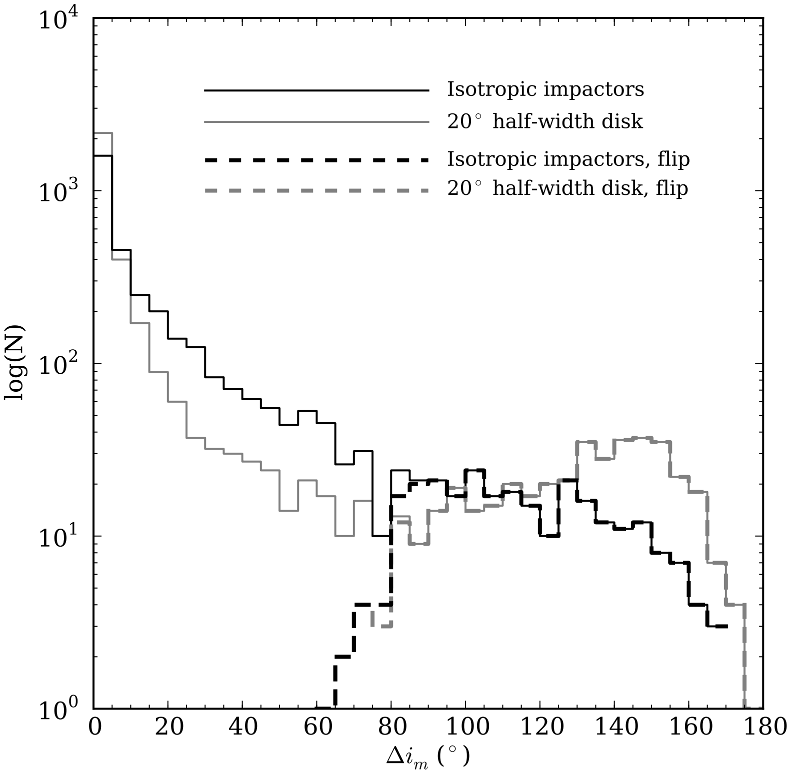

Figure 3.9: Same as Figure 3.8, but with initial inclinations drawn from $p(i) \propto \sin(i)e^{-\frac{1}{2}\left(\frac{i}{10^\circ}\right)^2}$. Fewer systems are reoriented, at between 7-11%.

gestive of formation in a dynamically cold disk (eg., Noll et al. 2008b). In order to determine the evolution of a primordially cold inclination distribution, we repeated our collisional simulations with an initial inclination distribution given by a sine times a Gaussian, centered at $i = 0°$ with a width of $\sigma = 10°$,

$$p(i) \propto \sin(i) e^{-\frac{1}{2}(\frac{i}{10°})^2}, \tag{3.21}$$

and determined the final inclination distribution given impactors striking uniformly from all directions or drawn from a longitudinally-uniform disk with half-width of 20°. The results are illustrated in Figure 3.9. Both final inclination distributions are strikingly similar to the present inclination distribution of the wide binaries. In the case of randomly-oriented impact trajectories, more inclination evolution occurred regardless of initial mutual inclination; however, in the case of disk-like geometry for the impactors, systems with low initial inclination tended to suffer less inclination evolution than the rarer systems with higher initial mutual inclination. A smaller fraction of systems changed orientation than in the case of uniform initial inclinations, due to the average system having to suffer significantly larger excursions in inclination in order to change orientation. Randomly-oriented impacts caused roughly 7% of systems to reorient, while impact trajectories drawn from a disk-like distribution caused roughly 11% to reorient.

We also investigated the possibility that with a disk-like impactor population, binaries which suffer collisions which widen their orbits will preferentially have their mutual inclinations decreased; this can be understood by thinking of "stretching" an initially inclined orbit in the plane of the impacts. We took synthetic binaries with initial $a_m/R_H \sim 0.02$ and subjected them to collisions with the same impactor populations as our wide binary experiments, but only with impact trajectories drawn from the disk-like distribution. We drew their initial inclinations from a uniform distribution, then considered the final inclinations of only those systems which had become widened (prior to disruption) to $a_m/R_H \gtrsim 0.07$, comparable to the minimum separation of the wide binaries considered here. Since these tighter systems take longer to disrupt than the wide systems, they were actually given a longer time over which to have their inclination modified than the wide binaries in our simulations. Figure 3.11 illustrates that while the inclination distribution does evolve away from the uniform distribution (unlike the behavior that would be expected from randomly-oriented impact trajectories), the inclination distribution does not change significantly

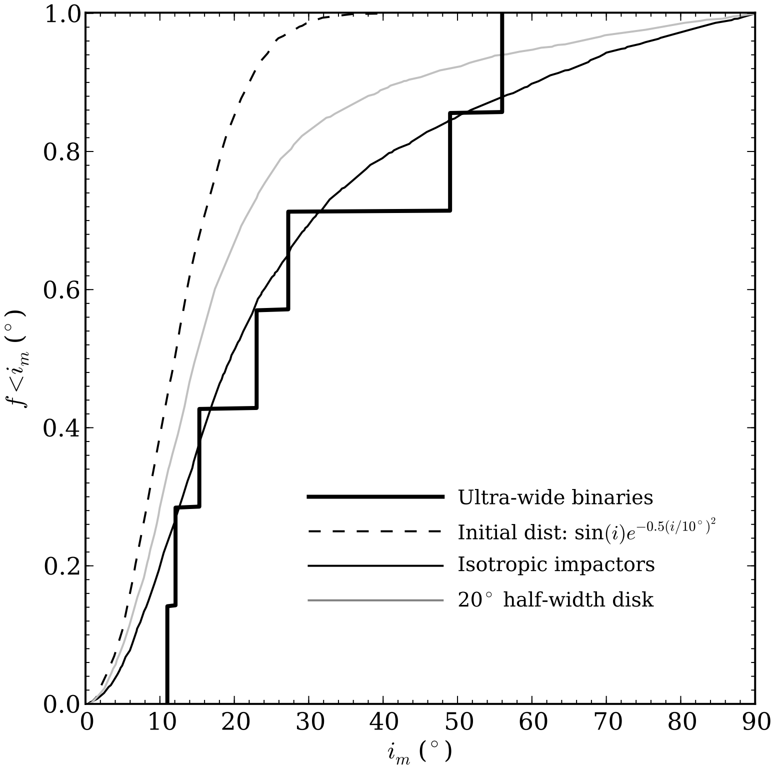

Figure 3.10: Comparison of initial and final inclination distributions after collisional evolution (final inclination taken just prior to binary disruption). Initial inclinations drawn from $p(i) \propto \sin(i)e^{-\frac{1}{2}\left(\frac{i}{10^\circ}\right)^2}$ (dashed line). Final inclinations shown for random impact trajectories (light black line) and disk-like impactor geometry (light gray line), and current ultra-wide TNB inclinations shown for comparison (heavy black line).

enough to make this mechanism feasible for explaining the current inclinations of the wide binaries. The KS statistic rules out that the wide binary inclination distribution was drawn from this collisionally-modified uniform distribution at greater than 95% confidence.

We conclude that if the wide binaries represent a highly collisionally-evolved population, then they must have had a much colder primordial inclination distribution. Additionally, they cannot have evolved from tighter binaries, because the current inclination distribution of tighter systems are close to uniform (Grundy et al. 2011, Parker et al. 2011) and collisions cannot produce a widened population with as cold an inclination distribution as is observed for the wide binaries when starting with an initially uniform inclination distribution.

3.3.2 Evolution of separation and eccentricity

In addition to tracking the inclination of the wide binaries during our collisional simulations, we also track their semi-major axis and eccentricity. Figure 3.12 illustrates the distribution of a_m/R_H and e just prior to collisional disruption for each binary system simulated, again with size-distribution fixed with $q = 3$. Since collisions preferentially occur while the system is at mutual apocenter, orbital evolution prefers to occur along the line of constant apocenter: $e' = (a_0/a')(1 + e_0) - 1$. The most severe increase in semi-major axis that can occur in a single non-unbinding collision is the condition where the original apocenter becomes the system's new pericenter: $e' = 1 - (a_0/a')(1 + e_0)$. Evolution to wider separation requires at least two significant collisions, and we find that it is uncommon for a system to be subjected to two such collisions while remaining bound. Between $90 - 95\%$ of all final orbits have final pericenters lower than their initial apocenter, and the most common behavior is to have next-to-no significant evolution prior to the collision which disrupts the system.

This conservation rule of $q' \leq Q_0$ can be used to further argue against the possibility that the current wide binaries represent a collisionally-widened tail of the tight binary population. If this were the case, not only would we expect a randomized inclination distribution, but we would also expect relatively high eccentricities to be the rule among the wide binaries. For an initially circular binary with initial $a_0/R_H = 0.02$, this conservation rule would state that if the system was widened to $a'/R_H = 0.1$ its eccentricity would usually exceed $e' \gtrsim 0.8$. As only two of the seven binaries in our sample exceed this eccentricity, it is unlikely that the wide binaries

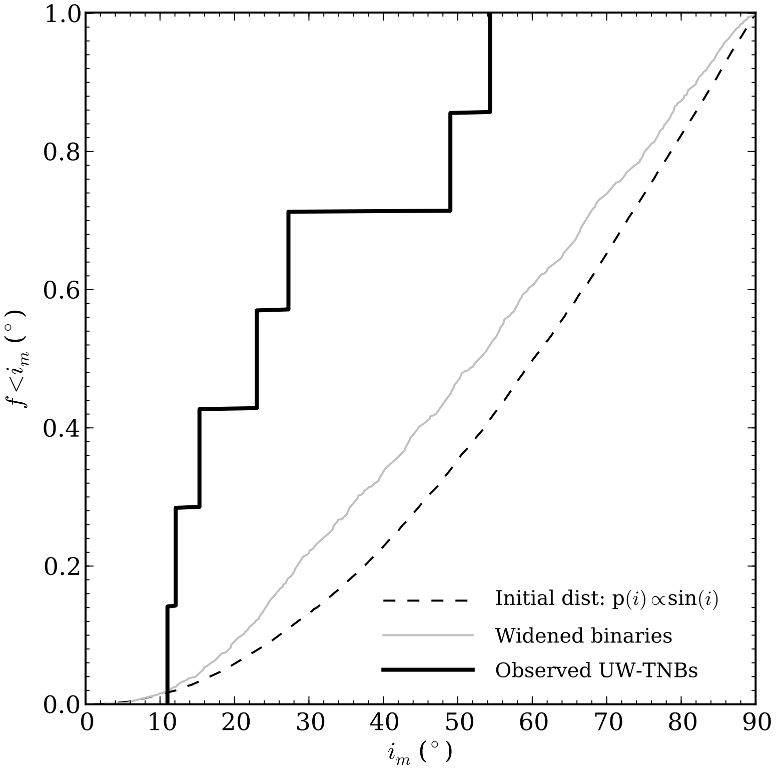

Figure 3.11: Comparison of initial and final inclination distributions after collisional evolution (final inclination taken just prior to binary disruption). Initial binary taken to have $a_m/R_H = 0.02$, and only those systems which are widened to $a_m/R_H > 0.07$ before disruption are considered. Initial inclinations drawn from $p(i) \propto \sin(i)$ (dashed line), and final inclinations of widened systems are shown for disk-like impactor geometry (gray line). Distribution of final inclinations for random impact trajectories are identical to initial distribution. Current ultra-wide TNB inclinations shown for comparison (heavy black line); that their inclinations are drawn from distribution of widened binary sample is ruled out at > 95% confidence.

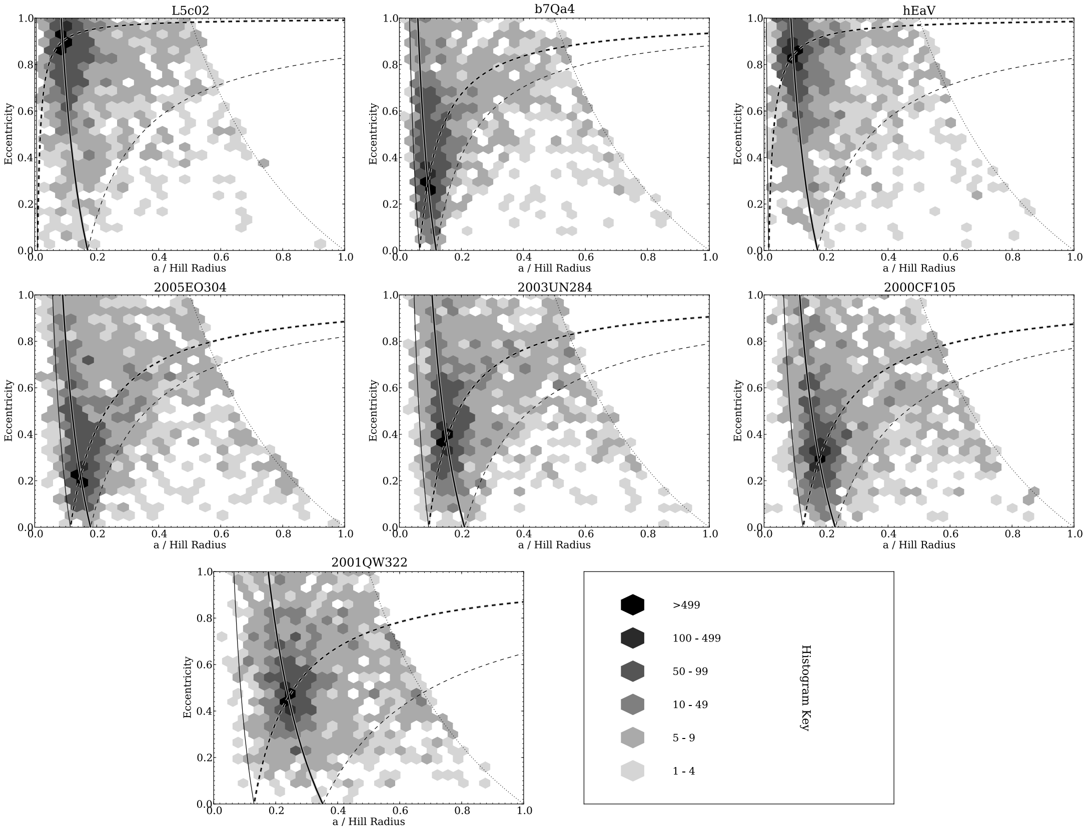

Figure 3.12: 2D histogram of last orbit before collisional disruption for each ultra-wide binary characterized, sorted in order of increasing initial a_m/R_H. These panels show outcomes for simulations with $q = 3$. Heavy solid line is constant apocenter ($e' = (a_0/a')(1+e_0)-1$). Heavy dashed line is constant pericenter ($e' = 1-(a_0/a')(1-e_0)$). These lines cross at the systems' current a_m/R_H and e. Light dashed line is where initial apocenter is final pericenter ($e' = 1-(a_0/a')(1+e_0)$), and light solid line is where initial pericenter is final apocenter ($e' = (a_0/a')(1-e_0)-1$). These lines mark the region within which a single non-unbinding collision can drive a binary. Note that binaries prefer to evolve along line of constant apocenter. Dotted line marks apocenter larger than the Hill radius, our criteria for disruption.

are the outcomes of this kind of evolution.

In fact, due to the larger available phase-space at high eccentricity, evolution along constant apocenter tends to increase the system's eccentricity for systems with low to moderate initial eccentricity while *decreasing* separation. Thus, systems like L5c02 with extremely high mutual eccentricities may represent the outcomes of collisional modification of initially wider and less eccentric systems. This is an attractive prospect, as the mutual pericenter passages of L5c02 during the high-eccentricity phases of its Kozai cycles ($q \simeq 31R_P$) may be close enough to cause significant orbital shrinking and circularization over the age of the solar system; if instead its present eccentricity is the outcome of a relatively recent collision, then it need not have maintained such close pericenter passages over such a long period.

3.4 Discussion

3.4.1 The curious case of 2000 CF_{105}

As discussed in §3.2, the binary 2000 CF_{105} is the most susceptible to collisional disruption under steep size distributions ($q > 2.5$), due to its wide separation and very small component sizes. Its current existence places the largest constraint on the population of impactors for these high slopes, but since at present it is only one binary the level of confidence one should have in this constraint is not immediately clear. For example, there is a non-zero probability that it represents a system which was primordially tightly-bound which has been anomalously widened, and it has not somehow survived over the age of the solar system in its current configuration.

However, a number of aspects of 2000 CF_{105} lead us to conclude that it is unlikely that it was ever tightly bound. First is its small size; it fell within the flux limits of current surveys only because of its extremely high albedo ($p \simeq 0.3$). Earlier we argued that somewhat lower albedos appear to be more common in the Kuiper Belt, and if this is the case then there is likely a large population of low-albedo 2000 CF_{105}-like binaries lurking unseen beneath the flux limits of current surveys. In other words, because of our current relative insensitivity to binaries of its size, the detection of 2000 CF_{105} suggests that binaries of similar size are intrinsically common.

Additionally, if 2000 CF_{105} were a collisionally-evolved tight binary, we would expect it to have both a high eccentricity and a mutual inclination drawn from the same uniform distribution as is observed for the tighter binaries (Parker et al. 2011, Grundy et al. 2011). However, its eccentricity is one of the lowest in our sample at $e = 0.29$, and it has the second-most aligned mutual orbit pole of any TNB known with a mutual inclination of 167.9°. Randomly drawing such an inclination from a uniform distribution is extremely unlikely ($p(|i_m| < 13°) \simeq 0.026$).

Together, the fact that 2000 CF$_{105}$ is likely the harbinger of many more small-radius binaries and that its current mutual orbit appears inconsistent with being generated by widening a tightly-bound binary through collisions, we conclude that the assumption that it has existed as an ultra-wide TNB in a configuration relatively similar to its present state over the age of the solar system is merited. By extension, we have confidence that its continued existence is a valid constraint on the small-object TNO population for steep size distributions.

3.4.2 Trends in binary fraction with radius: rapid collisional grinding vs. slow erosion

Nesvorný et al. (2011) showed that during a period of intense collisional grinding (motivated by the need to remove the excess mass required by hierarchical accretion models of planetesimal formation), a trend of decreasing binary fraction with decreasing radius would be imprinted on the surviving population in the radius range of the binaries considered here. Such behavior can be easily understood by considering the ratio of lifetimes expressed in Eqn. 3.5 and noting that for any impactor size distribution with slope steeper than $q = 2.5$ system lifetime decreases with decreasing system mass.

We can estimate the implied trend in binary fraction analytically. Given Eqn. 3.5, the binary fraction with radius will be the following exponential:

$$f(R) = 2^{-\left(\frac{R_{50}}{R}\right)^{(4q-10)/3}}, \tag{3.22}$$

where R_{50} is the radius of a binary whose population will be reduced by 50% due to collisional grinding after the elapsed time considered, given by solving Eqn. 3.13 for R given $\tau = t/\ln(2)$ with t being the elapsed time. To easily compare with the results of Nesvorný et al. (2011), we convert Eqn. 3.13 into terms of R_{50} and a_m/R_H (assuming a binary with equal-mass components on a circular orbit about the Sun) and solve:

$$R_{50} = \left[\frac{2t(0.007 \times 3.12^q + 1) P_i N_0 R_0^{q-1}}{\ln(2)} \left(\frac{0.62}{V_i} \right)^{\frac{1-q}{3}} \left(\frac{a_m}{R_H} \frac{a_{\mathrm{out}}}{G(\frac{(8\pi\rho)^2}{3} M_\odot)^{\frac{1}{3}}} \right)^{\frac{q-1}{6}} \right]^{\frac{3}{4q-10}} \tag{3.23}$$

This simple analysis ignores breaks in the size distribution, but these can be included trivially by treating Eqn. 3.22 in a piecewise manner:

$$f(R) = \begin{cases} f_1(R) = 2^{-\left(\frac{R_{50}}{R}\right)^{(4q_1-10)/3}} & : R > R_c \\ f_2(R) = (f_1(R_c))^{\left(\frac{R_c}{R}\right)^{(4q_2-10)/3}} & : R \leq R_c \end{cases}, \tag{3.24}$$

where R_c is the primary radius of a binary who can be disrupted by impact with an object with radius R_b which is the location of the break in the impactor size distribution between slopes q_1 (large object slope) and q_2 (small object slope). R_c can be derived from Eqn. 3.1, and here we convert it to terms of a_m/R_H:

$$R_c = \left(R_b \left(\frac{V_i}{0.62} \right)^{\frac{1}{3}} \left(\frac{a_m}{R_H} \frac{a_{\mathrm{out}}}{G(\frac{(8\pi\rho)^2}{3} M_\odot)^{\frac{1}{3}}} \right)^{\frac{1}{6}} \right)^{\frac{3}{4}}, \tag{3.25}$$

which, for a binary at 45 AU, with $V_i = 1$ km s^{-1} and $\rho = 1$ gram cm^{-2}, reduces to approximately

$$R_c \simeq 20.8 \times \left(\frac{R_b}{1\ \mathrm{km}} \right)^{\frac{3}{4}} (a_m/R_H)^{\frac{1}{8}} . \tag{3.26}$$

As an illustrative example, we consider the expected binary fraction with radius given an impactor population with $N(R > 1$ km$) = 5 \times 10^9$ and $q = 3.5$ after 4×10^9 years have elapsed. We adopt $P_i = 4 \times 10^{-22}$ yr^{-1} km^{-2}. Given these parameters and considering a binary with $a_m/R_H = 0.1$, we find $R_{50} \simeq 72.3$ km — that is, over the age of the solar system, this impactor population would destroy 50% of binaries with primary radius 72.3 km and initial $a_m/R_H = 0.1$. The resulting predicted binary fraction trend with radius is illustrated in Figure 3.13.

Also illustrated in Figure 3.13 are the trends if there is a break arbitrarily added to the impactor size distribution at $R_b = 2$ km. As a limiting example, the trivial case where there are no impactors with radius less than 2 km is shown, as well as a break to a shallower size distribution with $q_2 = 2.5$ or $q_2 = 2.0$ below the break. With the break radius at $R_b = 2$ km, the primary radius where we would expect the binary fraction trend to change is $R_c = 26.2$ km. For the case of $q_2 = 2.5$, the binary fraction remains fixed for all radii smaller than R_c, while for the other cases the binary fraction climbs again for smaller radii.

Note that the resulting trends in radius, while not as strong, are very similar to the trends predicted by the numerical simulations presented in Nesvorný et al. (2011) when considering a short period of intense collisional grinding. Though no strong evidence currently exists for a trend in binary fraction with radius, if such a trend is identified in the future further work will be required to disentangle its origin from one of two possibilities. Either such a trend could be produced through a period of strong collisional grinding in the early solar system, or it could be the result of slow collisional erosion over the age of the solar system (given a roughly steady-state impactor population with size distribution slope steeper than $q = 2.5$). This complication lies atop the underlying issue that at present there is currently little theoretical constraint on what trends of binary fraction with radius might be produced by the binary formation mechanism directly, without any subsequent modification by collisional erosion.

3.4.3 Implications for formation mechanisms

In the previous chapter, the wide binary inclination distribution was found to be inconsistent with a uniform distribution due to its preference for inclinations aligned with outer orbit poles. Such an inclination distribution was found to be suggestive of formation in a dynamically-cold disk. However, because the orientations of the wide binaries were found to be consistent with no preference for prograde or retrograde, and they ruled out an extreme preference for retrograde orientations predicted by Schlichting & Sari (2008b) for formation by the L_2s mechanism in a very cold disk, it was concluded that at the time of binary formation the velocity dispersion of the disk must have been approximately the Hill velocity.

In this chapter, we have shown that if the wide binary inclination distribution is in fact non-uniform, it must have been *less* uniform in the past with stronger preference for low inclinations. However, we have also found that if subjected to a maximally-erosive disk over the age of the solar system, a non-negligible fraction $(7 - 11\%)$ of these systems could be reoriented from prograde to retrograde and vice-versa. If the primordial prograde-to-retrograde ratio was ~ 0.03 as predicted by Schlichting & Sari (2008b) for formation in a very dynamically-cold disk, then

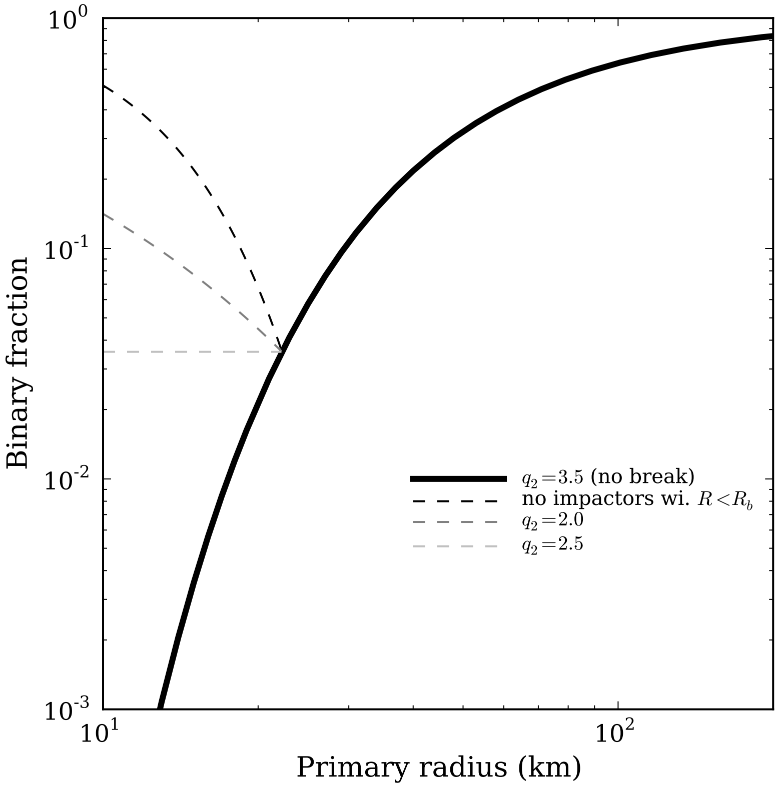

Figure 3.13: Analytical estimate of the trend of binary fraction with primary radius, given an impactor population with size-distribution slope $q_1 = 3.5$ valid for objects larger than $R_b = 2$ km, while the slope for smaller objects is allowed to vary. This initial impactor size distribution (which has no break) adopts the following parameters: $N(R > 1\text{ km}) = 5 \times 10^9$, $V_i = 1$ km s^{-1}, $P_i = 4 \times 10^{-22}$ yr^{-1}, and assumes that the binaries all have separations $a_m/R_H = 0.1$ and are equal-mass systems. Elapsed time is taken to be 4×10^9 years over which collisions have occurred. Heavy solid line shows trend with no break to shallower slope, while dashed lines show several cases with $q \leq 2.5$ where binary fraction will increase with decreasing radius.

reorienting 10% of the binaries over the age of the solar system would result in a current prograde to retrograde ratio of ~ 0.14. Even after this reorientation, however, the probability of randomly sampling 4 prograde and 3 retrograde systems from a distribution with a prograde-to-retrograde ratio of 0.14 is less than 1%. Thus it seems that collisions cannot be invoked to reorient a sufficient number of binaries to make the L_2s mechanism a viable explanation for the majority of wide binary orbits.

In the previous chapter, we also explored the possibility that these wide binaries formed through the gravitational collapse mechanism posited by Nesvorný et al. (2010), and found generally encouraging results. However, it was found that when correcting for observational completeness, the Nesvorný et al. (2010) results somewhat over-produce wide binary systems (roughly by a factor of four) with respect to the currently observed separations. Given collisional decay of both populations, we can estimate how the ratio of wide to tight binaries would evolve over the age of the solar system:

$$\frac{N'_{wide}}{N'_{tight}} = e^{t\left(\frac{1}{\tau_{tight}}-\frac{1}{\tau_{wide}}\right)}\frac{N_{wide,0}}{N_{tight,0}} = \left(\frac{f_{tight,0}}{f'_{tight}}\right)^{1-\frac{\tau_{tight}}{\tau_{wide}}}\frac{N_{wide,0}}{N_{tight,0}}, \tag{3.27}$$

where $N_{x,0}$ represents the primordial number of a given population x, while N'_x represents the current number of that same population x after collisional decay, and f'_{tight} and $f_{tight,0}$ represent the current and primordial fraction of tight binaries. Using Eqn. 3.5 to estimate $\frac{\tau_{tight}}{\tau_{wide}}$ for binaries with the same mass but a ratio of $(a_{tight}/R_H)/(a_{wide}/R_H) = 0.02/0.1 = 0.2$ for a size-distribution slope of $q = 3$ gives a ratio of lifetimes of roughly 1.7. Comparing an even more tightly bound binary to a more widely separated one, $(a_{tight}/R_H)/(a_{wide}/R_H) = 0.01/0.2 = 0.05$, we find an even larger lifetime ratio of ~ 2.7.

Substituting $\frac{\tau_{tight}}{\tau_{wide}} = 1.7$ into Eqn. 3.27 along with a primordial tight binary fraction of 80% (assuming a total primordial binary fraction of 100%) and a current binary fraction of ∼29% (eg., Noll et al. 2008a), we find that the fraction of wide to tight binaries could have been scaled down by roughly a factor of 2.6 over the age of the solar system. Using the larger lifetime ratio of $\frac{\tau_{tight}}{\tau_{wide}} = 2.7$, we find that the fraction of wide to tight binaries could be reduced by over a factor of 10 over the age of the solar system — however, this case would imply a current wide binary fraction of roughly half a percent, less than is observed.

Somewhere between these two cases, erosion is sufficient to account for the roughly factor of four discrepancy between the predictions of Nesvorný et al. (2010) and the current ratio of wide to tight binaries. A primordial tight binary fraction of 80% and wide binary fraction of 20%, scaled down to a present-day binary fraction of 29% with a factor of four decrease in relative fraction of wide binaries to tight binaries would imply a present day wide binary fraction of roughly 1.4%, slightly less than is observed. However, even this qualitative agreement is very encouraging given the somewhat preliminary nature of the simulations of Nesvorný et al. (2010) and the simplicity of the analysis presented here.

3.4.4 Second-order effects: mutual tides and the Kozai effect

This work generally ignored the effect of mutual tides (only treating them to the extent that mutual pericenter approaches within the Roche limit caused a merger), and did not include the effect of Kozai oscillations (Kozai 1962, Fabrycky & Tremaine 2007, Perets & Naoz 2009) on the evolution of the binary orbits. Because we found that the correction from the analytical estimate of collisional lifetimes did not vary systematically with system eccentricity, we do not expect that including Kozai cycles will significantly alter the estimates of collisional lifetimes. However, they may somewhat alter the behavior of the evolution of inclination and eccentricity over the age of the solar system. Future work is merited to fold in the effects of mutual tides and Kozai cycles, especially when large samples of binaries are uncovered by future surveys and the conclusions derived from their orbital distribution become more precise.

3.4.5 Prospects for detecting catastrophic collisions

Many of the collisions modeled in the numerical simulations we present in §3 would produce a prodigious amount of dust and debris. Such collisions may occasionally be detectable as transient brightening events, similar to the event detected in the Main Asteroid Belt in early 2010 (Jewitt et al. 2010). Given the frequent deep observations of large areas of the sky in upcoming surveys like Pan-STARRS and LSST, we estimate the frequency at which such events will be detectable. Similar estimates have been made for collisions in the Main Asteroid Belt (LSST Science Book v.2, 2009, Ch. 5.6.1)

Using the estimates of debris cross-sectional area produced in collisions derived in Wyatt & Dent (2002) for grains larger than 1 mm in radius, and conservatively assuming an albedo of 5% for the debris produced by the catastrophic disruption of

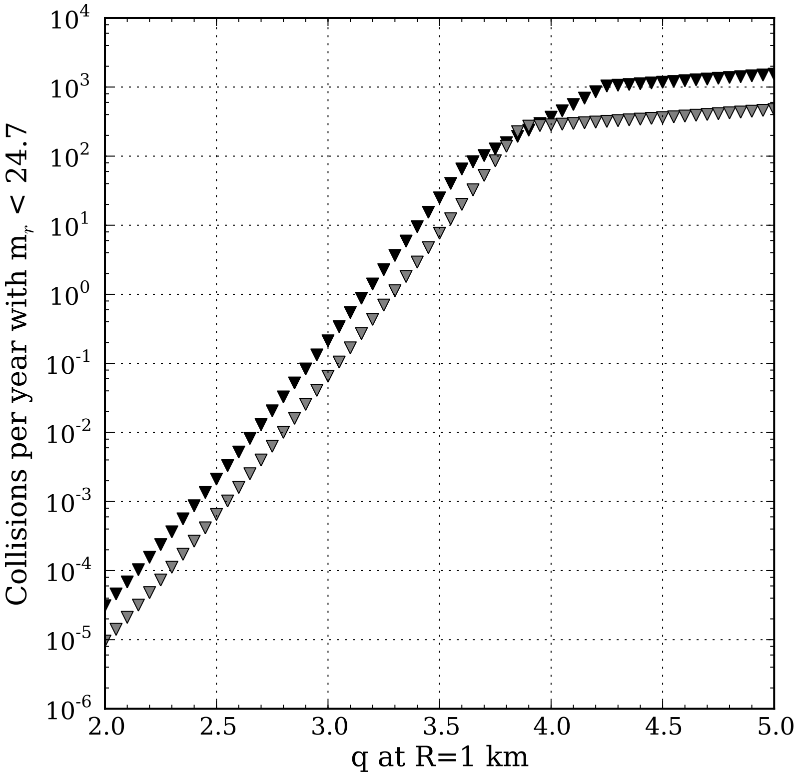

Figure 3.14: Estimate of the rate of collision events in the Classical Kuiper Belt detectable by LSST, given the small-object population limits discussed in the text. Results assuming $P_i = 1.3\times10^{-21}$ km^{-2} yr^{-1} (black triangles) and $P_i = 4\times10^{-22}$ km^{-2} yr^{-1} (gray triangles). Breaks indicate transition from population limits determined by the observed number of large objects (leftmost trend), binary survival (middle trend, only visible in the black triangles), and occultation limits (rightmost trend).

small TNOs, we find that that a collision which disrupts 50% of the mass of a 700 m radius TNO will produce a debris cloud sufficiently large to be detected in reflected light by LSST (given a single-visit r-band depth of 24.7). Similarly, impacts which disrupt 80% of the mass of a 600 m radius TNO or 5% of the mass of a 1.6 km radius TNO will also be detectable. By Eqns. 3.6 and 3.7, we estimate that such disruption events will require impactors of radius ∼58 m, 57 m, and 72 m, respectively (given a relative velocity of ~ 1 km s^{-1}).

The lifetime of these events also factors into their detectability, and depends on the velocity dispersion of the debris cloud. Again adopting the derivations of Wyatt & Dent (2002) for the rate of azimuthal spreading for debris clouds produced by such a catastrophic impact, we estimate that such systems will remain visible for roughly two to three weeks before their surface brightness drops to below detectable levels.

Using the combination of $R \sim 1$ km population estimates presented earlier (extrapolation from large size, occultation limits, and binary survival), we can estimate the frequency of impacts as large or larger than this minimum detectable size as a function of size distribution slope. Assuming the same two values for intrinsic collision probability P_i as used in our earlier analysis, we find that for reasonable size distribution slopes, there may be tens to hundreds of collision events detectable by LSST per year. Figure 3.14 illustrates the estimated frequency of detectable impacts, and the expected rate of events detectable by LSST is strongly dependent on the size distribution slope at small size. Thus, the detection or non-detection of these transient collision events in surveys like LSST may prove to be a strong indicator of the size distribution of very small objects in the Kuiper Belt.

3.5 Summary

1. For most reasonable impactor populations, the collisional lifetime of a TNB can be accurately estimated by analytical arguments with a small empirical correction determined by our simulations; the expression for collisional lifetime is given by Eqn. 3.13. This estimate includes the effects of multiple collisions and mass loss.

2. Evolution of separation and eccentricity preferentially occurs along lines of constant apocenter, and 90-95% of all systems modeled have final pericenters lower than their primordial apocenter. This is further evidence that the wide bina-

ries are not examples of primordially-tight binaries which have been widened by collisional processes, as we would expect eccentricities to be high on average ($e \gtrsim 0.8$).

3. Collisions with objects in the 1—5 km radius range are capable of unbinding the ultra-wide TNBs, and the continued existence of these systems constrains the number of impactors that can presently exist in the Classical Kuiper Belt. These limits are compatible with the extrapolation of the measured large object ($R > 30$ km) population to $R \sim 1$ km with a size distribution power-law slope of less than $q \simeq 3.5 - 3.7$, depending on the assumed intrinsic collisional probability. These limits are also compatible with the putative detection of a stellar occultation by a single ~ 250 m object in the Classical Kuiper belt (Schlichting et al. 2009) for slopes greater than $q \simeq 2.5 - 3$. The convergence of these estimates suggests that, barring more complicated structure in the size distribution (eg., a collisional "divot," Fraser 2009), the size distribution slope at small radii is roughly consistent with collisional equilibrium at $q \sim 3.5$.

4. Collisions with realistic collider size distributions do not cause any strong asymmetry between prograde and retrograde survival times, and it is likely that the equal numbers of prograde and retrograde mutual orbits reflects the primordial inclination distribution. A non-negligible fraction of binaries have their orientation flipped from prograde to retrograde and vice-versa, but not a large enough fraction to account for the observed prograde to retrograde ratio if the binaries were formed by the L_2s mechanism, as Schlichting & Sari (2008b) predict roughly 97% of such systems would form with retrograde orientation.

5. Even with impact trajectories drawn from a disk-like distribution, it is unlikely for the ultra-wide TNB inclinations to have been generated by collisional modification of an initially uniform inclination distribution. Instead, the ultra-wide TNB inclination distribution must have been dynamically colder in the past.

6. Faster erosion of a widely separated binary population plausibly resolves the over-production of wide binaries by the model of Nesvorný et al. (2010), as reasonable impactor populations can easily cause a reduction in the relative fraction of wide binaries to tight binaries by the required factor of roughly four.

7. Analytical arguments can reproduce similar trends in binary fraction with primary radius as found by Nesvorný et al. (2011), and slow erosion of the binary

population was found to produce similar trends in binary fraction with radius as rapid collisional grinding. This will complicate the interpretation of any future detection of a trend in binary fraction with radius.

8. Upper limits on small-object populations still can allow enough collisions to be occurring that next-generation optical surveys like LSST may detect tens to hundreds of transient brightening events per year due to large dust-producing impacts. The rate of these events is extremely sensitive to the size distribution at small size, and the detection or non-detection of such collisions may be a powerful diagnostic of the decameter-scale impactor population in the current Kuiper Belt.

Chapter 4

Binary Disruption by Neptune Scattering

This chapter is based on a Letter published in the Astrophysical Journal:
Parker, A. & Kavelaars, J.J., 2010. ApJL 722, 204.

The dynamical histories of the sub-populations of the Kuiper Belt remain in contest. Producing an inclination width as high as is observed (eg., Kavelaars et al. 2008) while maintaining a cold component with low eccentricities and inclinations remains a theoretically challenging prospect. Levison et al. (2008, hereafter L08) present numerical simulations designed to determine if the Nice model, a proposed framework for understanding the history and architecture of the outer Solar System, provides a pathway to create the low-inclination component of the classical Kuiper Belt. They suggest that the objects that now reside in the Cold Classical Kuiper Belt (CCKB) may have formed significantly interior to their present heliocentric distances, and were scattered outward by interactions with Neptune during a high-eccentricity period of its early orbital evolution. During this period, the region exterior to Neptune was full of overlapping mean-motion resonances (MMRs). Objects that entered this region could chaotically evolve to low eccentricity, where some would become trapped as the eccentricity of Neptune damped out and the resonance widths decreased and ceased to overlap. Assuming that Neptune's eccentricity started at 0.3 and was damped with a timescale of order 1 Myr, L08 finds that a distinct population of low-e, low-i objects can be injected into the Kuiper Belt region.

Trans-Neptunian Binaries likely formed in the primordial disk (binary formation in

Table 4.1: Initial Planetesimal Orbits

Parameter	Range
a_{out}	20–34 AU
e_{out}	0–0.4 ($a_{\mathrm{out}} < 29$ AU), 0–0.15 ($a_{\mathrm{out}} > 29$ AU)
i_{out}	0°–10° ($a_{\mathrm{out}} < 29$ AU), 0° ($a_{\mathrm{out}} > 29$ AU)

the current Kuiper Belt is suppressed by its low density and relatively high energetics) and would have been subjected to the same Neptune interactions proposed for the entire CCKB-precursor population by L08. As illustrated in the previous chapters, the current binary population in the CCKB has a component with extremely wide separations; for example, the system 2001 QW$_{322}$ has a semi-major axis to Hill radius fraction (a/R_H) of ~ 0.22. Such wide systems are extremely sensitive to perturbations (Petit and Mousis, 2004), and may have undergone significant modification or even disruption if they were subjected to close encounters with Neptune. We seek to test whether an initial population of TNBs subjected to emplacement into the CCKB through the L08 mechanism could leave behind a remnant population of binaries large enough to produce those we see today. We track the evolution of a given binary system through a suite of *multiple* of close encounters with Neptune determined by the close encounter histories of objects emplaced in the CCKB through the L08 mechanism.

Binary-planet encounters have been explored in the context of capturing planetary satellites (Agnor and Hamilton, 2006; Vokrouhlický et al. 2008). Our analysis and simulations are similar to those used by these studies, but specifically focus on the end-states of the *binaries*, rather than the captured population of planetary satellites.

4.1 Close Encounter Histories

To accurately determine the tidal effects of Neptune on passing binaries, we first determined the trajectories of their close approaches relative to Neptune. These trajectories were generated by running a suite of N-body simulations that track the interactions of a Neptune-mass object with a swarm of massless particles. Since we are interested in testing the effects of the Kuiper Belt formation scenario simulated by L08, we must generate close-encounter trajectories that reflect those that binaries would have experienced given the L08 model. The initial conditions of our simulations were chosen to emulate Run B from L08, since this run was the most successful at generating a final Kuiper Belt with characteristics similar to those we see today. This

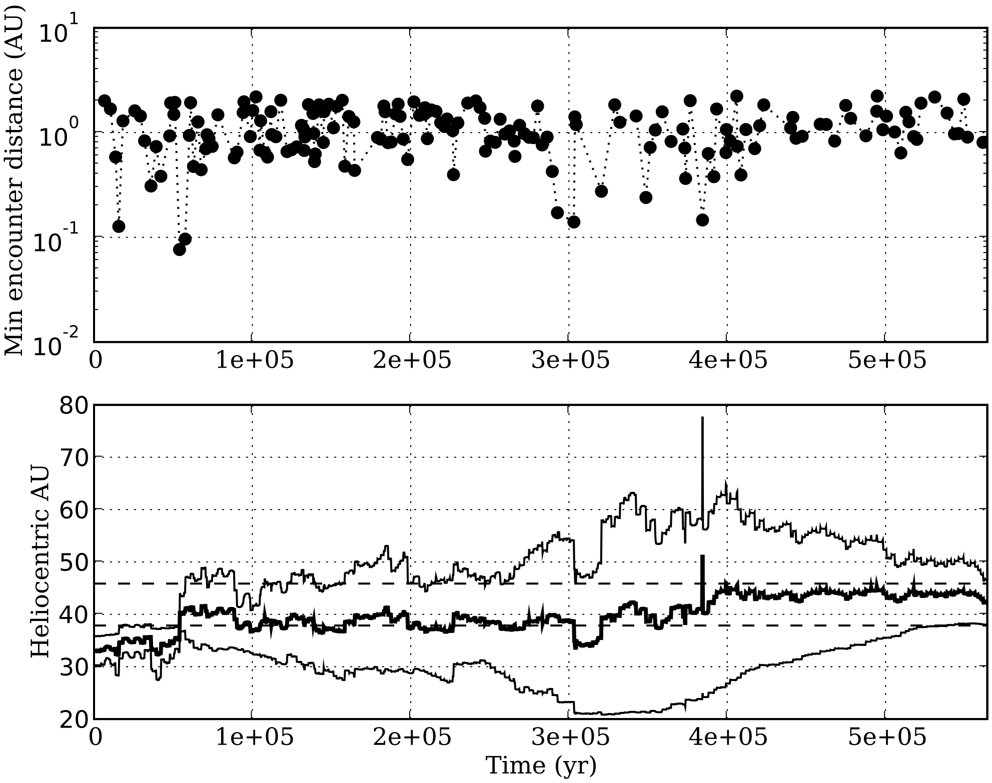

Figure 4.1: An example of a close encounter history for one particle flagged as having reached the CCKB. Top Panel: minimum Neptuneocentric distance for all tracked close encounters vs. time since integration start. Bottom panel: Orbital elements of the particle vs. time since integration start. Thick line represents semi-major axis, while lower and upper thin lines represent pericenter and apocenter, respectively. Lower and upper dashed lines mark our synthetic Neptune's 3:2 and 2:1 mean-motion resonances, respectively. Only close encounters inside 1AU were treated during our integrations of binary mutual orbits.

initial configuration sets Neptune's initial semi-major axis at 28.9 AU and eccentricity at 0.3, and the swarm of planetesimals initially between 20 AU $< a_{\rm out} <$ 34 AU (see Table 4.1 for initial orbital elements of the planetesimal swarm).

Since we are interested only in the characteristics of the close encounters that scatter objects into orbits that can be caught in the series of overlapping exterior MMRs, we did not evolve Neptune's orbital elements from their initial values. We monitored each particle's semi-major axis and eccentricity for 1 Myr and find all those candidates that pass through "CCKB-like" orbits which no longer have close encounters with Neptune. If any particle passed through 38 AU $< a_{\rm out} <$ 45.9 AU (3:2 and 2:1 MMRs for the initial Neptune orbit), $e_{\rm out} < 0.1$, and $i_{\rm out} < 5^\circ$ after at least 0.5 Myr has passed, we flagged it as having reached the CCKB. This is a conservative approach, as objects may continue to evolve in eccentricity for some time before the overlapping MMRs would have snapped closed due to the eccentricity damping imposed on Neptune by L08, which could result in later epochs where the object has close encounters with Neptune. Additionally, by allowing such low (38 AU) semi-major axes for our CCKB flagged sample, we are including objects that did not suffer as much orbital migration as would be required for objects reaching the real CCKB, which exists between semi-major axis limits of $\sim 42.5 - 47$ AU (eg., Kavelaars et al. 2008).

Using a modified version of the *Mercury 6* N-body code (Chambers 1999), we integrated an initial population of 15,000 particles; of these, 156 were emplaced in the CCKB according to our criteria. For every object which we flagged as having reached the CCKB, we generated a "close encounter history" by extracting all encounters that occurred within 3 Neptune Hill Radii. Figure 4.1 illustrates a single close encounter history for a particle which reaches the CCKB in 6×10^5 years, and Figure 4.2 shows the distribution of close encounters for all particles flagged as reaching the CCKB in our simulations.

The top panel of Fig. 4.3 illustrates the relative velocity at infinity v_∞ for the Neptune close encounters in our simulations. The distribution for the particles that reached the CCKB is peaked at approximately 1 km s^{-1}, and the peak is coincident with the median. The peak for the distribution of all the particles is at approximately 1.7 km s^{-1}, while the median lies at 2.3 km s^{-1}. This is consistent with the distributions produced by the simulations presented in Vokrouhlický et al. (2008). The bottom two panels of Fig. 4.3 show the source of the difference in the v_∞ distributions between the total population of particles and the subset that reach the

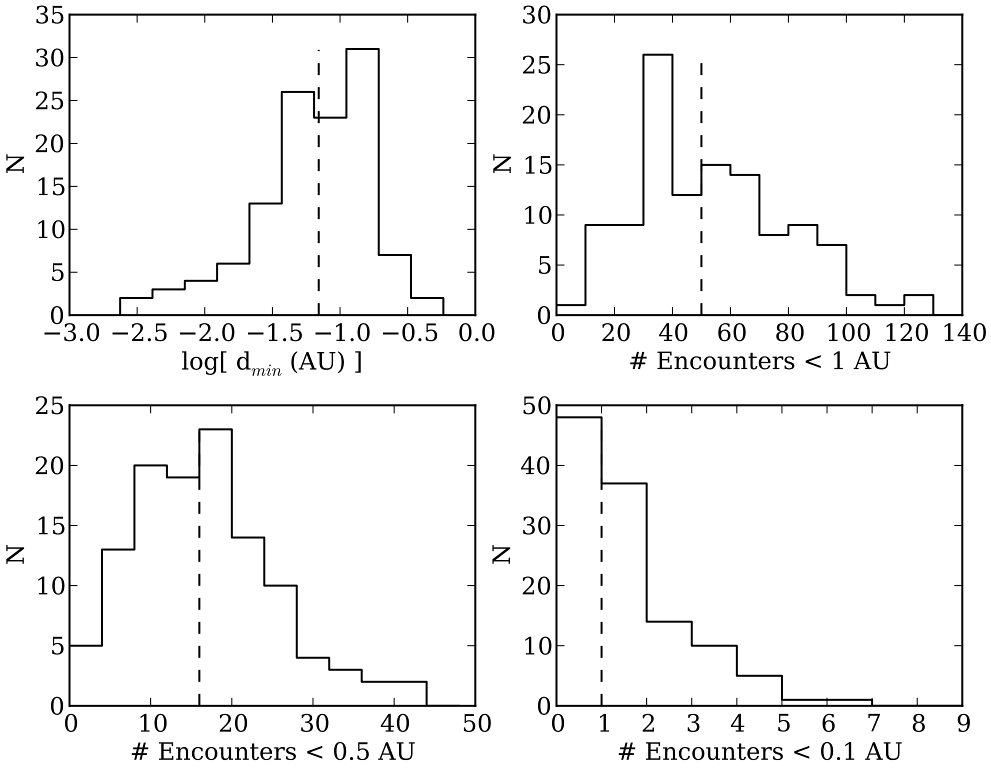

Figure 4.2: Close encounter statistics for all 156 particles which were flagged as entering the CCKB. Top left: histogram of the minimum separation for the closest approach in each close encounter history. Top right, lower left, and lower right: Histogram of the number of encounters in each close encounter history < 1 AU, 0.5 AU, and 0.1 AU, respectively. In all panels, medians are illustrated with vertical dashed lines. For conversions, Neptune's hill radius is approximately 0.77 AU, and 0.1 AU correspond to approximately 600 Neptune radii.

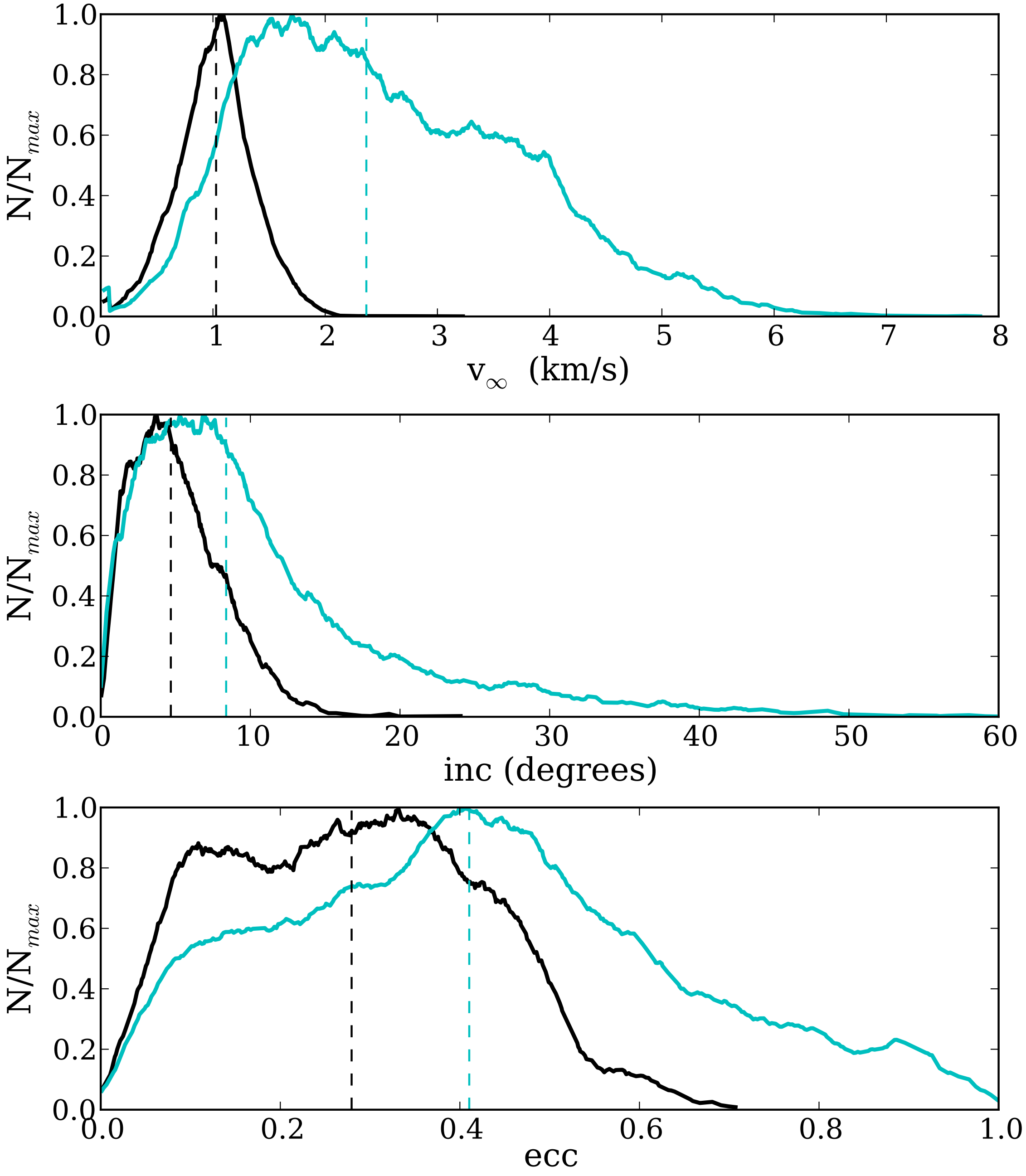

Figure 4.3: Top panel: Distribution of velocity at infinity (relative to Neptune) for close encounters in our simulations, normalized to unity. Middle and bottom panel: Distribution of inclination and eccentricity for particles in our N-body simulations. Values are sampled at random epochs from all particles' histories. Black lines represent the distribution for particles that reached CCKB. Gray lines represent the distributions for random subset of all particles. Vertical dashed lines mark medians of each distribution.

CCKB. The crossing velocity between two objects is driven by their relative inclination and eccentricity, and objects that reach the CCKB have a significantly lower median inclination and eccentricity throughout their history. In other words, objects that *start with* or that are *scattered into* highly inclined or highly eccentric orbits are rarely emplaced into the CCKB. Because of this, the median v_∞ for the particles that reach the CCKB is lower than for the entire population (which includes many objects scattered to large inclination or eccentricity).

4.2 Integration of Binary Orbits

We used a second, purpose-built numerical integrator to simulate the close encounters between binary systems and Neptune. *Mercury 6* was modified to produce position and velocity at closest approach to Neptune for each close encounter passing less than 1 AU ($\sim$ 1.3 Neptune Hill radii) from Neptune. For each close encounter, we generated a hyperbolic trajectory with respect to Neptune that replicated these quantities (Neptuneocentric pericenter separation and velocity). If a given encounter lead to temporary capture by Neptune, we increased the encounter velocity to the parabolic limit, decreasing the overall tidal impulse Neptune can exert on the system (making this a conservative approximation with respect to the efficiency of disruption of binaries).

All binaries are treated as a massive primary with a test particle as a secondary. We verified that this had little effect on our results by running a sample of several thousand binary integrations with mass ratios of 1:1 which produced no notable change in outcome.

The initial binary orbits are sampled from the range covered by known classical Kuiper Belt binaries (Naoz et al. 2010, Grundy et al. 2009, Petit et al. 2008, Veillet et al. 2002), and are generated as follows:

1. Draw a/R_H from a uniform distribution between 0.005—0.3.

2. Draw a from from a uniform distribution between 2×10^3—1.2×10^5 km.

3. Determine M from given a/R_H and a. If it lies outside 10^{16}—10^{19} kg, re-select a and re-compute M. Repeat until successful.

4. Eccentricity is drawn from a uniform distribution between 0—0.95, and all

initial angular parameters (including inclination) are drawn from uniform distributions over their entire physical ranges.

At the beginning of each integration of a given close encounter in a specific encounter history, we used the mutual orbital elements from the *last* integration of the same binary in order to generate the relative position and velocity of the secondary with respect to the primary (mean anomaly, node, and argument of pericenter are randomized). We then placed the primary on the hyperbolic trajectory of this close approach with Neptune, and placed the secondary on the same trajectory with the addition of an offset in position and velocity determined by its mutual orbit with the primary. The binary is started at a distance of 1.5 AU ($\sim$ 2 Neptune Hill radii) from Neptune, and integrated until passing outside a radius of 1.5 AU from Neptune. All motions are taken to be in the frame of Neptune.

A binary is considered destroyed if any of the following criteria are met after any close encounter integration:

1. The system becomes unbound (Total energy of the system is greater than zero).
2. Mutual semi-major axis is enlarged to more than one Hill Radius (with respect to the Sun, assuming a circular final heliocentric orbit at 40 AU).
3. Binary components collide (assuming a density for each component of 1 g cm^3 in order to determine radii).

At the end of *all* close encounters in a given history, a binary is considered to have survived emplacement into the CCKB if it has not been destroyed by any of the criteria above. In our simulations, by far the most common mechanism for destruction was (2), representing $\sim$98.5% of all disruptions, while cases (3) and (1) each contributed nearly negligibly at $\sim$1.3% and $\sim$0.2%, respectively. In most cases, the closest few approaches in a given encounter history determine if a binary survives (mutual semi-major axis evolution is similar to a Lévy flight, eg., Colins and Sari 2008); however, more distant encounters can cause modification of binary orbits that make later close approaches more likely to disrupt the system. This illustrates the importance of treating entire encounter histories.

These destruction criteria should be considered very conservative. The true a/R_H limit for stability varies with inclination but is always < 1, and considering R_H variations due to heliocentric orbit evolution during scattering will lead to more efficient disruption by solar tides. Mergers may become more important if we considered Kozai cycles (Perets and Naoz 2009, Kozai 1962) and tidal damping effects.

Figure 4.4 illustrates the results of 7,500 integrations of the binary-Neptune interactions, requiring roughly 150 CPU-hours to integrate. Binaries with initially wide orbits are efficiently destroyed before being emplaced in the CCKB, with the probability of destruction crossing 50% at approximately $a/R_H \sim 0.05$ and increasing to 80% by $a/R_H \sim 0.1$. Additionally, we find that it is unlikely that binaries with initially tight orbits and which survive emplacement are left with significantly widened orbits: for all binaries that survived emplacement with initial $a/R_H < 0.05$, only $\sim 5\%$ have final a/R_H exceeding 0.05, and fewer than 2% exceed 0.075. Those binaries that are widened show no preference for any specific region of initial mutual eccentricity-inclination phase space.

We found a larger fraction ($\sim 50\%$) of objects implanted into the CCKB from inside the 29 AU boundary between the initially excited and non-excited disks than was found by L08. To check if these additional inner objects skewed the probability of binary disruption (as L08 showed that such objects are subjected to more Neptune encounters), we performed a second set of 7,500 binary encounter integrations using only the 94 encounter histories for objects with initial $a_{\mathrm{out}} > 29$AU, removing the influence of the inner objects. The results are illustrated in Figure 4.4, and for wide separations the variations in destruction probability between the full sample and the "outer disk" sample are minor.

Binary mutual orbits that were initially very eccentric ($e > 0.7$) were somewhat more easily disrupted than initially more circular orbits ($e < 0.2$) for moderate a/R_H, with the largest variation between the two groups being $\sim 10\%$. For higher a/R_H, this difference decreases substantially. A second smaller set of integrations was run to test the effect of initial inclination, and the difference in destruction probability between separate samples of 1500 $i = 0°$ and $i = 90°$ mutual orbits remained less than a few percent at all a/R_H.

4.3 Discussion

We have simulated the effects of interactions between Neptune and Trans-Neptunian Binaries, given the kinds of encounter histories required for emplacement of the CCKB though the mechanism proposed by L08, and we find that wide binaries ($a/R_H > 0.05$) are efficiently destroyed by these interactions. Any primordial population of wide

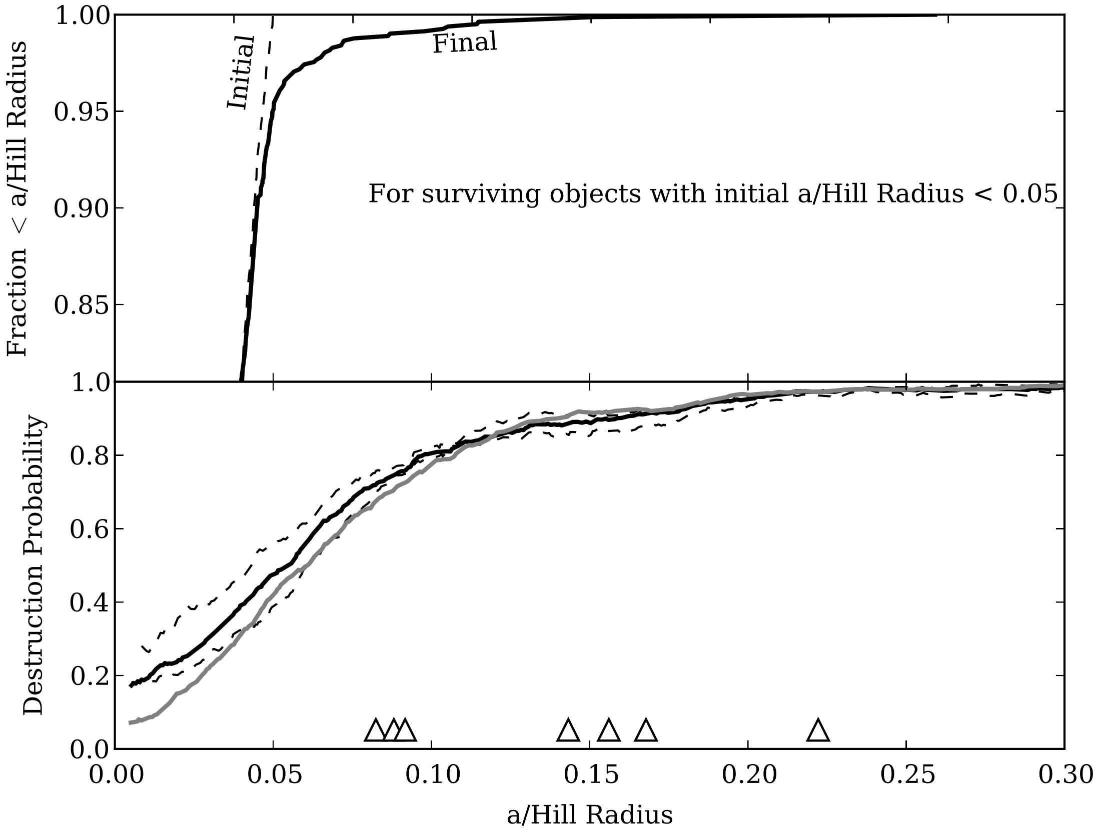

Figure 4.4: Results from two sets of 7,500 binary-Neptune integrations. Top panel: "Mobility" of initially tight binaries. Dashed line is a cumulative histogram of a/R_H prior to Neptune interactions for surviving binaries with initial $a/R_H < 0.05$. Solid line is a cumulative histogram of a/R_H for the same binaries after interactions. Bottom panel: Probability of destruction of a binary system as a function of its initial a/R_H. Lower and upper dashed lines represent subset of sample with $e < 0.2$ and $e > 0.7$, respectively. Gray line: Results from integrating encounter histories for objects with initial $a_{\mathrm{out}} > 29$AU. Triangles: estimates of a/R_H for the seven wide binaries characterized in previous chapters.

binaries would be decimated by emplacement into the cold belt through this process. The binaries we characterize in previous chapters are all wide enough to be easily stripped by this process, and comparing the a/R_H and eccentricity of our systems to the results of the simulations of Neptune scattering, we find destruction probabilities ranging from at least 75% for b7Qa4 to over 98% for 2001 QW_{322}. Furthermore, such interactions would likely have randomized the orbit poles of the surviving wide binaries, not leaving behind the aligned poles we see today.

Taken together, we estimate that if our sample represents a population which has been subjected to disruption by Neptune scattering, the initial population of ultra-wide TNBs would have to have been roughly 13 times larger than the current population. If we take the lower limit of the current wide binary fraction of the Cold Classical Kuiper Belt estimated by Lin et al. (2010) at 1.5%, this indicates that the primordial wide binary fraction have to exceed 20% to leave enough wide binaries surviving post-Neptune scattering. Correcting the estimate of Kern & Elliott (2006) to apply to only the Cold Classical Kuiper Belt (using the same approach as Lin et al. 2010) results in an estimate closer to 5% for the current wide binary fraction, which would imply a primordial fraction of wide binaries in excess of 65%. These estimates assume no other processes disrupted binaries in the intervening time between implantation in the Kuiper Belt and the present day. A primordial wide binary fraction of 20% is comparable to the entire current binary fraction in the Cold Classical Kuiper Belt.

As mentioned previously, the Nesvorný et al. (2010) simulations appear to overproduce wide binaries with respect to today's population; synthetic binaries as wide or wider than the ultra-wide TNBs characterized in this work created by the Nesvorný et al. (2010) model represent roughly 20% of the systems produced by their simulations. Therefore, if the primordial binary fraction was $\sim$ 100%, the ultra-wide binary population produced in these simulations would be roughly sufficient to leave a remnant population similar to the observed population after implantation in the cold Classical Kuiper Belt through Neptune scattering if no additional processes disrupted these systems afterward. However, since a much larger fraction of the tighter binaries would survive the implantation process, we would expect a significantly larger remnant population of tight binaries if the primordial binary fraction was so high. Later processes (such as collisions) could modify the binary fractions over the age of the solar system, but generally wide binaries are more susceptible to stripping processes and the relative fraction of wide to tight binaries will tend to decrease over time. Therefore, barring a formation mechanism that much more strongly favors wide separations, we find that the ultra-wide binary orbits indicate that it is unlikely for the cold Classical Kuiper Belt to have experienced a period of scattering encounters with Neptune. This implies that a component of the Cold Classical Kuiper Belt was not emplaced by scattering from lower heliocentric orbits, but either had to form *in situ* or be implanted by a gentler mechanism in order to preserve its population of wide binaries.

Binary destruction by Neptune scattering may help explain the variation of binary fraction between different Trans-Neptunian populations. The binary fraction is much lower in the high-i (Hot) component of the Classical Kuiper Belt than in the low-i component (Noll et al. 2008b). L08 illustrate that objects captured in the Hot Classical Kuiper Belt via the mechanisms presented in Gomes (2003) interacted with Neptune for significantly longer than simulated in this work ($\sim 10^7$ years). If the Hot Classical Kuiper Belt was emplaced in large part by these mechanisms, a significant fraction of its initial binary population may have been destroyed. This would naturally decrease the binary fraction of this population without appealing to variations in the original formation mechanism of Trans-Neptunian Binaries.

The two known binary Centaurs (Grundy et al. 2008; Grundy et al. 2007) are actively interacting with the giant planets, and have dynamical lifetimes of order 1-100 Myr (Tiscareno and Malhotra 2003). If we take our simulations of encounters with Neptune as a baseline for estimating the probability of disruption of these binary systems over their lifetimes as Centaurs, we see that for systems as tight as these (with a/R_H of order $\sim 0.007 - 0.01$), probability of disruption after ~ 1 Myr is fairly low (10-15%), but their survival over tens of Myr is quite unlikely. Their existence likely reflects the different encounter histories Centaurs are subjected to compared to objects injected into the CCKB through the mechanisms studied here.

Chapter 5

Summary and Conclusions

5.1 Trans Neptunian Binaries: What's new?

The chapters of this thesis have laid out the results of an observational campaign to characterize the widest known Trans-Neptunian Binaries, along with two dynamical studies aimed at determining the implications of their current properties. Here these results are summarized, and the facets of these results which are truly new with respect to the body of knowledge in literature regarding Trans-Neptunian Binaries are highlighted. Figure 5.1 illustrates the physical scale of the mutual orbits in this sample with respect to other binary minor planets, and demonstrates the uniqueness of these objects.

5.1.1 Exceptional systems

Several of the binaries in the sample characterized in this work have turned out to be new record-setters, with extreme values in mass, separation, and eccentricity.

The system 2001 QW$_{322}$ has the largest separation between its components of any known binary minor planet, both in physical terms (semi-major axis of 1.015×10^5 km, or over a quarter of the Earth-Moon separation) and in terms of Hill sphere occupation ($a/R_H \simeq 0.22$). The wide separation of this system was already known from the previous partial characterization of the system by Petit et al. (2008).

The two binary systems L5c02 and hEaV both have extremely high mutual eccentricity — 0.9 and 0.84, respectively. L5c02 is therefore the most eccentric binary minor planet currently known, and hEaV is the second-most eccentric Trans-Neptunian binary known.

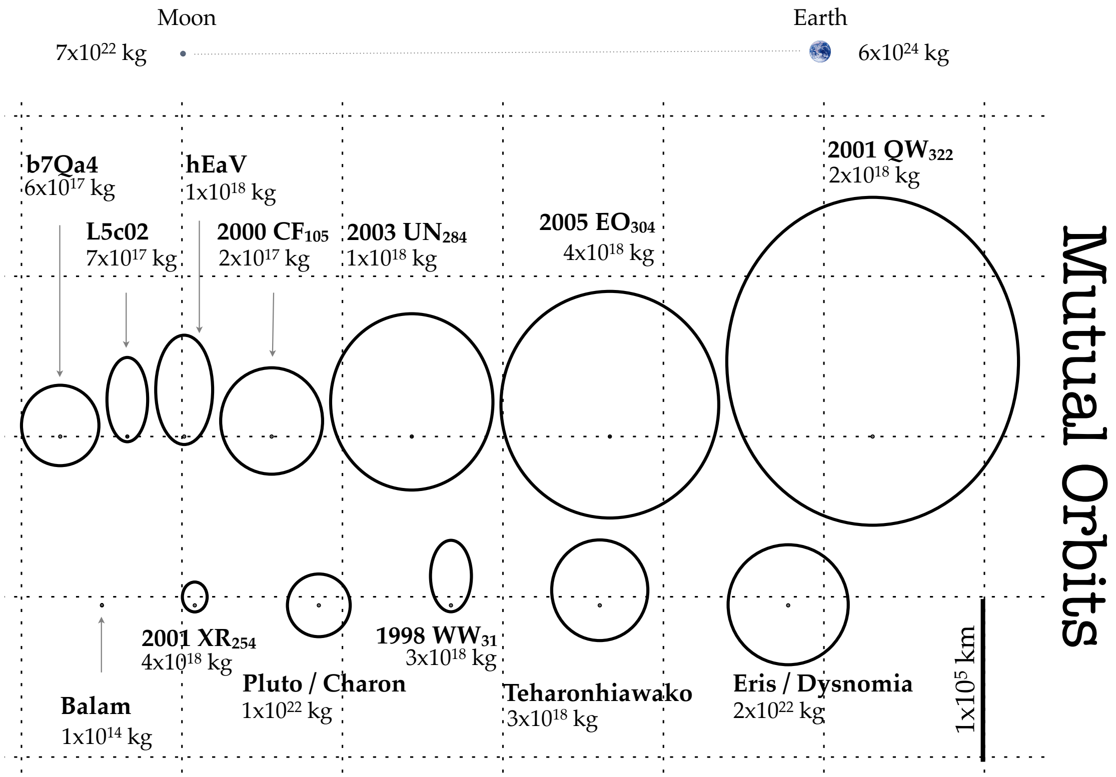

Figure 5.1: Illustration of the scales of the mutual orbits of the seven ultra-wide Trans-Neptunian Binaries characterized in this work (middle row) in comparison to a sample of other binary minor planets (bottom row) and the Earth-Moon system (top). First-order system masses are shown, and the radii of the Earth and Moon are to scale.

2000 CF_{105} has the lowest measured mass of any Trans-Neptunian Object at 1.85×10^{17} kg. Assuming both components share the same density (1 gram cm^{-3}) and albedo and adopting a $\Delta m \sim 0.72$, this leads to a primary radius of 32 km and a secondary radius of 23 km. These radii are comparable or even smaller than the estimated radius of the break in the Kuiper Belt's size distribution, a size regime which should be stripped of binaries if the Kuiper Belt was ever subjected to a period of intense collisional grinding (Nesvorný et al. 2011).

5.1.2 Membership

The outer orbits of all known binaries with $a_m/R_H > 0.02$ are consistent with being drawn from the debiased orbital distribution of the CFEPS L7 Cold Classical Kuiper Belt (the "stirred" and "kernel" components), and are inconsistent with being drawn from any other population. This indicates that the wide binaries are hosted exclusively by the Cold Classical Kuiper Belt, and that the dynamical history of this population must support the survival of these wide binaries.

5.1.3 Mutual Orbit Properties

The mutual orbits of the current sample of seven ultra-wide Trans-Neptunian Binaries are now determined to far greater accuracy than in any previous study. They occupy large fractions of their mutual Hill spheres ($a_m/R_H \sim 0.08-0.22$), and are more widely separated that the predictions of the Chaos-Assisted Capture formation mechanism (Astakhov et al. 2005). Additionally, while hEaV and L5c02 have high mutual eccentricities, all others in the sample have mutual eccentricities inconsistent with the predictions of Exchange Reactions (Funato et al. 2004). The wide separations suggest formation in a dynamically cold environment, as binaries with separations of $s \gtrsim R_H(v_H/v)^2$ (where v is the velocity dispersion of planetesimals in the primordial disk, and v_H is the Hill velocity) tend to be disrupted (Schlichting & Sari 2008a & b) — so given the observed separations of the wide binaries, $v \lesssim 4 \times v_H$.

Mutual inclinations are known for all systems, and the pole solutions are non-degenerate. There is no significant preference for prograde or retrograde orbits, and a predominantly retrograde population as predicted by the L_2s formation mechanism (Schlichting & Sari 2008b) is ruled out. The mutual orbit poles are relatively aligned, and are inconsistent with being drawn from either a uniform distribution ($p(i_m) \propto \sin(i_m)$) or the inclination distribution of tighter binaries from literature. Kozai Cycles coupled with tidal friction (Fabrycky & Tremaine 2007) are insufficient to modify an initially uniform inclination distribution to an extent which would be consistent with the observed distribution, and therefore the primordial inclination distribution of the wide binaries must have preferred low inclinations. This primordial preference must have been stronger than the extant preference, as a non-uniform inclination distribution will tend to evolve toward a uniform distribution if subjected to random perturbations from collisions. A preference for low mutual inclinations suggests a very dynamically-cold disk ($v < v_H$, Noll et al. 2008), but it cannot be *too* dynamically cold or the L_2s mechanism would dominate over the L_3 mechanism in the binary formation rate and produce retrograde binaries. Thus, there is a fine-tuning problem if the L_2s and L_3 mechanisms are the sole processes responsible for forming the wide binaries, as this would require that $v \simeq v_H$, and at present there is no clear reason for such a condition to be expected. Additionally, it remains unclear if a balance can be struck which allows the formation of aligned poles which have no preference for prograde or retrograde orientation, and further investigation of these formation mechanisms is required.

The separations and eccentricities of the wide binaries are consistent with the predictions of formation of binaries through gravitational collapse (Nesvorný et al. 2010), and this mechanism somewhat over-produces wide binaries with respect to the observed fraction of wide vs. tightly bound binaries, leaving room for collisional decay of the wide population. At present, the initial conditions of these models remain poorly constrained, and the simulations are preliminary in nature and make no prediction about the orientations and inclinations of the resulting binaries. However, the success of the current simulations with regard to separation and eccentricity is encouraging, and these models should be refined and seriously investigated.

5.1.4 Albedos

Estimates of the r-band albedo of each object were found by combining the measured system masses of each binary with their observed H magnitude, and assuming a plausible bulk density for each component of $\rho = 1$ gram cm^{-3}. These albedos ranged from 0.08-0.3, and are consistent with the high albedos measured for solitary low-inclination Classical TNOs. An ansatz albedo distribution of the form

$$P(p) \propto \begin{cases} e^{-0.5(\frac{p-0.05}{\sigma_p})^2} & : p > 0.05 \\ 0 & : p \leq 0.05 \end{cases} \tag{5.1}$$

is consistent with the observed albedos and radii, assuming the observed objects were drawn from surveys with flux limits of approximately $H \sim 8$ and from an underlying size distribution with slope $q = 4.8$. Widths between $0.058 \leq \sigma \leq 0.1$ are consistent with the observed sample. Steeper size distribution slopes would require that the binary fraction decay with decreasing radius, as predicted by Nesvorný et al. (2011).

5.1.5 Collisional lifetimes

Since these binaries are so widely separated, they are sensitive to collisional disruption by relatively small impactors. Numerical simulations were performed of the bombardment of each binary system with impactors drawn from realistic size distributions with a variety of small-object slopes, and these showed that the binaries' mean lifetimes could be accurately approximated by an analytical function. Using this function and the constraint that any collisionally-eroded primordial binary population must leave behind the observed population of wide binaries, upper limits on the population of small objects ($R \gtrsim 1$ km) in the present day Kuiper Belt were determined. The extrapolation of the observed large-object populations, the putative observation of a single stellar occultation by a 250 m TNO (Schlichting et al. 2009), and the collisional upper limits all converge at a small-object slope near the collisional equilibrium slope of $q \simeq 3.5$. Slopes significantly higher than this are ruled out by the continued existence of very small binaries like 2000 CF_{105}.

Additionally, it is unlikely for these wide binaries to represent a collisionally-evolved tail of the primordially tightly-bound binaries. If this were the case, one would expect the wide binaries to have at least as uniform an inclination distribution as the current tight binaries, and they do not. One would also expect a preference for high mutual eccentricities, and this is inconsistent with the observed moderate mutual eccentricities.

5.1.6 Transport by Neptune

Levison et al. (2008) and others posit that the Kuiper Belt may have formed nearer to the Sun than its present location, and been transported outward by interactions with the giant planets (primarily Neptune). However, numerical simulations presented in this work show that the close encounters with Neptune required to scatter the Cold Classical Kuiper Belt into its current location would have been extremely disruptive to wide binaries, and would not have widened primordially tight binaries sufficiently to re-supply the wide binary population. Thus, the continued existence of a large population of very widely separated binaries in the Cold Classical Kuiper Belt suggests that at least this population was never subjected to an intense period of close encounters with Neptune, and was likely formed in situ.

5.2 Implications for solar system science: processes in the primordial disk

In the previous chapters, we have found that the inclination distribution of the wide binaries indicates a very cold dynamical environment at the time of formation, but formation of the binaries post-accretion through the L_2s pathway — which should dominate in such conditions — can be ruled out due to a lack of preference for retrograde orientations. We also found that the cold Classical Kuiper Belt was never subjected to a period of close encounters with Neptune, and therefore likely formed in situ. Finally, the properties of mutual orbits produced by current simulations of gravitational collapse are consistent with the observed properties of binaries in the cold Classical Kuiper Belt.

Together, all these results suggest that formation of the cold Classical Kuiper Belt occurred in situ, with objects forming via rapid collapse of small particles directly into large ($10 - 100$ km) planetesimals through primary accretion driven by turbulent concentration of solids in the protoplanetary disk (eg., Johansen et al. 2007, Cuzzi et al. 2010). This process offers a mechanism for forming binaries such as are observed in this population, and can feasibly form the cold Classical Kuiper Belt in situ (Cuzzi et al. 2010) without requiring that a large fraction of the primordial mass in planetesimals be subsequently removed through either significant collisional grinding or dynamical processes (both of which can be destructive to the binary population), even when the density of the primordial disk is required to drop sharply beyond 30 AU to halt the early migration of Neptune at its present distance. Additionally, since this process produces no massive sea of small planetesimals (most planetesimals being “born big”), the L_2s mechanism will naturally be ineffective, thus preventing it from forming a dominantly retrograde binary population in the dynamically cold environment indicated by the binaries' low mutual inclinations.

The mechanism of binary formation by gravitational collapse should be extensively explored. If it can be shown to produce roughly equal numbers of prograde and retrograde binaries while maintaining a preference for low mutual inclinations, then this should be taken as strong support for the formation of the cold Classical Kuiper Belt in situ by rapid primary accretion driven by turbulent concentration and gravitational collapse.

5.3 Future Prospects

Previous chapters illustrated that future large-scale optical surveys will have incredible capacity to discover and characterize a very large sample of wide Trans-Neptunian Binaries. Such a sample, drawn from a single survey with well-defined flux completeness, will provide a powerful constraint on the albedo distribution of the Kuiper Belt. Binary properties which may vary with component size, outer heliocentric orbit, or other characteristics can be mapped and used to further constrain the formation mechanisms of Trans Neptunian Binaries, thus further illuminating the dynamics of the primordial planetesimal disk.

The current collisional environment can be probed as well, as expanding clouds of dust grains produced by collisions in the Kuiper Belt may be detected by the same future surveys. The rate of detection is strongly linked to the slope of the size distribution at small sizes, and may prove to be a powerful discriminator of the properties of the population of very small objects in the current Kuiper Belt.

The current sample of wide binaries can also be further explored and exploited. More accurate photometry will help nail down the albedo uncertainties, and measurements of lightcurves of the individual components may reveal the spin rates or possibly the presence of a third component in some systems. Continued astrometric observations are merited to further refine the masses and other properties of these systems.

Further dynamical studies are merited as well. Performing tidal stability analyses and including higher-order effects in the collisional evolution code will produce information crucial in interpreting any large, well-characterized sample of wide Trans-Neptunian binaries uncovered by future surveys.

Chapter 6

Bibliography

- Adams, C. 1846. Monthly Notices of the Royal Astronomical Society 7. 149.
- Agnor, C. and Hamilton, D., 2006. Nature, 441. 192-194.
- Airy, G. B., 1846. Monthly Notices of the Royal Astronomical Society 7. 121.
- Astakhov, S., Lee, E. & Farrelly, D. 2005. Monthly Notices of the Royal Astronomical Society 360, 401.
- Barkume, K., Brown, M., & Schaller, E. 2008. The Astronomical Journal 135. 55-67.
- Barucci, M., Belskaya, I., Fulchignoni, M. & Birlan, M. 2005. The Astronomical Journal 130. 1291-1298.
- Benecchi, S., Noll, K., Grundy, W., Buie, M., Stephens, D., & Levison, H. 2009. Icarus 200, 292.
- Benz, W., & Asphaug, E. 1999. Icarus 142, 5.
- Bernstein, G., Trilling, D., Allen, R., Brown, M., Homan, M., Malhotra, R. 2004. The Astronomical Journal 128, 1364.
- Bertin E. & Arnouts S. 1996. Astronomy and Astrophysics Supp. 117, 393.
- Bickerton, S., Kavelaars, JJ., & Welch, D. 2008. The Astronomical Journal 135, 1039.
- Brown, M. 2001. The Astrophysical Journal 121, 2804.
- Brown, M., Schaller, E., Roe, H., Rabinowitz, D. & Trujillo, C. 2006. The Astrophysical Journal 643. 61-63.
- Brown, M., Barkume, K., Ragozzine, D. & Schaller, E. 2007. Nature 446. 294-296.

- Brown, M., Ragozzine, D., Stansberry, J. & Fraser, W. 2010. The Astronomical Journal 139, 2700.
- Brucker, M., Grundy, W., Stansberry, J., Spencer, J., Sheppard, S., Chiang, E. & Buie, M. 2009. Icarus 201, 284.
- Christy, J. W., & Harrington, R. S., 1978. The Astronomical Journal 83. 1005-1008.
- Chambers, J., 1999. Monthly Notices of the Royal Astronomical Society, 304. 793-799.
- Collins, B. and Sari, R., 2008. The Astronomical Journal, 136. 2552-2562.
- Cuzzi, J. Hogan, R., Bottke, W. 2010. Icarus 208, 518.
- Delsanti, A., Boehnhardt, H., Barrera, L., Meech, K., Sekiguchi, T. & Hainaut, O. 2001. Astronomy and Astrophysics 380, 347.
- Duncan, M., Quinn, T. & Tremaine, S. 1988. The Astrophysical Journal 328. 69-73.
- Edgeworth, K. 1949. Monthly Notices of the Royal Astronomical Society 109. 60.
- Fabrycky, D. & Tremaine, S. 2007. The Astrophysical Journal 669, 1298.
- Farinella, P., Davis, D. & Stern, S. 2000. In: Mannings, V., Boss, A., Russell, S. (Eds), Protostars and Planets IV. Univ. of Arizona Press, Tucson, AZ, 1255.
- Fernandez, J. 1980. Monthly Notices of the Royal Astronomical Society 192. 481-491.
- Fraser, W., Brown, M. & Schwamb, M. 2010. Icarus 210. 944-955.
- Fraser, W. & Brown, M. 2010. The Astrophysical Journal 714. 1547-1550.
- Fraser, W. C. 2009. The Astrophysical Journal 706, 119.
- Fraser, W. C. & Kavelaars, J. J. 2009, The Astronomical Journal 137, 72
- Fuentes, C. I., George, M. R., & Holman, M. J. 2009, The Astrophysical Journal 696, 91
- Funato, Y., Makino, J., Hut, P., Kokubo, E. & Kinoshita, D. 2004. Nature 427, 518.
- Gladman, B., Kavelaars, JJ., Petit, J.-M., Morbidelli, A., Holman, M. & Loredo, T. 2001. The Astronomical Journal 122. 1051-1066.
- Gladman, B., Marsden, B., VanLaerhoven, C. 2008. In: Barucci, M., Boehnhardt, H., Cruikshank, D., Morbidelli, A. (Eds), The Solar System Beyond Neptune. Univ. of Arizona Press, Tucson, AZ.

- Goldreich, P., Lithqick, Y. & Sari, R. 2002. Nature 420, 643.
- Gomes, R., 2003. Icarus, 161. 404-418.
- Grundy, W., Standberry, J., Noll, K., Stephens, D., Trilling, D., Kern, S., Spencer, J., Cruikshank, D., and Levison, H., 2007. Icarus, 191. 286-297.
- Grundy, M., Noll, K., Virtanen, J., Muinonen, K., Kern, S., Stephens, D., Stansberry, J., Levison, H., and Spencer, J., 2008. Icarus, 197. 260-268.
- Grundy, W., Noll, K., Buie, M., Benecchi, S., Stephens, D. & Levison, H. 2009. Icarus 200, 627.
- Grundy, W. M., Noll, K. S., Nimmo, F., Roe, H. G., Buie, M. W., Porter, S. B., Benecchi, S. D., Stephens, D. C., Levison, H. F. & Stansberry, J. A. 2011, Icarus (In press).
- Herschel, W. 1781. Philosophical Transactions of the Royal Society of London 71. 492.
- Jewitt, D. & Luu, J. 1993. Nature 362. 730-732.
- Jewitt, D. & Luu, J., 2001. The Astronomical Journal 122, 2099.
- Jewitt, D., Weaver, H., Agarwal, J., Mutchler, M. & Drahus, M. 2010. Nature 467, 817.
- Johansen, A., Oishi, J., Low, M-M., Klahr, H., Henning, T. & Youdin, A. 2007. Nature 448, 1022.
- Kavelaars, J.J., Jones, L., Gladman, B., Parker, J. W., and Petit, J.-M., 2008. Barucci, M.A., Boehnhardt, H., Cruikshank, D.P., and Morbidelli, A. (Eds.), The Solar System Beyond Neptune. Univ. Arizona Press, Tucson, 59.
- Kenyon, S., Bromley, B., O'Brien, D. & David, D. 2008. In: "The Solar System Beyond Neptune." Univ. of Arizona Press, Tucson, AZ, pp. 193.
- Kern, S. 2006. Doctoral Thesis, Massachusetts Institute of Technology.
- Kern, S. & Elliot, J. 2006. The Astrophysical Journal 643, L57.
- Kowal, C. T., Liller, W. & Marsden, B. 1979. In "Dynamics of the Solar System; Proceedings of the Symposium." Dordrecht, D. Reidel Publishing Co., p. 245-250.
- Kozai, Y. 1962. The Astronomical Journal 67, 591.
- Kuiper, G. 1951. Proceedings of the National Academy of Sciences 37. 1.
- Lee, E., Astakhov, S. & Farrelly, D. 2007 Monthly Notices of the Royal Astronomical Society 379. 229-246.
- Leonard, F. 1930. Astronomical Society of the Pacific Leaflets 1. 121-124.

- Levison, H. & Morbidelli, A. 2003. Nature 426. 419-421.
- Levison, H., Morbidelli, A., VanLaerhoven, C., Gomes, R. & Tsiganis, K. 2008. Icarus 196, 258.
- Lin, H.-W, Kavelaars, J. J, Ip, W.-H, Gladman, B. J, Petit, J. M, Jones, R. L, Parker, J. W. 2010, Publications of the Astronomical Society of the Pacific 122, 1030.
- LSST Science Collaborations & LSST Project. 2009, LSST Science Book, Version 2.0, arXiv:0912.0201
- Lunine, J. 1993. Science 261, 697.
- Marchis, F., Descamps, P., Berthier, J., Hestroffer, D., Vachier, F., Baek, M., Harris, A., Nesvorný, D. 2008. Icarus 195, 295.
- Margot, J., Nolan, M., Benner, L., Ostro, S., Jurgens, R., Giorgini, J., Slade, M. & Campbell, D. 2002. Science 296, 1445.
- Merline, W., Weidenschilling, S., Durda, D., Margot, J., Pravec, P. & Storrs, A. 2002. in Asteroids III, U of Arizona Press, 289.
- Metropolis, N., Rosenbluth, A., Rosenbluth, M., Teller, A. & Teller, E. 1953. Journal of Chemical Physics 21, 1087.
- Morbidelli, A., Levison, H., Tsiganis, K. & Gomes, R. 2005. Nature 435. 462-465.
- Müller, T. and 34 co-authors. 2010. Astronomy and Astrophysics 518. L146.
- Naoz, S., Perets, H. & Ragozzine, D. 2010. The Astrophysical Journal 719. 1775-1783.
- Nesvorný, D., Youdin, A. & Richardson, D. 2010. The Astronomical Journal 140, 785.
- Nesvorný, D., Vokrouhlický, D., Bottke, W., Noll, K., Levison, H. 2011 The Astronomical Journal 141, 159.
- Nicholson, S. & Mayall, N. 1930. Publications of the Astronomical Society of the Pacific 42. 350.
- Noll, K., Stephens, D., Grundy, W., Millis, R., Spencer, J., Buie, M., Tegler, S., Romanishin, W., & Cruikshank, D. 2002. The Astronomical Journal 124, 3424.
- Noll, K., Levison, H., Grundy., W., and Stephens, D., 2006. Icarus, 184. 611-618.

- Noll, K., Grundy, W., Stephens, D., Levison, H. & Kern, S. 2008a. Icarus 194, 758.
- Noll, K. Grundy, W., Chiang, E., Margot, J.-L., Kern, S. 2008b. In: Barucci, M., Boehnhardt, H., Cruikshank, D., Morbidelli, A. (Eds), The Solar System Beyond Neptune. Univ. of Arizona Press, Tucson, AZ.
- Parker, A. H. & Kavelaars, J. J., 2010, The Astrophysical Journal Letters 722, L204.
- Perets, H. & Naoz, S. 2009. The Astrophysical Journal 699, L17.
- Perets, H. & Naoz, S. 2008. arXiv:0809.2095v1
- Petit, J.-M. & Mousis, O. 2004, Icarus 168, 409.
- Petit, J.-M., Kavelaars, JJ., Gladman, B., Margot, J.-L., Nicholson, P., Jones, R., Parker, J., Ashby, M., Campo-Bagatin, A., Benavidez, P., Coffey, J., Rousselot, P., Mousis, O. & Taylor, P. 2008. Science 322, 432.
- Rabinowitz, D. L. et al 2006. The Astrophysical Journal 639. 1238.
- Ragozzine, D. 2009. Doctoral Thesis, California Institute of Technology.
- Richardson, D. & Walsh, K. 2006. Annual Revue Earth Planetary Science 34, 47.
- Schlichting, H. & Sari, R. 2008a. The Astrophysical Journal 637, 1218.
- Schlichting, H., & Sari, R. 2008b. The Astrophysical Journal 686, 741.
- Schlichting, H., Ofek, E., Wenz, M., Sari, R., Gal-Yam, A., Livio, M., Nelan, E., & Zucker, S. 2009. Nature 462, 895.
- Simard, L., WIllmer, C., Vogt, N., SarThe Astronomical Journaledini, V., Phillips, A., Weiner, B., Koo., D., Im., M., Illingworth, G. & Faber, S. 2002. The Astrophysical Journal Supp. 142, 1.
- Szabó, Gy. M., Ivezić, Ž., Jurić, M. & Lupton, R. 2007. Monthly Notices of the Royal Astronomical Society 377. pp 1393-1406.
- Tiscareno, M., and Malhotra, R., 2003. The Astrophysical Journal, 126. 3122-3131.
- Tombaugh, C. 1946. Astronomical Society of the Pacific Leaflets 5. 73.
- Tsiganis, K., Gomes, R., Morbidelli, A. & Levison, H. 2005. Nature 435. 459-461.
- Veillet, C., Parker, J., Griffin, I., Marsden, B., Doressoundiram, A., Buie, M., Tholen, D., Connelley, M. & Holman, M. 2002. Nature 416, 711.
- Verrier, U.L. 1846. Astronomische Nachrichten 25. 53.

- Vokrouhlický, D., Nesvorný, D. and Levison, H., 2008. The Astrophysical Journal, 136. 1463-1476.
- Walsh, K. 2009. Earth, Moon & Panets 105, 193.
- Wang, J.-H. and 23 co-authors, 2009. The Astronomical Journal 128, 1893.
- Weidenschilling, S. 2002. Icarus 160, 212.
- Weidenschilling, S. 1977. Astrophysics and Space Science 51. 153-158.
- Wyatt, M. & Dent, W. 2002. Monthly Notices of the Royal Astronomical Society 334, 589.
- Yoshida, F. & Nakamura, T. 2008. Publications of the Astronomical Society of Japan 60. 297-301.
- Yoshida, F., Nakamura, T. 2005. The Astronomical Journal 130. 2900-2911.